SAINT-PETERSBURG UNIVERSITY

Solovev Ivan Aleksandrovich

COHERENT OPTICAL DYNAMICS OF EXCITONS AND TRIONS IN SEMICONDUCTOR QUANTUM WELLS

Scientific specialisation 1.3.8. Condensed matter physics
Translation from Russian

Dissertation is submitted for the degree
of Candidate of Physical and Mathematical Sciences

Thesis supervisor:
Dr. Sci. (Phys-Math), Prof.
Irina A. Yugova

Saint Petersburg – 2023

Contents

Introduction

Relevance of the topic

The history of the study of exciton effects began back in the 30s of the XX century, when J. Frenkel first proposed the existence of excitons as excitation quanta by analogy with phonons [1, 2]. Later strongly localized excitons will be called Frenkel excitons., which characteristic size is of the order of the size of an atom and which are observed primarily in molecular crystals. In crystals with a high permittivity, by excitons one refers electron-hole pairs of large radius coupled by Coulomb interaction, the theory for which was proposed by Wannier [3] and subsequently developed by Mott [4, 5]. It is these quasiparticles, called Wannier-Mott excitons, that are observed in semiconductor crystals, for example, in gallium arsenide or zinc oxide. Experimental observation of excitons in copper oxide Cu_2O was first carried out by E. Gross in the early 1950s [6].

Despite the fact that the fundamentals of exciton physics were considered more than 50 years ago, this topic is extremely relevant today. Technological progress in the field of semiconductors has led to the emergence of fundamentally new objects - semiconductor heterostructures, the characteristic dimensions of which are on the nanometer scale. In contrast to bulk materials, the optical properties of such objects as quantum wells (QWs), quantum wires, and quantum dots (QDs) are mainly determined by exciton effects due to an increase in the overlap of the electron and hole wave functions in an exciton [7, 8]. At the same time, by manipulating the percentage composition of heterostructure layers and their characteristic sizes, one can set the desired exciton parameters [9]. Thus, the study of resonant exciton features began to play a major role in the spectroscopy of nanostructures [10].

Alongside with the improving of the quality of grown epitaxial structures, femto- and picosecond laser technology had been rapidly developing, which makes it possible to achieve exceptionally high values of the instantaneous intensity of the electromagnetic field [11, 12]. High laser pulse intensities together with the resonant structure of exciton spectra made it possible to overcome the problem of low nonlinear susceptibility coefficients and to observe various nonlinear optical effects [13–17]. These achievements eventually opened the door to a new direction in exciton physics at the end of the 20th century - the study of ultrafast nonlinear optical dynamics [18].

The striking example of a nonlinear optical effect is four-wave mixing (FWM) which was considered first by Armstrong et al. was the [19]. The essence of the effect is following: when a nonlinear medium is excited by three electromagnetic waves, a fourth wave arises as a result of interaction, the wave vector and frequency of which do not coincide with those of the exciting waves in the general case [10, 18, 20]. The efficiency of the process is determined by the third-order nonlinear dielectric susceptibility $\chi^{(3)}$. Despite its smallness in the general case, the value, as a rule, increases in the resonance spectral range.

In the course of the development of FWM research, the spin echo technique from an inhomogeneous ensemble of spins found its new application, which was previously used in the field of nuclear magnetic resonance. It turned out that in optical spectroscopy it is possible to realize a similar effect for the photon echo (PE) predicted by Kopvillem and Nagibarov [21] and then demonstrated by Hartmann [22]. Today, transient FWM and, in particular, PE are powerful tools for studying the basic properties of the nonlinear interaction of light with semiconductor nanostructures, which make it possible to observe the coherent optical dynamics of excitons at times from hundreds of femtoseconds to a few nanoseconds [18, 23, 24].

From the very beginning of the fundamental research of FWM, there was a special interest in the possibilities of applied application of the results. As an example, we can cite creation of phase conjugate mirrors [25–28], prototypes of optical logic elements [29] and optical memory cells [30–35]. To date, an actual task of modern experimental physics is the search for new material platforms for creating elements of quantum computing [36]. The development of nonlinear optics of semiconductors, namely the implementation of coherent optical control, and the improvement of nanostructure growth technologies, made it possible to create systems based on QDs that meet the requirements for candidates for the role of a qubit [37–39]. The fundamental problem of any qubit platform is the loss of coherence [40]. In this context, the transient FWM is an extremely useful tool for studying the mechanisms of exciton dephasing in nanostructures, which indicates a high degree of relevance of such studies.

After briefly review of the historical course of the development of nonlinear optics of semiconductors, we could come to the conclusion that both ways of developing science are equally important: both the extensive one, with the expansion of the set of knowledge about various new material systems, and the intensive one,

with a deeper understanding of the fundamental processes observed in the already established systems. classical systems. Often the latter leads to the discovery of new subtle effects. This work contains both components, which indicates both the relevance of the research and its completeness. Chapters 3 and 4 are devoted to the application of the degenerate FWM technique to study novel wide-gap semiconductor structures with QWs based on ZnO and InGaN, the coherent properties of which were not well studied so far.

It is worth to consider potential implementations of any coherent control protocols after fundamental understanding of the nature of the processes occurring during interaction with light. Only if there is a predictable response of the system, it is possible to consider about the applied use of knowledge. Therefore, to study the dynamics of a spin-dependent PE, we intentionally use a well-studied system with (In,Ga)As/GaAs QWs of the highest quality which response is predictable. Thus, the concluding chapter is devoted to the development of a technique for spin-dependent coherent optical control of exciton states in a model GaAs-based system.

In our work, we use a protocol that combines the coherent optical dynamics of excitons with the spin precession of an electron and a hole in an exciton induced by an external magnetic field. After a thorough study the nature of such complex spin and optical dynamics of excitons in a model structure, it becomes possible to apply the developed methods to new objects, such as wide-gap QWs based on ZnO and InGaN, transition metal dichalcogenides, or perovskites.

Purpose and objectives

The purpose of this work is to develop the possibilities of coherent control of excitons and their charged complexes in semiconductor nanostructures. Development is proposed in two directions - the application of the photon echo method to the study of ultrafast coherent dynamics in promising novel low-dimensional semiconductor structures, as well as the development of protocols of coherent optical control of excitons based on the spin-dependent photon echo. Achieving this purpose required solving the following objectives:

- Building of an experimental setup for detecting a photon echo signal from semiconductor nanostructures, which are cooled down to liquid helium temperatures, with a picosecond time resolution, a 1 meV spectral resolution and the ability of manipulation by such degrees of freedom as the sample temperature, the polari-

metric configuration of excitation and detection, the application of an external magnetic field with an amplitude of up to 6 T.

- Experimental observation of a FWM signal in the form of a two-pulse spontaneous and a three-pulse stimulated photon echo under selective excitation of inhomogeneously broadened ensembles of neutral excitons and excitonic charged complexes in ZnO/(Zn,Mg)O, (In,Ga)N/GaN, and (In, Ga)As/GaAs quantum wells in the ultraviolet and infrared spectral range. Conducting spectral, polarimetric, temperature and power measurements of the photon echo signal.

- Determination of the effect of experimental conditions on optical dephasing and energy relaxation of excitons and excitonic complexes. Analysis of the obtained experimental data and comparison of the results with the theoretically expected behavior of the system, as well as with the published results.

- Experimental observation of Larmor precession of the electron and hole spins in the spin-dependent photon echo from excitons in (In,Ga)As/GaAs QW subject to transverse magnetic field. Study of the dependence of the signal on the magnetic field amplitude and polarization excitation-detection configuration.

- Analysis of experimental results using the model of a five-level exciton system interacting with light in a transverse magnetic field. The model is taking into account different dephasing rates for optically bright and dark excitons.

- Experimental verification of the presence of both the periodic oscillation regime and the aperiodic behavior of the spin-dependent photon echo decay predicted by the theoretical model.

Scientific research method

The fundamental experimental method of the work is time-resolved transient four-wave mixing. The method provides detection of ultrafast optical coherent dynamics of exciton excitations on a picosecond time scale. When using two- and three-pulse excitation protocol, the method makes it possible to determine the fundamental properties of the systems under study such as the rate of energy relaxation and the rates of reversible and irreversible phase relaxation. The advantage of the method is the ability to separate the contributions of various mechanisms leading to

phase and energy relaxation. The use of the spectrally narrow picosecond pulses allows for selective study ensemble of quasiparticles of interest without exciting other quasiparticles whose optical transitions are closely located in the spectral range. In addition, the instantaneous power in a picosecond pulse is many times less than in the conventionally used femtosecond pulse. This fact reduces the influence of undesired many-body interactions leading to excitation-induced dephasing.

Scientific novelty

All scientific results presented in the dissertation are new.

The picosecond photon echo technique has not yet been used to study the coherent optical properties of excitons and trions in structures with ZnO/(Zn,Mg)O quantum wells. The reason for this is that only recently it has been possible to achieve a relatively high growth quality of these structures [41, 42] . Using the spectrally narrow picosecond technique, the spectral dependences of the phase and energy relaxation times for ensembles of excitons and trions of two types A and B were determined for the first time. Original measurements made it possible to separate the contributions of various mechanisms to the phase and energy relaxation of the mentioned ensembles.

The presented studies of the coherent optical dynamics of localized excitons in a periodic structure with quantum wells (In,Ga)N/GaN, observed in the range of hundreds of picosecond, are the first measurements of this kind. To date, there are only a few reports devoted to the coherent optical properties of excitons in GaN-based nanostructures. However, in all published studies, optical coherence lasted only at subpicosecond timescale.

The work shows the first experimental demonstration of the protocol of spin-dependent two-pulse photon echo realized on a system of excitons in (In,Ga)As/GaAs quantum well. The experiment confirmed the theoretically predicted oscillatory behavior of the photon echo decay under application of a transverse magnetic field. An extraordinary aperiodic behavior of the signal was observed experimentally, which manifests the phase relaxation time of dark excitons. The method allowed to observe the Larmor precession of the heavy hole spin and to determine the corresponding $g-$factor in the range of magnetic fields 0-6 T, as well as to obtain information about the electronic $g-$factor, to estimate exchange interaction constant δ_0 and the inhomogeneous spread of the hole $g-$factor.

Theoretical and practical significance of the work

Basically, the presented work is of fundamental character. The main goal is to gain basic knowledge about the coherent optical dynamics of excitons and excitonic complexes in ZnO/(Zn,Mg)O, (In,Ga)N/GaN, and (In,Ga)As/GaAs semiconductor QWs. Obtaining knowledge about the energy structure of the ensembles under study, the nature of interaction with light, understanding the main mechanisms of dephasing and energy relaxation and the behavior of the system under the application of a magnetic field are of fundamental scientific importance in this work. The obtained knowledge can be included in lecture courses for university graduate students. In addition, from the practical point of view, one can cite the development of an experimental technique for spin-dependent photon echo with a picosecond time resolution. The Introduction of various degrees of freedom to the experimental setup allows to control a larger number of parameters and observe previously undetectable effects.

Scientific statement to be defended

- The monotonic growth of the energy relaxation rate Γ_1 and pure dephasing rate Γ_c of A trions in ZnO/(Zn,Mg)O quantum wells with increase of energy at low temperatures is a consequence of the localization of quasiparticles on potential fluctuations of the quantum well. The change in value of Γ_1 is owing to the nonradiative relaxation of trions inside a random potential landscape accompanied with the emission of phonons. Elastic scattering of moving trions by potential fluctuations leads to an increase in Γ_c as the localzation degree decreases.

- Excitons in (In,Ga)N/GaN quantum wells experience strong localization within a substantially inhomogeneous potential of the well, whose structure has a quantum dot-like character. Localization leads to an increase in the phase and energy relaxation times of excitons. Localization leads to a growth of the exciton dephasing and energy relaxation times

- Oscillations of the two-pulse photon echo signal from the InGaAs/GaAs quantum well subject to an external magnetic field are due to the Larmor precession of exciton spins.

- Mixing of bright and dark excitons in an (In,Ga)As/GaAs quantum well under the action of an external magnetic field leads to an increase in the dephasing time of the exciton system. In the regime of aperiodic behavior of the spin-dependent photon echo the dephasing time tends to that of long-lived dark excitons.

Reliability and approbation of the results

The consistency of theoretical modeling with experimental results, as well as the agreement between the conclusions and earlier published works, ensure the reliability of the results. The original scientific results of this work were presented at the following international scientific conferences:

1. I. A. Solovev, S. V. Poltavtsev, Yu. V. Kapitonov, I. A. Akimov, S. Sadofev, J. Puls, D. R. Yakovlev, and M. Bayer, Time-resolved photon echoes from excitons and trions in ZnO/ZnMgO quantum wells International conference on the physics of semiconductors (ICPS) July 29 - August 3 2018, Montpellier, France (the best poster)

2. I. A. Solovev, Yu. V. Kapitonov, I. A. Yugova, S. A. Eliseev, Yu. P. Efimov, V. A. Lovcjus and S. V. Poltavtsev, Magnetic field-dependent photon echo from excitons in InGaAs/GaAs quantum wells International Conference on Optics of Excitons in Confined Systems, September 16-20 2019, Saint Petersburg, Russia

3. I. A. Solovev, I. I. Yanibekov, Yu. V. Kapitonov, Ia. A. Babenko, V. A. Lovcjus, S. A. Eliseev, Yu. P. Efimov, I. A. Yugova, and S.V. Poltavtsev, Accessing dark excitons in InGaAs/GaAs quantum well via spin-dependent photon echo, International conference on physics of light-matter coupling in nanostructures, October 27-30 2020, Clermont-Ferrand, France (online)

4. I.A. Solovev, Yu.V. Kapitonov, I.A. Yugova, S.A. Eliseev, Yu.P. Efimov, V.A. Lovcjus and S.V. Poltavtsev Observation of dark exciton coherent dynamics in InGaAs/GaAs quantum well by means of spin-dependent photon echo, International symposium on photon echo and coherent spectroscopy (PECS-2021), October 25-30 2021, Kazan, Russia (Best research award for young scientists)

The results were also presented at three scientific seminars of the I. N. Uraltsev Spin Optics Laboratory, St. Petersburg State University.

Personal contribution

The author independently carried out the presented experimental measurements, processed and analyzed the obtained data. To conduct research at the Nanophotonics Research Center, St. Petersburg State University, the author independently built an experimental setup for study of two- and three-pulse spin-dependent photon echo with a picosecond time resolution. The author took an active part in the formulation of scientific problems, the interpretation of results and the preparation of scientific publications.

Publications

The main scientific results of the dissertation were published in 5 research articles, 4 were published in scientific journals of the first quarter Q1. All articles are indexed in the Scopus, Web of Science and RSCI databases. List of publications of the author on the topic of the dissertation:

1. I. A. Solovev, I. I. Yanibekov, I. A. Babenko, B. V. Stroganov, S. A. Eliseev, V. A. Lovcjus, Yu. P. Efimov, S. V. Poltavtsev, Yu. V. Kapitonov, I. A. Yugova "Manipulation of optical coherence of quantum-well excitons by transverse magnetic field", Physical Review B, **106** 115401 (2022)

2. I. A. Solovev, I. I. Yanibekov, Yu. P. Efimov, S. A. Eliseev, V. A. Lovcjus, I. A. Yugova, S. V. Poltavtsev, Yu. V. Kapitonov "Long-lived dark coherence brought to light by magnetic-field controlled photon echo", Physical Review B **103** 235312 (2021)

3. I. A. Solovev, Yu. V. Kapitonov, B. V. Stroganov, Y. P. Efimov, S. A. Eliseev, S. V. Poltavtsev "Separation of inhomogeneous and homogeneous broadening manifestations in InGaAs/GaAs quantum wells by time-resolved four-wave mixing", Journal of Physics: Conference Series, **1124**, 051042 (2018)

4. S. V. Poltavtsev, I. A. Solovev, I. A. Akimov, V. V. Chaldyshev, W. V. Lundin, A. V. Sakharov, A. F. Tsatsulnikov, D. R. Yakovlev, M. Bayer "Long coherent dynamics of localized excitons in (In,Ga)N/GaN quantum wells", Physical Review B **98**, 195315 (2018)

5. I. A. Solovev, S. V. Poltavtsev, Yu. V. Kapitonov, I. A. Akimov, S. Sadofev, J. Puls, D. R. Yakovlev, M. Bayer "Coherent dynamics of localized excitons and

trions in ZnO/(Zn,Mg)O quantum wells studied by photon echoes", Physical Review B **97**, 245406 (2018).

The author has 8 more publications that are not related to the topic of the dissertation.

Volume and the structure of the work

The dissertation consists of an introduction, five chapters and a conclusion.

The first chapter provides insights into exciton states in semiconductor nanostructures and comprises a review of studies of ultrafast exciton dynamics. The chapter presents an review of the manifestation of exciton relaxation mechanisms in various experimental techniques, with particular attention paid to the specifics of work on transient four-wave mixing and photon echo.

The second chapter describes the theoretical and experimental approaches used to study the photon echo. The first part of the chapter contains a description of the theoretical formalism necessary for the analysis of the photon echo signal from an exciton ensemble in quantum wells. The second part of the chapter is devoted to a detailed description of the experimental setup designed to measure the picosecond photon echo, with a description of the features of time-resolved signal detection.

The third chapter presents the new results of an experimental study of the coherent optical dynamics of excitons and trions in ZnO/(Zn,Mg)O quantum wells. The chapter contains a brief introduction, a description of the sample, original results of linear spectroscopy and measurements of the two- and three-pulse photon echo signal in the spectral region of exciton and trion transitions, temperature studies of coherent dynamics with an discussion of the results.

The fourth chapter presents the results of applying the photon echo technique to study the coherent optical dynamics of excitons in multiple quantum well structure (In,Ga)N/GaN QWs on a picosecond time scale. The chapter contains an introduction, a description of the sample under study, the results of original studies on the spectroscopy of two- and three-pulse photon echo from excitons at different temperatures, and discussion.

The fifth chapter is devoted to the development of protocols for the coherent control of excitons, namely, the experimental implementation of the protocol for spin-dependent photon echo in an (In,Ga)As/GaAs quantum well subject to transverse magnetic field. The chapter contains a brief introduction, a description of the

sample under study, original results of linear exciton spectroscopy and a study of the coherent optical dynamics of excitons by means of the two-pulse spin-dependent photon echo. The chapter provides an analysis of the theoretical model used to explain the observed oscillatory behavior of the echo signal. The peculiarities of the model are considered in detail in comparison with experimental data.

In conclusion, the results of the work are presented.

Chapter 1. State of the art in ultrafast spectroscopy of excitons in nanostructures

The chapter is devoted to a review on the experimental study of ultrafast exciton spectroscopy in semiconductor nanostructures. The chapter contains a description of exciton states and an overview of exciton dynamics studies by various experimental techniques with discussion of their features. Special attention is paid to a review of works on the study of the coherent optical dynamics of excitons by means of four-wave mixing and photon echo. At the end of the chapter, an review of recently published works on spin-dependent photon echo is given.

1.1 Exciton states in semiconductor nanostructures

In recent years, the focus of semiconductor research has shifted from bulk materials to the study of low-dimensional nanostructures. Artificially created objects are distinguished by the fundamental possibility to provide desired properties to an object and to design structures with the required characteristics [9]. Low-dimensional structures are actively used in a wide class of optoelectronic devices - from the conventional LEDs and laser pointers [43] to quantum single-photon detectors [44].

A number of books are devoted to the features of low-dimensional systems [9, 18, 45–48]. Among such systems, QWs are the simplest. The conventional version of a single semiconductor QW of the first type is a layered heterostructure consisting of semiconductors with different band gaps. A thin, on the order of 10-100 nm, layer of one semiconductor is grown between relatively thick layers of another semiconductor 50-200 nm thick, the band gap of which is greater than the width of the first one. The width difference is distributed between the valence band (V-band) and the conduction band (C-band), forming potential quantum wells for a hole and an electron, respectively, as shown in the figure 1. In low-dimensional systems, exciton effects play a key role in the light-matter interaction processes. In a bulk crystal, an exciton, as a hydrogen-like particle bound by the Coulomb interaction, has a Rydberg series of states in addition to the parabolic dependence of the kinetic
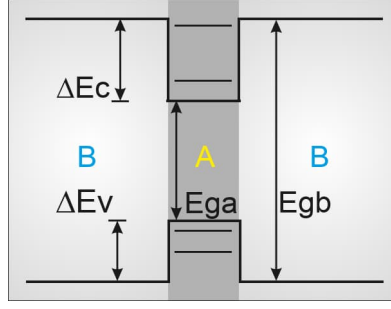
Figure 1: Scheme of type I QW and energy profile of the top of the valence band and the bottom of the conduction band. $Ega(Egb)$ is the band gap of the material A (B), $\Delta E_{C(V)}$ is the value of the potential well for an electron (hole); the energy quantization levels for an electron and a hole are shown schematically by the horizontal lines in the middle layer A.

energy of the exciton as a whole:

$$E = E_g - \frac{R_x}{n^2} + \frac{\hbar^2 Q^2}{2M}, \ R_x = \frac{\mu e^4}{32(\pi \hbar \varepsilon \varepsilon_0)^2}, \ M = m_c + m_v, \ \mu = \frac{m_c m_v}{m_c + m_v}, \quad (1)$$

where E_g is the crystal band gap, R_x is the exciton binding energy, M and μ are the total and reduced masses of the exciton, expressed in terms of the effective masses of the electron m_c and the hole m_v. R_x for GaAs is 4.8 meV, while for ZnO it is about 60 meV. In low-dimensional structures (QWs, QDs), quantum confinement of charge carrier leads to size quantization of the kinetic energy of an electron in the C band and for a hole in the V band, which significantly changes the energy structure and optical properties. Reducing the dimension of the structure also leads to a qualitative modification of the density of states function from a root dependence to a step function. This feature, together with the exciton effect, manifests itself in the absorption spectra [15, 49]. For a QW with a finite barrier height and a thickness comparable to the Bohr radius of a three-dimensional exciton (for GaAs, about 12 nm) and less, there is no analytical solution for stationary exciton states. A solution exists for the strictly two-dimensional case of a 2D exciton [45]:

$$E = E_g - \frac{R_x}{(n - 1/2)^2} + \frac{\hbar^2 Q_\parallel^2}{2M} + E_{hm} + E_{em}, \quad (2)$$

where E_{hm}, E_{em} are the electron and hole size quantization energies. Note, that for 1-s state of a 2D exciton, the binding energy increases by a factor of 4, and the exciton radius decreases by a factor of 2 compared to the three-dimensional case [9].

It makes it possible to observe exciton effects in QWs at higher temperatures, in contrast to bulk structures [15]. In physical wells, the binding energy E_x is between R_x and $4R_x$, and the stationary state energies are calculated using various numerical methods [47, 50, 51].

the interaction of excitons with an electromagnetic field also undergoes qualitative changes. In nanostructures, the possibility of direct radiative recombination appears due to translational symmetry breaking, in contrast to a bulk ideal crystal, in which exciton-polaritons are stationary states, and radiative recombination requires the involvement of a phonon or a defect in the process [52–54].

1.2 Peculiarities of spectroscopic methods for studying excitons in nanostructures

The study of the interaction of light with matter, as a rule, begins with a consideration of the linear response. Linear optical spectroscopy is attractive due to its elegant simplicity and at the same time it provides a rich set of basic information about the nature of the interaction. In the case of studying direct-gap semiconductors, the main methods are photoluminescence (PL) and reflection spectroscopy. Next, we briefly consider the studies of excitons in nanostructures by the methods mentioned above.

1.2.1 Nonresonant photoluminescence

Basically PL method consists in excitation of the structure by light with a photon energy above the spectral range of interest and observation of the secondary luminescence of the structure. In PL spectroscopy of QWs, laser excitation has usually photon energy above the energy of the well barrier. A detailed consideration of the method is provided in the monograph [55]. When a photon is absorbed, an electron from the valence band exhibits an optical transition to a state in the conduction band. The created electron-hole pair undergoes rapid energy relaxation to the lowest energy states corresponding to excitons. Ultimately, at low temperatures (units of Kelvin), the lines of the lowest exciton states predominate in the PL spectra, since the intensity of the lines in the PL spectra is determined not only by the strength of the transition oscillator, but also by the level population [55]. The change in the spectral position of the ground exciton state in the PL spec-
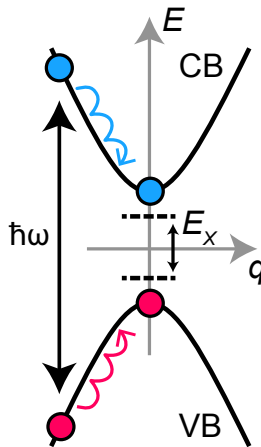
Figure 2: Scheme of nonresonant excitation of an electron-hole pair and subsequent thermalization of charge carriers with the formation of an exciton. CB - conduction band, VB - valence band. The dotted line illustrates schematically the exciton transition energy E_X for comparison with the band gap, the difference between which is determined by the exciton binding energy.

trum clearly shows, for example, the temperature narrowing of the band gap [56], accompanying by the broadening of exciton resonances due to exciton-background scattering [57], as shown in the figure 3.

PL technique turns out to be extremely useful also in studying the properties of excitons subject to a magnetic field and exciton fine structure [58]. Owing to the trend towards emission from the lowest states, the micro-PL makes it possible to obtain information about the localized states of excitons in the well and, thereby, to estimate the degree of interface inhomogeneity, as shown in figure 4 [59, 60]. Therefore, the PL method is often used as a tool for inspection of the growth quality of structures [61–64]. In this work, we will also extensively exploit this method for the basic optical characterization.

PL can be used not only to obtain a stationary spectroscopic pattern, but also to reveal the kinetics of ultrafast relaxation and radiative recombination of excitons. High temporal resolution is achieved using ultrashort laser pulses and either direct detection with fast photodetectors or various two-pulse techniques such as up-conversion [18, 65]. The latter technique was used by Damen et al. [66]. Under nonresonant excitation with laser energy above the exciton transition the exciton PL kinetics of excitons in a high-quality QW begins with an increase in the signal, the characteristic time of which increases with decreasing temperature and reaches hundreds of ps at $T = 5$ K. The rise time of the signal is determined by the rate of formation of radiative excitons, which, in turn, depends on the processes
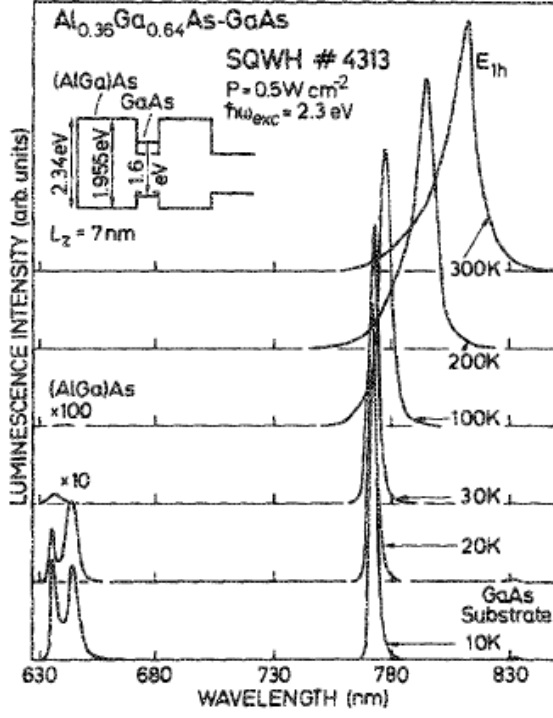
Figure 3: PL spectra of GaAs/AlGaAs measured at Temperatures from 10 to 300 K. The sample structure and excitation configuration is plotted in inset. Imported from [57]
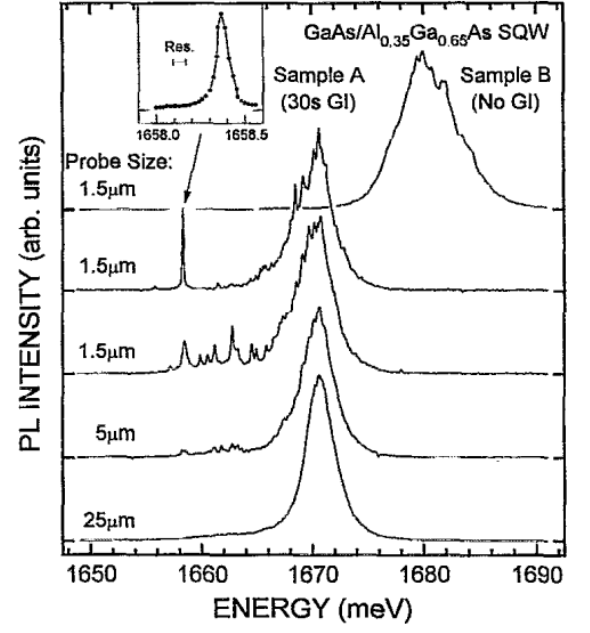
Figure 4: Micro-PL spectra of the growth-interrupted sample (A) and the sample grown without interruption (B) as a function of detection spot diameter. Imported from [59].

of relaxation of electron–hole pairs with the formation of hot excitons, followed by thermalization and relaxation of the energy and momentum projection along the well plane. To distinguish between these processes, the authors studied the kinetics of exciton line broadening. It turned out that the broadening of the exciton PL line due to collisions of excitons with charge carriers is much larger than the broadening due to exciton-exciton scattering. As a consequence, the kinetics of broadening of the PL line showed that the main mechanism of the long rise in PL is associated with the relaxation of the momentum of non-radiative excitons. Similar indirect manifestations of long-term relaxation of non-radiative excitons were recently observed [67].

An increase of the exciton density makes the exciton thermalization faster [68], and it was used to shorten the PL rise time [69]. As a result the oscillating behavior of the PL rise time with increasing excitation energy was observed, which was associated with the entering into phonon replica resonances.

The complexity of data interpretation could be considered as a The drawback

Figure 5: Sketch of dispersion of exciton states in quantum well and linear dispersion of ligth.

of the PL technique [70]. For example, as was shown above, in the case of non-resonant excitation, it is necessary to take into account t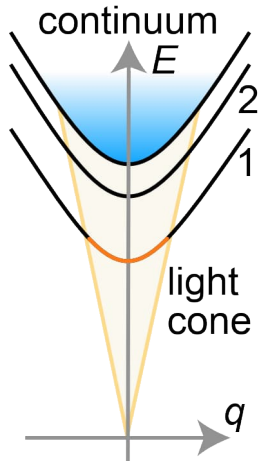he formation process of optically active excitons. Often variety of mechanisms lead to similar observable results, and in real systems they can all take place simultaneously. It should be noted that due to the multiple events of energy relaxation with the emission of phonons, information about the phase of the exciting light is lost, so the PL emission occurs in all directions. The mentioned shortcomings can be partially circumvented by applying quasi-resonant excitation in the spectral vicinity of the resonance of interest. However, this method always has the problem of filtering the useful signal from the scattered exciting light. For example, one has to detect PL in the polarization crossed with the exciting light.

1.2.2 Resonant photoluminescence

Despite the experimental difficulties, quasi-resonant pulsed excitation of excitons inside the light cone, illustrated in the Figure 5, is attractive by the possibility to study the intrinsic properties of excitons, for example, the radiative lifetime τ_R [71]. The first theoretical calculations of τ_R excitons in GaAs-based QWs had rather large discrepancies. Hanamura provided an estimate of about 3 ps [72]. Andreani et al. estimated τ_R of about 25 ps for a heavy hole exciton (HH) in a 10-thick GaAs/Al$_x$Ga$_{1-x}$As QW nm [53], while the experiment revealed an order of magnitude longer times [73, 74]. Citrin showed that several parameters significantly affect the PL decay time [54]. In the case of free excitons, τ_R is determined only by Γ_0,

which is proportional to the exciton oscillator strength. The localization of excitons in the fluctuation potential leads to an increase in τ_R. In real systems, it is necessary to consider an ensemble of localized and free excitons, as a result of which the time τ_R will be determined by the ratio of particles in the ensemble. This allowance allows us to qualitatively explain the discrepancies in the published experimental results [73, 74].

Another important factor is the effect of dephasing due to elastic scattering of excitons on the PL decay time. The analysis shows that the time τ_R is directly proportional to the homogeneous width of the exciton resonance if the latter is much greater than the thermal energy kT [54] and than the exciton kinetic energy at the light cone edge. Such behavior was experimentally observed by direct measurement of PL decay by a streak camera [75]. The homogeneous linewidth was controlled via pumping the exciton reservoir by an additional pulsed laser. The PL kinetics clearly showed how τ_R firstly increases significantly with an increase in the exciton density and then decreases to the initial value as the exciton reservoir population decreased.

In the case of femtosecond pulsed resonant excitation, an ensemble of excitons initially possesses coherence, which decays due to scattering processes. It leads to a change in the exciton wave vector along the well plane, which, in turn, makes it possible to observe PL in directions different from the direction of transmission and reflection of the exciting light. Detection of the scatterred light showed that the PL kinetics exhibits not only the processes of exciton scattering and dephasing mentioned above, but also demonstrates quantum beats between light (LH) and heavy (HH) hole excitons [76]. The observation of beats indicates that the quasi-momentum scattering rate is much higher than the exciton dephasing rate in this case, and a change in the quasi-momentum does not lead to a change in the relative phase between the HH and LH excitons.

1.2.3 Reflection spectroscopy

In the previous section, it was shown that the emission of exciton PL is accompanied by intermediate processes before the act of photon emission: relaxation of energy and quasi-momentum in the nonresonant case and scattering of the quasi-momentum during resonant excitation. Reflection spectroscopy, on the contrary, does not imply the presence of additional processes besides the optical generation

of excitons and their subsequent direct radiative recombination. Reflection of light by an exciton layer in a QW is a coherent process, that is, it corresponds to the radiation produced by an ensemble of excitons that have retained their initial coherence. Therefore, constructive interference is observed only in the directions of transmission and reflection of the exciting light as a result of collective emission. The transmission is often difficult to measure experimentally due to the significant absorption of light in the sample substrate, while, as a rule, there is a thin layer with a thickness of no more than 1 μm in the direction of reflection from the QW layer.

A general idea of the reflection from a thin QW layer with an exciton resonance ω_0 can be obtained in a framework of the model of an ensemble of classical Lorentz atomic oscillators interacting with monochromatic electromagnetic wave with frequency ω. Electric susceptibility χ has a pole singularity [77]:

$$\chi(\omega) = \frac{Ne^2}{\varepsilon_0 m_0} \frac{1}{\omega_0^2 - \omega^2 - i\gamma\omega}, \tag{3}$$

where γ - damping rate of atomic oscillators, N - density of them and m_0 - electron mass in atom. In the vicinity of the resonance one can consider $\omega \approx \omega_0$.

$$\chi(\omega) = \frac{Ne^2}{\varepsilon_0 m_0 2\omega_0} \frac{1}{\omega_0 - \omega - i\gamma/2} = \frac{\chi_0}{\omega_0 - \omega - i\tilde{\gamma}}, \ \chi_0 = \frac{Ne^2}{\varepsilon_0 m_0 2\omega_0}, \ \tilde{\gamma} = \gamma/2 \tag{4}$$

From the Maxwell's equations, one can obtain an expression for the reflection coefficient of a plane wave incident normally on a thin layer with a susceptibility $\chi(\omega)$:

$$R(\omega) = \frac{\Gamma_R^2}{(\omega - \omega_0)^2 + (\Gamma_R + \tilde{\gamma})^2}, \ \Gamma_R = k\chi_0/2. \tag{5}$$

The reflection spectrum has a single resonance centered at ω_0. Resonant feature has Lorentzian shape with half-width of $\Gamma_R + \tilde{\gamma}$. Indeed, this is a quite simplified approach, but its result coincides qualitatively with the results of more of rigorous approaches, such as the interaction of a linearly polarized wave with two-level oscillators located in a thin medium [78, 79], solution of the wave equation with a non-local dielectric response, as well as quantum perturbation theory and other methods [9, 53]:

$$r_{QW}(w) = \frac{i\Gamma_0}{\widetilde{\omega}_0 - \omega - i(\Gamma_0 + \Gamma)} \tag{6}$$

Here Γ_0 is the radiative polarization decay rate (radiative width), Γ is the nonradiative dephasing rate, $\widetilde{\omega}_0$ is the renormalized exciton resonance frequency. When light is incident normally on a sample with a QW, one has to take into account the interference of the signal with light reflected from the smooth surface of the sample. If exciting light is polarized along the plane of incidence (p-polarization), the reflection from the sample surface disappears at the Brewster angle of incidence [79], and the measured reflectivity spectrum R contains only the response from the QW:

$$R = |r_{QW}|^2 = \frac{\Gamma_0^2}{(\widetilde{\omega}_0 - \omega)^2 + (\Gamma_0 + \Gamma)^2} \tag{7}$$

The method is attractive due to its experimental simplicity, while it makes it possible to obtain a rich set of information about the processes of dephasing of an ensemble of excitons. Γ_0 is determined by the exciton oscillator strength and is inversely proportional to the radiative lifetime $\tau_0 = 1/(2\Gamma_0)$. The method is actively used for characterization, determination of the dependence of the exciton oscillator strength on the quantum well thickness [80–82] and for identification of the exciton dephasing mechanisms [79, 83]. These studies have shown that, in high-quality samples with GaAs-based QWs, the inhomogeneous broadening of an ensemble of excitons is comparable to the radiative width and may even be smaller. Therefore, in such structures at low temperatures and low excitation regime, the main contribution to the irreversible phase relaxation of excitons comes from radiative recombination.

In the previous section, it was shown that the resulting exciton PL decay rate depends on many factors. Reflection spectroscopy makes it possible to separate the radiative and non-radiative contributions to phase relaxation. Experimental study of the radiative relaxation rate of excitons Γ_0 in a high-quality QW did not revealed significant change in the exciton oscillator strength, directly proportional to Γ_0, either with an variation of temperature in the range of 8-50 K or with photoinduced non-radiative broadening of the exciton resonance [79].

In case of excitation by ultrashort laser pulses, the width of the exciton line of the reflectivity spectrum is related to the kinetics of signal decay via the Fourier transform. One can obtain the temporal evolution of the polarization decay by performing such transformation, result of which coincides with the direct measurement of the free induction decay [83]. In this case, the characteristic decay time of the direct measurement and the Fourier-transformed reflectivity spectrum coincide and correspond to the inverse of the width of the reflectivity contour, which is
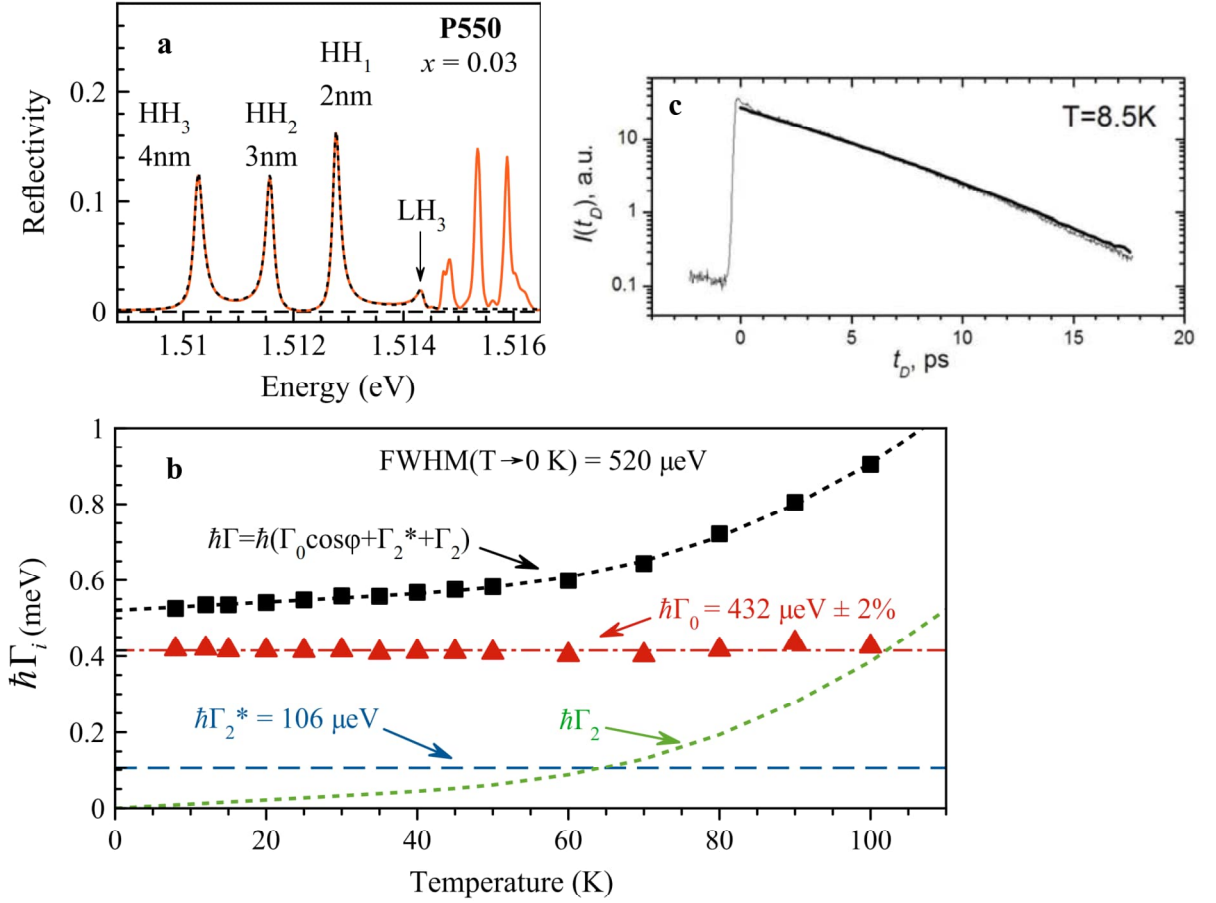
Figure 6: (a) Reflectivity spectrum measured at the Brewster angle of incidence from the samples with a thickness of 2, 3 and 4 nm. The fit by linear combination of equations (7) is plotted by dash line. (b) Decomposition of dephasing rate into radiative rate (red), reversible non-radiative rate (blue) and irreversible non-radiative rate (green). Imported from [81]. (c) Temporal profile of free polarization decay (thin) and Fourier transform of the reflectance spectrum (thick). Imported from [83].

determined by the total dephasing rate $\tau_{FID} = (\Gamma_0 + \Gamma)^{-1}$. Thus, reflection spectroscopy is a powerful tool for studying the coherent optical dynamics of excitons in nanostructures.

1.2.4 Pump-Probe reflection spectroscopy

The use of pump-probe nonlinear technique in reflection spectroscopy is of particular interest. The point of the method is illustrated in the figure 7. The technique consists in initial optical pumping of the system by strong high-power laser pulse and subsequent time-resolved detection of a change in the reflection of weak probe illumination. The technique basically reveals many-body interactions of excitons with excitons, phonons and charge carriers [84]. Variations of the method have been

Figure 7: Sketch of pulsed experimental Pump-Probe method.

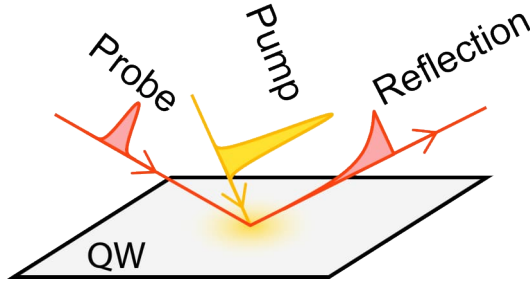actively used to study the effect of electron-hole plasma on exciton resonances in GaAs/AlGaAs QWs, the effects of phase space filling, and bandgap renormalization [85]. We are interested in the case, when the reflection spectrum of femtosecond probe pulse reveals (probes) the kinetics of transient processes induced by pump pulse via the indirect effect of pumping on the probe response.

The method was used to study the dynamics of a reservoir of excitons with a large wave vector [86, 87]. Direct radiative recombination is not possible for such type of dark excitons, since they are outside the light cone (see figure 5). As a result, excitons in the reservoir have a relatively long nanosecond-scale relaxation times. In this case, the reservoir has a significant effect on optically active bright excitons through scattering processes, which must be taken into account, for example, when considering various coherent control protocols. The dynamics of dark excitons was studied by detection of additional non-radiative broadening of exciton lines in the reflection spectrum of probe pulse induced by strong pump pulse. Measurements have revealed the dependence of the dynamics on the reservoir generation method. In particular, in case of the generation of a reservoir of dark excitons inside the QW layer, the dynamics of broadening (and, accordingly, the dynamics of the concentration of the reservoir) exhibited a rapid initial decay followed by a long-lived decay with a characteristic time longer than the laser pulse repetition period. The long-lived signal was attributed to the accumulation of a reservoir of dark excitons. The relaxation of the reservoir population has been described using a kinetic model that takes into account both resonant and nonresonant excitation.

Further development of the technique led to the observation of the spin dinamics of dark excitons in the reservoir [67]. It was shown that dark excitons cause the spectral shift of the lines corresponding to the recombination of brigth excitons via the exchange interaction. It turned out that the spectral shift can be controlled

by applying an external transverse magnetic field, which causes the Larmor precession of the long-lived exciton spin from the reservoir. To observe the effect, it was necessary to select a sample with a very high quality QW, since the oscillating spectral shift of the lines occurred on a scale of the order of 10 μeV.

The pump-probe technique is mainly used to study many-body interactions as was shown. The response of probe excitation is indirectly sensitive to the effects of pumping via the intermediate process under study. In this case the optical coherence created by the pump pulse is not conserved and thus is not taken into account. However, an interesting case is when the probe excitation can reveal directly the coherent response of the system to pump pulse. Such technique was used to observe quantum beats between the quantum-confined states of excitons in a QW [88]. A spectrally-broad pump pulse, which cover several excitonic resonances, excites a coherent superposition of a multilevel exciton system. The created coherence of several exciton levels, described by a set of off-diagonal elements of the exciton density matrix, experiences oscillations (beats) at frequencies corresponding to transitions between exciton levels. Electric field of the probing pulse coherently interact with the same exciton ensemble that was excited by the pump pulse. The secondary emission emerging in the reflection geometry of the probe pulse exhibits quantum beats in the form of a dependence of the amplitude of reflected light at exciton spectral lines on the time delay between the pump and probe pulses. This experiment is remarkable in the combination of the pump-probe concept and the theoretical approach used to describe coherent processes like four-wave mixing.

1.3   Four-wave mixing and photon echo

The above approaches can be used in both linear mode and non-linear excitation regime. They can be characterized by relative experimental simplicity, on the one hand, and often complex data interpretation, on the other hand. For example, in case of significant inhomogeneous broadening of spectral lines, it is impossible to obtain information about individual emitters that form an inhomogeneous ensemble, that is, information about a homogeneous linewidth. The advantage of fundamentally nonlinear optical techniques is the ability to circumvent the limitations of linear methods. Moreover, optical nonlinearity is fundamentally essential for the potential implementation of coherent control protocols.

The essence of the phenomenon is the emergence of a new electromagnetic wave as a result of the joint interaction of three electromagnetic waves with an optically active nonlinear medium. Next, we consider a nonlinear optical method for studying ultrafast coherent optical dynamics, which is based on the phenomenon of four-wave mixing (FWM). The point of the phenomenon is that the joint interaction of three electromagnetic waves with an optically active nonlinear medium give rise to the emergence of a new fourth electromagnetic wave. The wave vector and frequency of the fourth wave are determined by all exciting waves. The intensity of the process is determined by the third-order nonlinear electric susceptibility $\chi^{(3)}$. The variety FWM effects is described in detail in monographs [17, 20]. We will consider degenerate type of FWM, in which the frequency of the all exciting waves is the same. Let us limit ourselves to thin optically active semiconductor layers with exciton resonances as the medium.
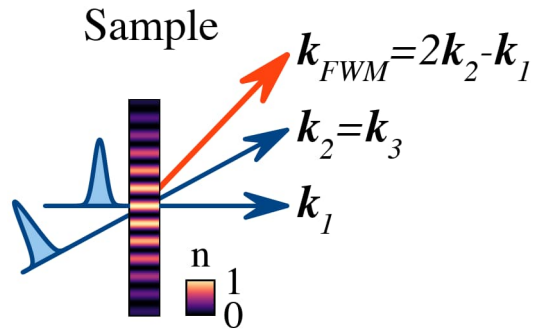
Figure 8: Schematic of FWM phenomena resulting from excitation of a thin medium by a sequence of two laser pulses with an illustration of population grating n.

In order to study transient ultrafast coherent phenomena, the excitation is performed by a sequence of femto- or picosecond laser pulses. Moreover, pulse technique is used thanks to the extremely high amplitude of electric field in the pulse, which is necessary for reliable detection of nonlinear response. Figure 8 illustrates a typical experiment in transmission geometry. The first pulse with the wave vector $\vec{k}_1$ excites a thin layer of oscillators (excitons in our case) and as result macroscopic polarization is created with a phase determined by the vector $\vec{k}_1$. The second pulse with the wave vector $\vec{k}_2$ also creates polarization in the medium, which spatial distribution is determined by the vector $\vec{k}_2$. The interaction of the polarization with the electromagnetic field of the second exciting pulse leads to the creation of a spatial population grating of the excited oscillators. This means that the optical properties of the medium become spatially modulated with a period determined by

the difference $\vec{k_2} - \vec{k_k}$. In turn, the third-order polarization induced by the third pulse with vector $\vec{k_3}$ will depend on the population grating and contain components characterized by the combination of wave vectors $\vec{k}_{FWM} = \vec{k_3} \pm (\vec{k_2} - \vec{k_1})$. These polarization components correspond to the coherent FWM response emitting in the phase-matching directions $\vec{k}_{FWM}$. Usually, self-diffraction of the second beam $\vec{k_3} = \vec{k_2}$ is considered as the third beam, and the FWM signal is detected in the direction $\vec{k_{FWM}} = 2\vec{k_2} - \vec{k_1}$.

The FWM phenomenon looks like a result of the diffraction of the third light beam on the interference grating created by the first two beams. Indeed, under the condition of spatial and temporal intersection of the beams, it is possible to obtain an interference pattern in the oscillators layer and thereby create a population grating. The population grating will lead to modulation of the optical properties of the layer (eg absorption) and the creating of an effective diffraction grating. The fundamental difference between such diffraction and the coherent FWM effect lies in the mechanism of formation of the population grating. In the FWM effect, the grating arises due to the nonlinear interaction of the electric field of one light beam with the polarization induced by another beam. The difference is clearly observed when using pulse technique. When the exciting pulses are separated in time, for example, using an optical delay line, interference does not occur, while the polarization is preserved even after the action of the pulse and decays with the phase relaxation time T_2.

The effects of diffraction by an interference grating were studied in periodic structures with QWs at room temperature [89, 90]. The spatially modulated photoexcitation of excitons and their subsequent ionization lead to the formation of an electron-hole plasma population grating. Manifestation of coherent dynamics of excitons under such conditions is not expected, however, the goal of such work was to search for strongly nonlinear media suitable for optical information processing at room temperature.

The FWM kinetics is determined by the nature of the system under study and by the excitation regime [18, 24, 91]. In the first approximation, this problem can be considered as the interaction of an ensemble of two-level systems with an electromagnetic field in the framework of the dipole approximation, using the density matrix formalism [91–94]. The problem will be considered in more detail in the next chapter. We just mention here that, depending on the experiment (two- or

three-pulse protocol), one can observe polarization decay kinetics, i.e., determine the irreversible dephasing time T_2, and the population decay kinetics of the excited state, i.e., determine the energy relaxation time T_1.

1.3.1 Relaxation processes studied by four-wave mixing and photon echo

The FWM technique makes it possible to obtain a fruitful information on the mechanisms of the loss of exciton optical coherence created by ultrashort optical excitation. Real systems always possess fluctuations in exciton level energy, which lead to fluctuations in the resonant frequency of the optical transition and to inhomogeneous broadening of spectral lines. After pulsed excitation of an inhomogeneous ensemble, the relative phase between individual emitters will increase with time, which will lead to a loss of ensemble coherence (phase relaxation). The characteristic time of such dephasing T_2^* is inversely proportional to the inhomogeneous broadening. Such a process limits the coherent linear response, which is observed, for example, in free induction decay experiment [83]. However, the coherence of individual emitters is preserved, so such dephasing process is reversible. In the FWM protocol, the ensemble of emitters also experiences relative dephasing that occurs after the action of the first pulse. However, the action of the second, so-called rephasing pulse, which is delayed with respect to the first one by a time delay τ_{12}, leads to an inversion of the relative dephasing, i.e. rephasing. Therefore, at time $2\tau_{12}$ after the arrival of the first pulse, all the oscillator in ensemble become in phase again, and a macroscopic polarization with the wave vector $\vec{k}_{FWM}$ appears. Such a FWM signal is called a photon echo [22] by analogy with a spin echo [95]. The main advantage of PE protocol is that one can work around the reversible dephasing. The rest mechanisms of decoherence of an individual emitter are irreversible and are characterized by an irreversible dephasing time T_2. Among them, many-body interactions such as elastic and inelastic scattering play the main role [23, 96].

The irreversible dephasing rate $\Gamma_2 = \frac{1}{T_2}$ determines the homogeneous width of the spectral line. The inhomogeneous broadening is usually much larger than the homogeneous width, in which case linewidth of the absorption or reflection spectrum is governed by inhomogeneous broadening. The advantage of PE method is the ability to distinguish the several contributions to the dephasing and determine

the homogeneous width hidden in linear spectroscopy.

In the case of a homogeneous ensemble, the signal is a decaying exponential function of the time delay between pulses with a characteristic time T_2 when scanning the delay between pulses 1-2 τ_{12} or T_1 when scanning the delay between pulses 2-3 τ_{23} (applicable only for the three-pulse experiment) [18]. When an inhomogeneous ensemble is excited by an ultrashort pulse, the temporal profile of the echo signal is a Gaussian peak centred at the time $2\tau_{12}$ for the two-pulse experiment and at $2\tau_{12} + \tau_{23}$ for the three-pulse experiment. When scanning the delay τ_{12} The time-integrated FWM signal (TI-FWM) decays with different decay constant depending on whether the ensemble is homogeneously or inhomogeneously broadened [23, 24]. It leads to the problem of interpreting TI-FWM data. On the other hand, the time-resolved technique (TR-FWM), which we use in this work, provides an unambiguous result, since the detected signal reveals the temporal profile of the FWM. Moreover, the temporal resolution allows us to effectively filter the desired signal from parasitic scattering of different nature.

The FWM technique was first applied to semiconductor structures in order to study the basic properties of coherent optical dynamics. The FWM in GaAs/AlGaAs QW at low temperatures was observed for the first time by Hegarty and colleagues [97]. The signal spectrum had a pronounced resonance in the vicinity of the exciton transition. The pulses creating the grating were overlapped in time, so no information about dephasing was obtained. In subsequent work, TR-FWM measurement revealed that the signal was a PE [98]. The results were qualitatively described using the model of an inhomogeneous ensemble of two-level systems [92], however the extracted dephasing time T_2 had a significant spread within the exciton spectral line. Early studies of FWM from excitons in a GaAs epitaxial layer [99] and a single QW [100] also showed coherent dynamics on picosecond timescale, as shown in figure 9(a). The corresponding homogeneous width, which is proportional to $\frac{1}{T_2}$, coincided with the width of the absorption spectrum (figure 9(b)). This means that the ensemble of delocalized excitons in the QW was predominantly uniformly broadened due to significant scattering of excitons by defects and acoustic phonons.

Exploiting of FWM made it possible to separate various contributions to the dephasing of excitons by conducting temperature experiments [100, 101], from which influence of scattering on the reservoir of incoherent excitons and free charge carriers was determined [102, 103]. Scattering on charge carries turned out to be much

stronger than exciton-exciton scattering, and both mechanisms are more pronounced in the quasi-two-dimensional case compared to the three-dimensional one.
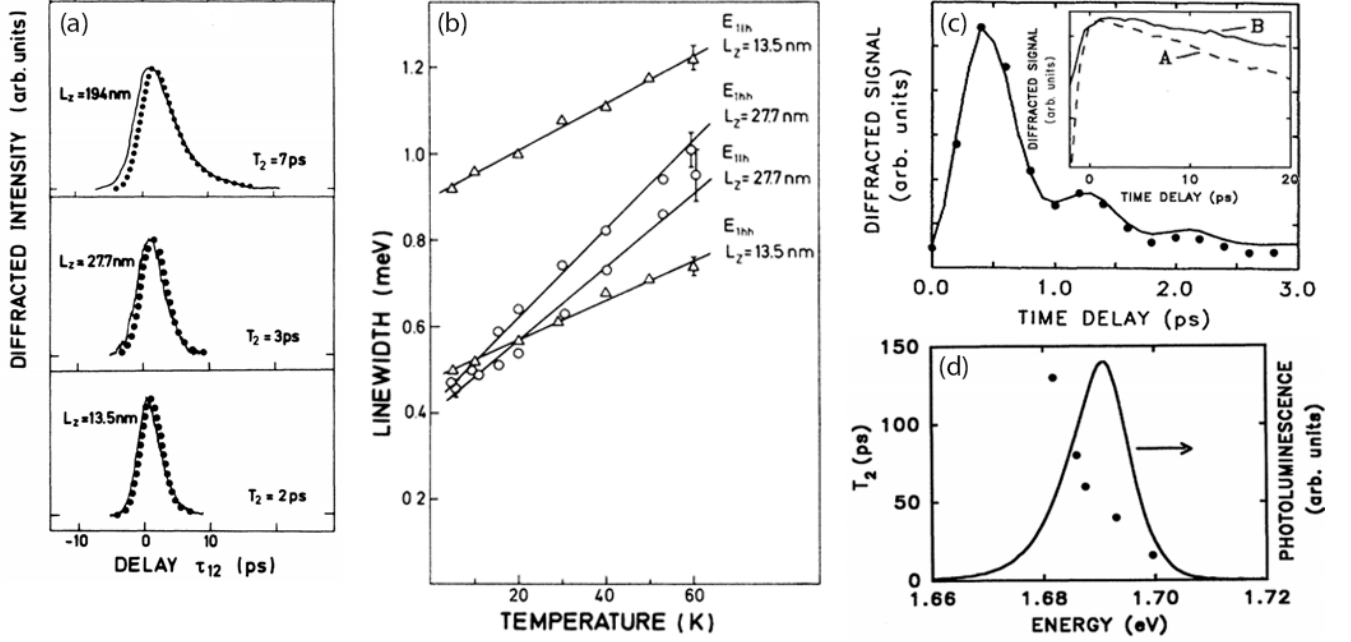

Figure 9: (a) FWM signal as a function of delay τ_{12}, measured in the bulk and two QWs. (b) Temperature dependence of the homogeneous width of the absorption spectrum. From [100]. (c) FWM as a function of the delay under femto and picosecond (inset) excitation. (d) Spectral dependence of the dephasing time T_2 across the exciton photoluminescence line. From [104].

The inevitable fluctuations of the QW quantizing potential significantly affect the coherent optical dynamics [96]. In case of a large inhomogeneity, the difference between the femto- and picosecond FWM techniques is clearly manifested [104]. Under spectrally broad femtosecond excitation, not only localized but also free excitons are excited, which manifests itself as beats in the signal kinetics (figure 9(c)). In addition to beats, a long-lived non-oscillating component was observed. Its origin could only be established by means of spectrally narrow picosecond excitation, which revealed a significant spread in the dephasing time by an order of magnitude within the exciton spectral line (figure 9(d)). An increase in the degree of localization of quasiparticles reduces the probability of scattering [105], which leads to longer coherence time. Thus, the picosecond FWM can be an effective tool for probing the localization of excitons on potential fluctuations, which we will extensively use further in this work.

The temporal profile of FWM signal exhibits oscillations due to quantum beats which appear under simultaneous excitation of two or more exciton resonances. Such

quantum beats between exciton states with light (LH) and heavy (HH) holes [104, 106–109] have been observed using FWM technique. The phenomenon was theoretically described using the three-level model [110]. The beat frequency corresponds to the energy splitting between the excited states. The nonlinear nature of the signal makes it possible to distinguish oscillations caused by polarization interference of electromagnetic waves emitted by two independent systems from interference of the quantum states of a single system [108]. A QW with pronounced HH and LH resonances was used to demonstrate the possibility of reconstruction of the FWM temporal profile through the Fourier transform of amplitude and phase spectra of the signal [109]. The proportion of excited states in the coherent superposition changes while scnanning excitation wavelength, which led to beats in the FWM time profile at the HH-LH splitting frequency. An oscillating behavior of the FWM signal was also observed under excitation of a pair of free and bound excitons [111], an exciton-biexciton pair [112, 113], and other systems as well [23].

In the case of studying the selected ensemble of quasiparticles, it is worth to utilize the picosecond technique instead of spectrally broad femtosecond pulses. Otherwise several resonances are excited simultaneously, resulting in a multi-component FWM signal, the interpretation of which may be complicated [114]. Moreover, excitation-induced dephasing and higher-order nonlinear effects arise due to the extremely high instantaneous amplitude of the femtosecond pulse. On the contrary, picosecond pulses make it possible to address ensemble of quasiparticles selectively and to supress many-body effects. Suppression of the dephasing mechanisms leads to an increase in the coherence time to tens of picoseconds in [115] QWs and hundreds of picoseconds in [116] QD ensembles, so there is no lack of time resolution.

Recently, FWM and PE have been widely used to study the coherent dynamics of excitons in promising materials, such as nanostructures based on zinc oxide [101], gallium nitride [117], monolayers of transition metal dichalcogenides [118–120] and halide perovskites as well [121–123]. Chapters 3 and 4 of the dissertation are also devoted to the study of coherent dynamics in little-studied structures.

The PE technique is used to develop protocols for the all-optical coherent control of exciton complexes. The fundamental manifestation of coherent manipulation is Rabi oscillations in the PE signal [24]. In accordance with the optical Bloch equations, the population of the excited states harmonically depends on the area of the pulses. Rabi oscillations in the PE signal were demonstrated in QWs [24, 115] and

QDs [116, 124–126]. A peculiarity of excitation of an inhomogeneously broadened ensemble by relatively long picosecond pulses [125] appeared in the regime of Rabi oscillations. Oscillators with a significant detuning from the laser pulse frequency experience additional reversible dephasing during the action of the pulse. Dephasing leads to a change in the arrival time of the PE in comparison with the classical case - the *Hann* echo. Such temporal shifts must be taken into account when considering protocols for coherent control of the exciton ensemble, where precise timing of the pulses is important. Further studies have demonstrated ability of manipulation of the PE shift by applying an additional control pulse which compensates the relative dephasing of emitters [116].

1.3.2   Spin-dependent photon echo

The introduction of magnetic phenomena into a purely optical PE protocol has significantly expanded the possibilities of coherent control and led to the emergence of a new trend of coherent optical dynamics - spin-dependent photon echo [24]. Consideration of both optical and magnetic effects makes it possible to combine the advantages of each of them and achieve fast optical coherent manipulation with long-lived spin storage.

In a spin-dependent PE experiment, an external magnetic field perpendicular to the direction of light (Voigt geometry) causes the spins of quasiparticles oriented by the first optical pulse to precess around the magnetic field vector at the Larmor frequency [127]. The experiment protocol is shown in the figure 10(d). By the time of the precession half-cycle, the magnetic field transfers the coherence between levels coupled by an optical transition into the so-called dark coherence between optically uncoupled levels. The second rephasing pulse arriving at this moment transfers the coherence either into pure spin coherence or into another dark coherence depending on polarization. Then, after one more half-cycle of the Larmor precession, the magnetic field transfors again dark coherence into bright one, so that PE emission is possible. Therefore, when scanning the delay between pulses the PE signal exhibits beats at the Larmor frequency, which was first demonstrated on trions in a CdTe/CdMgTe QW [127]. The decay kinetics of the spin-dependent PE amplitude are shown in the figures 10(a) and (b). The problem is fundamentally different from the previously mentioned cases of quantum beats, in which the energy spacing between states and frequency are rigidly determined by the growth parameters of
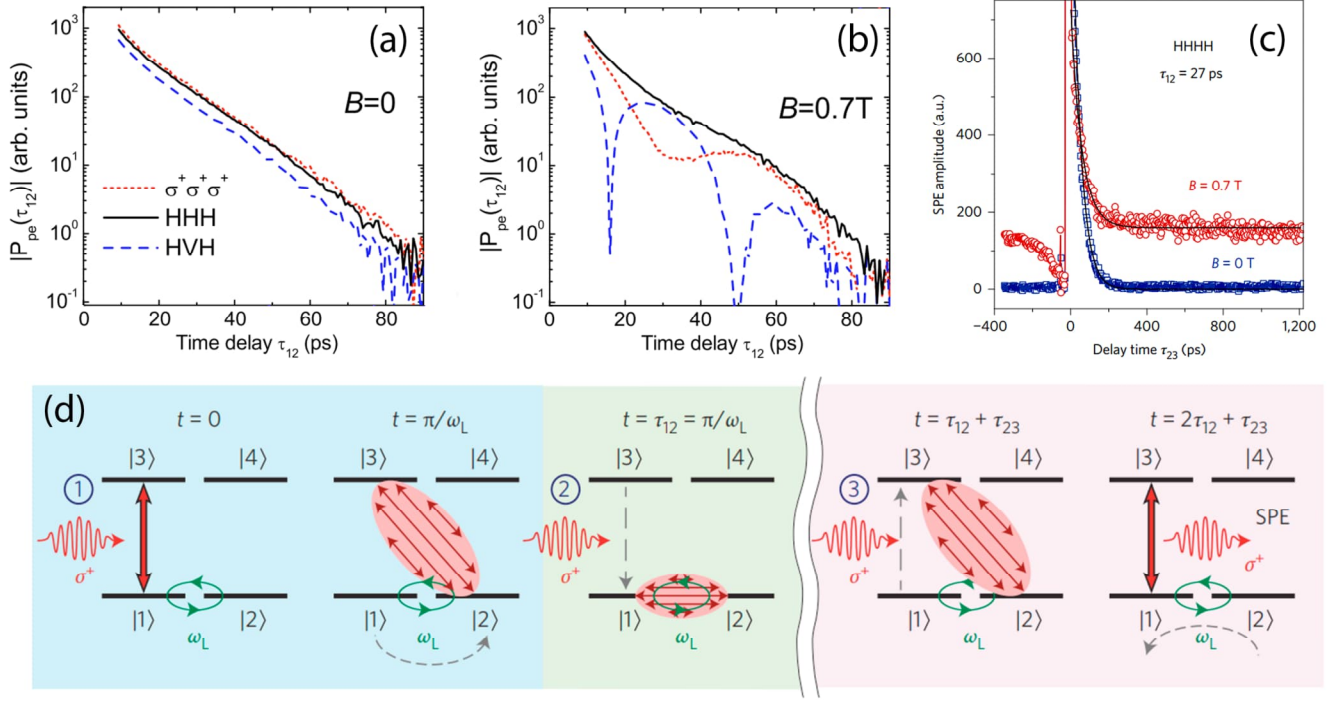
Figure 10: PE decay kinetics at zero magnetic field (a), at $B = 0.7$ T (b). (c) Three-pulse PE decay kinetics (SPE) . (d) Protocol for action of light pulses on a four-level electron-trion system and magnetic-field-induced oscillations which occur between pulses. Red arrows corresponds to coherences. In [127] only first two pulses were used (a-b), while all of them were used in [128] (c-d).

the structure. The introduction of an external magnetic field into the PE protocol provides a new degree of freedom, which makes it possible to control the splitting of initially spin-degenerate states.

The most interesting scenario is associated with the transfer of optical coherence into the spin subsystem of ground electronic states. Microscopic spin coherence does not depend on the processes of fast optical dephasing or radiative recombination of exciton complexes. We can say that information about the light pulse is stored in the electron spin states, that is, it is recorded and frozen there. The storage time of spin coherence is determined only by spin dephasing processes, which, as a rule, are several orders of magnitude slower than optical dephasing. However, the question arises how to read this long-lived coherence. A three-pulse spin-dependent PE provides such an opportunity [128]. The third pulse with a particular polarization determined by the selection rules transfers the coherence from the spin subsystem back to the dark coherence between the ground and excited states in the same way as the second pulse does. Further, after a half-cycle of the Larmor precession (figure 10(d)) the magnetic field will transfer again the coherence to the bright configu-

ration, and the condition for the PE emission will be fulfilled. The implementation of such a protocol was demonstrated on trions in a CdTe/CdMgTe QW [128]. In a zero magnetic field, the three-pulse echo decayed with a trion lifetime $T_1 = 45$ ps, while in a presence of the magnetic field with a longitudinal spin relaxation time $T_1^e = 50$ ns exceeding by three orders of magnitude, as shown in the figure 10(c). As a result, the technique provides observation of three-pulse PE signal at times significantly exceeding the trion lifetime, which can be used to implement optical memory in nanostructures.

Since the key feature of the spin-dependent PE is the Larmor precession, the method provides a rich set of information about the spin properties of quasiparticles. The oscillation frequency depends on the value of the electron and hole g factor in a trion, which can be extracted by measuring the PE signal at different magnetic fields. Measurements of multiple beats in the PE decay kinetics for different sample orientation relative to the magnetic field revealed not only the presence of the electron and hole g factors [129], but also made it possible to determine hole anisotropy in the CdTe/CdMgTe QW [130] and in InGaAs/GaAs QDs [131]. It should be noted that, in contrast to the Kerr rotation technique, which is widely used to determine the g factor, a two-pulse spin-dependent PE is formed only by those quasiparticles that have retained their optical coherence. Also, the two methods manifest local spin dynamics in a different way - it turned out that the hopping of resident electrons leads to a reduction in the decay time of the PE signal, and, conversely, to an increase in the transverse spin relaxation time due to averaging of the fluctuating nuclear field [132].

2D Fourier spectroscopy technique has been actively developed in recent years [133]. It was additionally introduced into spin-dependent PE to study the Zeeman splitting of trions and excitons localized on a neutral donor in a QW [134]. The method provided determination the difference between Zeeman splitting of donor bound electrons and those localized at potential fluctuations in the range of fractions of μeV, which is two orders of magnitude smaller than the homogeneous width of optical transitions.

The mentioned works were devoted either to the study of trions or donor-bound excitons. Therefore, these protocols for long-lived spin-dependent PE require a sufficient doping level to obtain a relatively large oscillator strength. From the point of view of the PE study, these quasi-particles are equivalent, since both are

described by a four-level model with a doubly degenerate ground state and two excited states. In the absence of a magnetic field, when excitation with circular polarization is used, one can select two non-interacting two-level subsystems. Neutral excitons in nanostructures are usually described using a five-level model consisting of a non-degenerate ground state of a crystal and two doublets of optically bright and so-called dark excitons, optical transitions to which are spin-forbidden. A simplified model that does not include dark states is a V-system. The fundamental difference between the energy level structure of excitons and trions manifests itself in the polarimetry of the classical PE. The signal from two ensembles has qualitative and quantitative difference [122, 135]. The spin-dependent PE dynamics is significantly different as well. In a two-pulse Larmor experiment, the precession of electron and hole spins in an exciton mixes the bright and dark exciton states, that was was considered theoretically [136]. The mixing is assumed to make two-pulse PE decay kinetics oscillate, however, it was no confirmed experimentally until the present work. The protocol for a long-lived spin-dependent PE shown in figure 10(d), cannot be directly implemented on an exciton ensemble, since there is no spin degeneracy of the ground state.

1.4 Conclusions and objectives of the dissertation

The chapter was devoted to analyze how the ultrafast optical dynamics of excitons in semiconductor nanostructures manifests itself in various linear and nonlinear optical regimes. An literature review has shown that the exciton intrinsic properties, such as the optical coherence time, energy relaxation, and the value of inhomogeneous broadening, are most clearly manifested in PE experiment. In some cases photon echo being a nonlinear optical tool for studying coherent optical dynamics has a lot of advantages over linear spectroscopic methods. FWM and PE have already demonstrated their fascination during the study of the optical properties of excitons in classical gallium arsenide based systems. The presented works on the study of excitons in novel materials also confirmed the high potential of the technique. The fundamental feature of PE is the possibility of implementing protocols for coherent control of an exciton ensemble, which was discussed in the final part of the review.

The aim of this dissertation is to develop coherent control of excitons and

excitonic charged complexes by means of photon echo. The development is proposed in two ways - the application of the method to the study ultrafast coherent dynamics in promising novel semiconductor nanostructures, as well as the development of protocols for coherent control of optical excitations based on the spin-dependent photon echo.

Chapter 2. Theoretical and experimental approaches for studying photon echo from excitons in nanostructures

The chapter describes the theoretical and experimental approaches that will be used to study the photon echo from ensembles of excitons and trions in layered nanostructures with quantum wells. The chapter describes the evolution of a two-level system interacting with an electromagnetic field in the framework of the density matrix formalism, considers the photon echo protocol for an inhomogeneous ensemble of two-level systems, and gives a illustrative interpretation using the Bloch sphere. It is shown what kind of the original problem is necessary to describe the photon echo signal from ensembles of excitons and trions, taking into account the fine structure and selection rules; a special attention is paid to spin effects in the photon echo. The final part of the chapter is devoted to a detailed description of the experimental setup and signal detection technique used in the work. A scheme of the optical setup for a picosecond two-pulse spin-dependent photon echo is presented, and the features of optical heterodyne detection are described.

2.1   Theory of the photon echo from ensemble of two-level systems

Let us consider the effects of FWM and PE in semiconductor nanostructures with a thin optically active layer. The nonlinear susceptibility is determined by the internal microscopic electronic structure of the system, so it is natural to use the quantum mechanical approach to calculate it. Analysis is done using the density matrix formalism, the evolution of which is determined by the Lindblad equation. Microscopic expressions for nonlinear susceptibilities and the corresponding nonlinear polarizations are considered in detail in the monograph by I. R. Shen [20].

An excitonic ensemble in nanostructures usually has a pronounced and quite isolated optical resonance, which allows us to leave the rest optical transitions out of the consideration and use a simplified model of an ensemble of two-level systems (TLS). The monograph by L. Allen and J. Eberly [94], as well as chapters in the works [18, 32, 40, 137] are devoted to the analysis of the coherent dynamics of two-level atoms. In our case, the ground level of the TLS corresponds to the ground state of the crystal, and the upper level corresponds to the excited state with one

exciton. The exciton state is a meta-stable state due to the presence of radiative and non-radiative relaxation channels. To describe the processes of phase and energy relaxation, phenomenological terms are introduced into the Lindblad equation. Let us further consider the basics of the theoretical approach for description of the PE experiments which is based on the works [18, 94, 138].

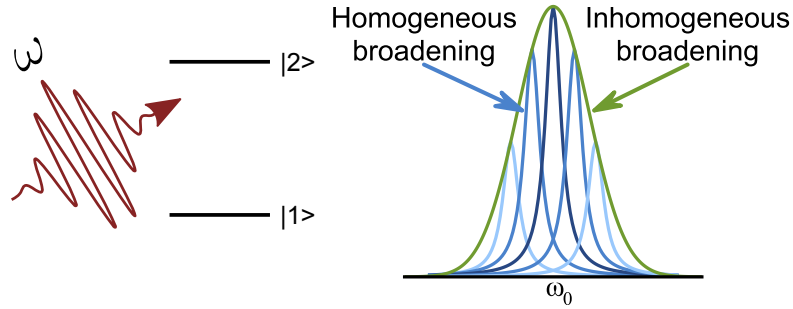### 2.1.1 Dynamics of the two-level system in an external electromagnetic field

Figure 11: Schematic representation of a two-level system interacting with a laser pulse with a carrier optical frequency ω. Inhomogeneous distribution of resonances of two-level systems with a homogeneous width in the vicinity of the central transition frequency ω_0.

To analyze the coherent dynamics of an ensemble of excitons in nanostructures, we use the model of an inhomogeneous ensemble of TLS. The interaction of such a system with a laser pulse is schematically shown in figure 11. Despite a rather strong simplification, the model correctly describes the main phenomena observed in the FWM, and also it predicts subtle effects when additional mechanisms are introduced. The purpose of this section is to demonstrate the general picture of coherent interaction using a minimal sufficient theoretical formalism. The approach can be futher developed to solve specific particular problems. The main conclusions of this section are reflected in our publication [138].

The evolution of a quantum system is determined by solving the von Neumann equation as described in A.1:

$$i\hbar \frac{\partial \rho(t)}{\partial t} = [H(t), \rho(t)], \tag{8}$$

where ρ - density matrix of the system. Density matrix formalism is described in the

appendix A.1. The matrix of unperturbed Hamiltonian of the TLS $\hat{H}_0$ is diagonal in the basis of its eigenstates:

$$\hat{H}_0 = \begin{pmatrix} 0 & 0 \\ 0 & \hbar\omega_0, \end{pmatrix} \tag{9}$$

where ω_0 is the frequency of the optical transition between the ground and excited states of the TLS, which has an inhomogeneous spread in the TLS ensemble. Assume that such a transition is allowed in the dipole approximation, then the Hamiltonian describing interaction between TLS and an electromagnetic field $\hat{V} = -\hat{d}E$ is given by:

$$\hat{V} = -\begin{pmatrix} 0 & d^* E_0^* e^{i\omega t} \\ dE_0 e^{-i\omega t} & 0 \end{pmatrix}, \tag{10}$$

where $d = \langle 2|\hat{d}|1\rangle$ is the matrix element of the dipole moment operator $\hat{d}$ corresponding to the transition from state 1 to state 2, E_0 is the amplitude of the plane electromagnetic wave with frequency ω. Then the total Hamiltonian $\hat{H} = \hat{H}_0 + \hat{V}$ is

$$\hat{H} = \begin{pmatrix} 0 & -d^* E_0^* e^{i\omega t} \\ -dE_0 e^{-i\omega t} & \hbar\omega_0 \end{pmatrix}, \tag{11}$$

For every TLS there is a 2×2 density matrix ρ whose evolution is determined by the von Neumann equation (8). The off-diagonal terms of the Hamiltonian contain terms oscillating at the optical frequency, which makes the differential equations more complicate. Such sticking point can be bypassed by a following modification, which is equivalent to a transition to a rotating reference frame [18, 94]. Let us introduce an auxiliary matrix M:

$$M = \begin{pmatrix} 0 & 0 \\ 0 & \omega \end{pmatrix}, \tag{12}$$

by which we transform ρ:

$$\tilde{\rho} = e^{iMt}\rho e^{-iMt} = \begin{pmatrix} 1 & 0 \\ 0 & e^{i\omega t} \end{pmatrix} \begin{pmatrix} \rho_{11} & \rho_{12} \\ \rho_{21} & \rho_{22} \end{pmatrix} \begin{pmatrix} 1 & 0 \\ 0 & e^{-i\omega t} \end{pmatrix} = \begin{pmatrix} \rho_{11} & \rho_{12}e^{-i\omega t} \\ \rho_{21}e^{i\omega t} & \rho_{22} \end{pmatrix}. \tag{13}$$

One can obtain the von Neumann equation by differentiating $\tilde{\rho}$ and taking into

account (8):

$$i\hbar\frac{\partial\tilde{\rho}}{\partial t} = [\underbrace{e^{iMt}\hat{H}e^{-iMt}}_{\hat{\tilde{H}}} - \hbar M, \tilde{\rho}] = [\hat{H}_{eff}, \tilde{\rho}]. \tag{14}$$

Then the matrix of the transformed Hamiltonian $\hat{H}_{eff}$ does not contain rapidly oscillating terms:

$$\hat{H}_{eff} = \begin{pmatrix} 0 & -d^*E_0^* \\ -dE_0 & \hbar\omega_0 \end{pmatrix} - \hbar\begin{pmatrix} 0 & 0 \\ 0 & \omega \end{pmatrix} = \begin{pmatrix} 0 & -d^*E_0^* \\ -dE_0 & \hbar\Delta \end{pmatrix} = \hbar\begin{pmatrix} 0 & \Omega^*/2 \\ \Omega/2 & \Delta \end{pmatrix}, \tag{15}$$

where $\Omega = \frac{-2dE_0}{\hbar}$ is the Rabi frequency $\Delta = \omega_0 - \omega$ is the detuning between driving field and resonance. Thus, we have obtained the von Neumann equation for the transformed density matrix and the effective Hamiltonian, which does not depend explicity on time. Let us rewrite (14) in the following form:

$$\begin{pmatrix} \dot{\tilde{\rho}}_{11} & \dot{\tilde{\rho}}_{12} \\ \dot{\tilde{\rho}}_{21} & \dot{\tilde{\rho}}_{22} \end{pmatrix} = -i\begin{pmatrix} \frac{\Omega^*}{2}\tilde{\rho}_{21} - \frac{\Omega}{2}\tilde{\rho}_{12} & \frac{\Omega^*}{2}(\tilde{\rho}_{22} - \tilde{\rho}_{11}) - \Delta\tilde{\rho}_{12} \\ \frac{\Omega}{2}(\tilde{\rho}_{11} - \tilde{\rho}_{22}) + \Delta\tilde{\rho}_{21} & \frac{\Omega}{2}\tilde{\rho}_{12} - \frac{\Omega^*}{2}\tilde{\rho}_{21}) \end{pmatrix}. \tag{16}$$

These differential equations for the density matrix elements are called the optical Bloch equations. Since $\hat{H}_{eff}$ does not explicitly depend on time, the evolution of $\tilde{\rho}(t)$ can be determined in terms of the initial state of the original density matrix $\tilde{\rho}(0)$ according to A.1 (see equation 67):

$$\tilde{\rho}(t) = e^{-(i/\hbar)\hat{H}_{eff}t}\tilde{\rho}(0)e^{(i/\hbar)\hat{H}_{eff}t}, \tag{17}$$

from which evolution of the original $\rho(t)$ can be obtained:

$$\rho(t) = e^{-iMt}e^{-(i/\hbar)\hat{H}_{eff}t}e^{iMt}\rho(0)e^{-iMt}e^{(i/\hbar)\hat{H}_{eff}t}e^{iMt} \tag{18}$$

2.1.2 The action of an ultrashort laser pulse

Let us consider the action of a ultrashort rectangular laser pulse of duration t_p on a two-level system, at which the phase shift due to the detuning $\Delta \cdot t_p \ll 1$ can be neglected. Then the Hamiltonian $\hat{H}_{eff} \to \hat{H}_l$ contains only off-diagonal terms,

and one can obtain an explicit expression for the factors in the expression (17) :

$$e^{(i/\hbar)\hat{H}_l t_p} = I + it_p \begin{pmatrix} 0 & \Omega^*/2 \\ \Omega/2 & 0 \end{pmatrix} + \frac{(it_p)^2}{2} \begin{pmatrix} |\Omega/2|^2 & 0 \\ 0 & |\Omega/2|^2 \end{pmatrix} + .. =$$

$$= \begin{pmatrix} \cos\theta/2 & iq^*\sin\theta/2 \\ iq\sin\theta/2 & \cos\theta/2 \end{pmatrix}, \qquad (19)$$

where $\theta = |\Omega t_p|$ - pulse area, $q = \frac{\Omega}{|\Omega|}$. Then the action of the pulse leads to the following changes of density matrix in the rotating frame:

$$\tilde{\rho}^a = \left(\begin{array}{c|c} \begin{array}{c} \tilde{\rho}^b_{11}\cos^2\theta/2 + \tilde{\rho}^b_{22}\sin^2\theta/2 - \\ -i\sin\theta/2\cos\theta/2(q^*\tilde{\rho}_{21} - q\tilde{\rho}_{12}) \end{array} & \begin{array}{c} \tilde{\rho}^b_{12}\cos^2\theta/2 + (q^*)^2\tilde{\rho}^b_{21}\sin^2\theta/2 - \\ -iq^*\sin\theta/2\cos\theta/2(\tilde{\rho}_{22} - \tilde{\rho}_{11}) \end{array} \\ \hline \begin{array}{c} \tilde{\rho}^b_{21}\cos^2\theta/2 + q^2\tilde{\rho}^b_{12}\sin^2\theta/2 - \\ -iq\sin\theta/2\cos\theta/2(\tilde{\rho}_{11} - \tilde{\rho}_{22}) \end{array} & \begin{array}{c} \tilde{\rho}^b_{11}\sin^2\theta/2 + \tilde{\rho}^b_{22}\cos^2\theta/2 - \\ -i\sin\theta/2\cos\theta/2(q\tilde{\rho}_{12} - q^*\tilde{\rho}_{21}) \end{array} \end{array} \right),$$

$$(20)$$

where the superscripts $\{b, a\}$ denote the elements of $\tilde{\rho}_{ij}$ before and after the excitation, respectively. The most illustrative change in the density matrix of the unperturbed system is under the action of pulse with area $\theta = \pi/2; \pi$:

$$\rho = \tilde{\rho} = \begin{pmatrix} 1 & 0 \\ 0 & 0 \end{pmatrix} \xrightarrow{\theta=\pi/2} \frac{1}{2}\begin{pmatrix} 1 & i \\ -i & 1 \end{pmatrix}; \; \tilde{\rho} = \begin{pmatrix} 1 & 0 \\ 0 & 0 \end{pmatrix} \xrightarrow{\theta=\pi} \begin{pmatrix} 0 & 0 \\ 0 & 1 \end{pmatrix}. \qquad (21)$$

A pulse with area $\theta = \pi/2$ transfers the TLS from the ground state to a coherent superposition with zero population inversion $\tilde{\rho}_{22} - \tilde{\rho}_{11}$, while the pulse $\theta = \pi$ completely inverts the TLS to the excited state.

2.1.3 Free precession

In the absence of perturbation, the Hamiltonian $\hat{H}_{eff}$ is diagonal, so according to (17) the evolution of $\tilde{\rho}(t)$ is given by

$$\tilde{\rho}(t) = \begin{pmatrix} \tilde{\rho}_{11} & \tilde{\rho}_{12}e^{i\Delta t} \\ \tilde{\rho}_{21}e^{-i\Delta t} & \tilde{\rho}_{22} \end{pmatrix}. \qquad (22)$$

The off-diagonal terms, which are responsible for the polarization, precess at the detuning frequency, while the diagonal terms responsible for the population remain constant.

We did not take into account the phase and energy relaxation so far, which real systems naturally possess. This is justified when considering the action of ultrashort laser pulses on the system with duration being much shorter than the characteristic relaxation times. However, when considering free precession, relaxation can not be neglected. The relaxation terms Γ are introduced into the optical Bloch equations phenomenologically, which corresponds to the transition from the von Neumann equation (68) to the Lindblad equation:

$$i\hbar\frac{\partial\rho}{\partial t} = [\hat{H}, \rho] + i\hbar\Gamma; \ \Gamma = \begin{pmatrix} \rho_{22}/T_1 & -\rho_{12}/T_2 \\ -\rho_{21}/T_2 & -\rho_{22}/T_1 \end{pmatrix}. \tag{23}$$

Here T_1 is the energy relaxation time, and T_2 is the irreversible phase relaxation (dephasing) time. Note that the irreversible phase relaxation rate $\Gamma_2 = 1/T_2$ is limited from below by the energy relaxation rate $\Gamma_1 = 1/T_1$.

$$\Gamma_2 = \Gamma_1/2 + \Gamma_C, \tag{24}$$

where Γ_C - the pure dephasing rate which is determined by elastic scattering processes. The presence of relaxation terms leads to exponential decay of the density matrix elements $\tilde{\rho}$ during free evolution:

$$\tilde{\rho}_{12}(t) = \tilde{\rho}_{12}e^{(i\Delta - 1/T_2)t}; \ \tilde{\rho}_{22}(t) = \tilde{\rho}_{22}e^{-t/T_1} \tag{25}$$

2.1.4   Photon echo protocol

Let us consider the two-pulse PE protocol for inhomogeneous TLS ensemble, shown in figure 12. Initially, the ensemble is in the ground state. Then the first laser pulse drives each TLS into a coherent superposition. After the action of the pulse, the systems in the ensemble experience reversible and irreversible phase relaxation, as well as energy relaxation. The second pulse is delayed by τ_{12} relative to the first pulse and rephase the ensemble. We will follow the macroscopic polarization P after the arrival of the second pulse. For clarity, we consider the first pulse with the area $\theta = \pi/2$, and the second one $\theta = \pi$. Note that the main result holds for arbitrary pulse areas. This protocol can be considered as subsequent action of the
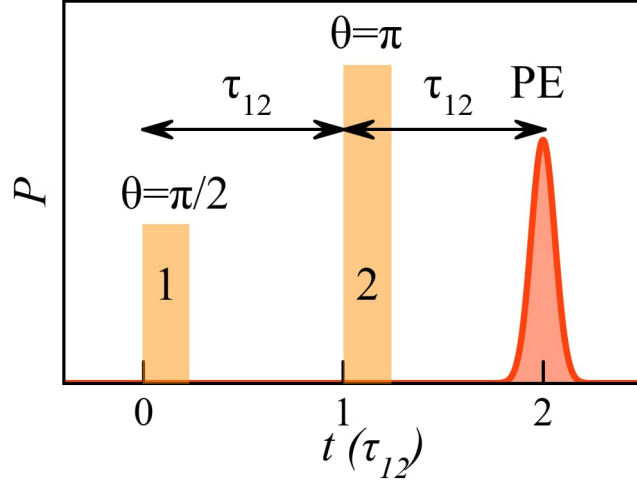
Figure 12: Schematic representation of macroscopic polarization in the form of a photon echo (PE in the figure) under excitation of the system by pulses 1 and 2 separated in time by delay τ_{12}. For simplicity, pulses are assumed to have a negligible duration with a finite pulse area.

Hamiltonian $\hat{H}_L$ and the unperturbed diagonal Hamiltonian $\hat{H}_{eff}$ on the $\tilde{\rho}(0)$:

$$\tilde{\rho}(0) = \begin{pmatrix} 1 & 0 \\ 0 & 0 \end{pmatrix} \xrightarrow{\theta=\pi/2} \frac{1}{2} \begin{pmatrix} 1 & i \\ -i & 1 \end{pmatrix} \xrightarrow{\tau_{12}} \frac{1}{2} \begin{pmatrix} 2 - e^{-\tau_{12}/T_1} & ie^{(i\Delta - 1/T_2)\tau_{12}} \\ -ie^{(-i\Delta - 1/T_2)\tau_{12}} & e^{-\tau_{12}/T_1} \end{pmatrix} \xrightarrow{\theta=\pi}$$

$$\xrightarrow{\theta=\pi} \frac{1}{2} \begin{pmatrix} e^{-\tau_{12}/T_1} & -ie^{(-i\Delta - 1/T_2)\tau_{12}} \\ ie^{(i\Delta - 1/T_2)\tau_{12}} & 2 - e^{-\tau_{12}/T_1} \end{pmatrix} \xrightarrow{t - \tau_{12}}$$

$$\xrightarrow{t - \tau_{12}} \frac{1}{2} \begin{pmatrix} 2 + e^{(-t/T_1)}(1 - 2e^{(\tau_{12}/T_1)}) & -ie^{i\Delta(t - 2\tau_{12}) - t/T_2} \\ ie^{-i\Delta(t - 2\tau_{12}) - t/T_2} & e^{(-t/T_1)}(2e^{(\tau_{12}/T_1)} - 1) \end{pmatrix} \quad (26)$$

We have defined the evolution of $\tilde{\rho}(t)$, hence the evolution of the original density matrix $\rho(t)$ can be calculated according to the rule (13). The polarization P_Δ induced by a single TLS is determined by the expectation value of the dipole moment $\langle \hat{d} \rangle = \mathrm{Tr}(\hat{d}\rho) \propto \mathrm{Re}(\tilde{\rho}_{12}e^{i\omega t})$ (see Appendix, equation (59)). After the arrival of the second pulse, P_Δ is

$$P_\Delta \propto \sin(\omega t + \Delta(t - 2\tau_{12}))e^{-t/T_2} \quad (27)$$

Note that at $t = 2\tau_{12}$, the contribution to the polarization phase associated with optical detuning is zeroed and all TLS in the ensemble become phased. The macroscopic polarization P is determined by integration over an inhomogeneous ensemble of TLS. Considering the Gaussian distribution of the transition frequency ω_0 (detuning Δ as well) with the central frequency $\bar{\omega}_0 = \omega$ and the variance $\sigma^2 = 8\ln(2)/T_2^*$, one can obtain

$$P \propto \int_{-\infty}^{+\infty} \sin(\omega t + \Delta(t - 2\tau_{12})) e^{-t/T_2} e^{-\Delta^2/2\sigma^2} d\Delta = P_0 \sin(\omega t) e^{-t/T_2} e^{\frac{-4\ln(2)(t-2\tau_{12})^2}{T_2^{*2}}}$$

(28)

Finally, the macroscopic polarization envelope, which is detected in the experiment, has the form of a Gaussian peak centered on $t = 2\tau_{12}$. The width of the peak is T_2^* and the amplitude decays exponentially with time T_2. The obtained result is in line with published calculations [18, 92].

There is a illustrative geometric interpretation of the TLS coherent dynamics using the Bloch vector $\vec{S} = (u, v, w)$, whose coordinates in the rotating reference frame are determined by the elements $\tilde{\rho}$

$$\begin{cases} u = \tilde{\rho}_{12} + \tilde{\rho}_{21} = 2\text{Re}(\tilde{\rho}_{12}) \\ v = i(\tilde{\rho}_{12} - \tilde{\rho}_{21}) = -2\text{Im}(\tilde{\rho}_{12}) \\ w = \tilde{\rho}_{22} - \tilde{\rho}_{11} = n_2 - n_1 \end{cases} .$$

(29)

The vertical projection of the vector $\vec{S}$ corresponds to the population inversion of the excited and ground state of the TLS, and the horizontal components correspond to the real and imaginary parts of the density matrix element $\tilde{\rho}_{12}$, which are responsible for the polarization. In case of TLS, one can adjust the phase in such a way that Ω becomes real [94]. Then the optical Bloch equations are reduced to the problem of rotation of the vector $\vec{S}$:

$$\dot{\vec{S}} = \vec{\Omega} \times \vec{S},$$

(30)

where the vector $\vec{\Omega} = (-\Omega, 0, -\Delta)$. Now we can depict the dynamics of the TLS ensemble in the PE protocol (26) as the dynamics of a set of vectors $\vec{S}$. For this purpose we use the previous result of the change in $\tilde{\rho}$ under the action of pulses and evolution of $\tilde{\rho}$ during a free precession between pulses, as depicted in the figure (13).

In this part the dynamics of the TLS ensemble in the two-pulse PE protocol under ultrashort excitation regime is analyzed. Performing analogous calculations for the three-pulse photon echo protocol, it can be shown that the amplitude of the stimulated three-pulse photon echo decays as $P \propto e^{-\tau_{23}/T_1}$, where τ_{23} is

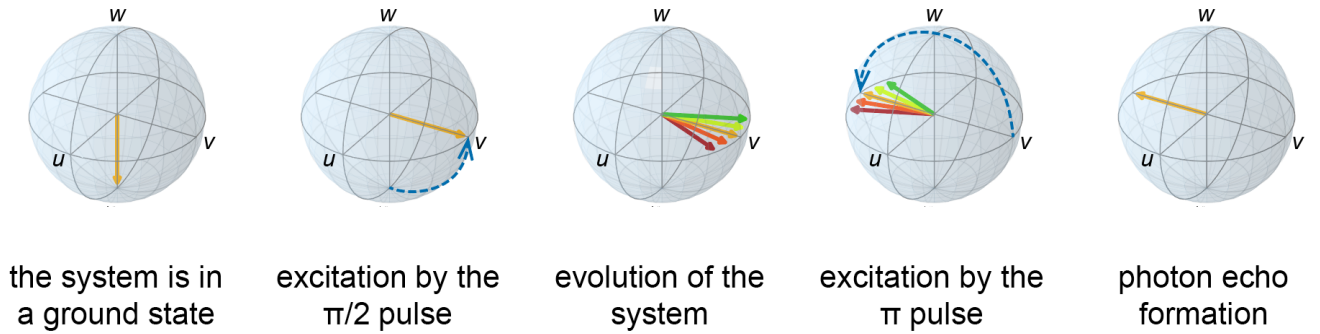| the system is in a ground state | excitation by the π/2 pulse | evolution of the system | excitation by the π pulse | photon echo formation |

Figure 13: Evolution of ensemble of Bloch vectors in PR protocol.

time delay between the second and third pulse. Despite of relative simplicity, this theory is in excellent agreement with experimental data even in its the basic version and describes correctly the PE signal from ensembles of excitons and their charged complexes in semiconductor nanostructures in the femto- and picosecond time ranges[138]. Using the described approach, one can develop the problem for particular cases [18, 32]. For example, if consider pulses of arbitrary areas, it can be shown that the PE signal will experience Rabi oscillations when scanning the pulse area of the first and second pulses [125]. Taking into account a finite pulse duration leads to shift and modification of the PE peak, and the introduction of additional relaxation mechanisms leads to a damping of the PE amplitude [115].

2.2 Exciton and trion fine structure and optical selection rules

The coherent dynamics of an ensemble of TLS systems was discussed in the previous section. In order to apply the theory in correct way and to describe the experimentally observed PE signal from excitons and trions, an extended model is required which takes into account the fine structure of excitons and trions, as well as selection rules for optical transitions between states.

The energy structure of exciton and trion levels, and corresponding selection rules are determined by the symmetry of valence and conduction bands. The subbands originating from atomic orbitals have a certain symmetry and are characterized by the corresponding orbital moment, as depicted in the figure 14(a). In the GaAs at the Γ point, the valence band has 3 p-like subbands with orbital quantum number $l = 1$, while conductivity band originates from s-like states with orbital momentum $l = 0$. Taking into account intrinsic moment - electron spin $S = 1/2$,

total angular momentum (also called spin) quantum number runs the values of $j = |l - s|..l + s$ and for each total angular momentum j there are $2j + 1$ projections $j_z = -j.. + j$. Thus, total angular momentum quantum number of electron in conduction band is $j = s = 1/2$ (since $l = 0$), while electron in valence subbands has $j = 1/2$ and $j = 3/2$. The spin-orbit interaction causes splitting of the valence subband with $j = 1/2$, which is therefore called the slit-off band, while the subbands with $j = 3/2$ and projections $j_z = \pm 3/2$ and $j_z = \pm 1/2$ are called heavy-hole (HH) and light-hole (LH) subbands respectively. These two subbands are degenerate in bulk material, but in QWs and QDs, the degeneracy is lifted due to translational symmetry breaking. A more detailed description of the fine structure is given, for example, in the monograph [139].
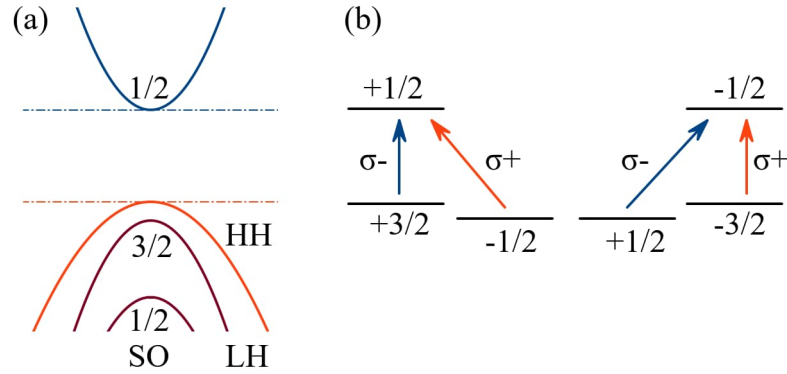

Figure 14: (a) Band structure of GaAs in the presence of HH-LH splitting. (b) Optically allowed interband transitions in GaAs.

In order to construct a QW-exciton model one should consider the allowed optical transitions between electronic states. Among other things, optical selection rules are determined by the angular momentum projection conservation law. We restrict ourselves to transitions from the HH subband to the conduction band. When a circularly polarized photon ($\sigma\pm$) with the projection $s_z = \pm 1$ is absorbed, transitions from the valence band states $j_z = \mp 3/2$ to the conduction band states $j_z = \mp 1/2$ take place. After such a transition a hole with the opposite projection $j_z = \pm 3/2$ is formed in the valence band, as shown in the figure 14(b). Let us consider the undoped structure. The ground state of the crystal corresponds to a completely filled valence band and an empty conduction band. When an exciton is formed from electron-hole pair with oppositely oriented spins, it has the $J_z = \pm 1$ projection and it is called bright exciton, since the optical transition from the ground state to such a state is allowed. If the spins of an electron and a hole in an exciton
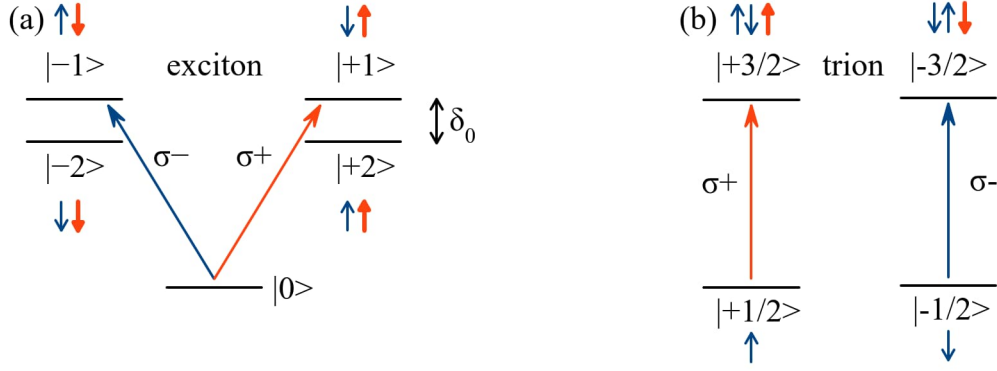
Figure 15: Energy level structure of exciton (a), negatively charged trion (b) and corresponding optical transitions.

are oriented in the same direction such excitons with the $J_z = \pm 2$ projection are called dark excitons, since direct optical transitions to such states are forbidden. As a result, for neutral excitons one can consider a V-type energy level structure with one common ground state and four excited states, as shown in Fig. 15(a).

The second case is a negatively doped structure with free electrons. The ground state corresponds to an unpaired electron in the conduction band. This is two-fold spin degenerate state $|\pm 1/2\rangle$, which is depicted in figure 15(b). An optical transition leads to creation of a negatively charged trion - two electrons in the conduction band with opposite spins (singlet state) and a hole in the valence band. A total trion spin $J_z = \pm 3/2$ equals to the hole spin. As a result, trion states can be described using a four-level model.

The chapters 3, 4 are devoted to the study of ZnO- and GaN-based quantum wells. These structures have a wurtzite type crystal structure. The conduction band is formed from s-type atomic orbitals, while the valence band originates from p-type orbitals, which splits into three subbands called A, B and C [140]. The order of subbands and their symmetry have long been a subject of discussion [41, 140–142]. However, the selection rules allow dipole transitions from subbands A and B to the conduction band under excitation by light whose electric field is perpendicular to the crystal growth axis $\vec{E} \perp \vec{(c)}$. These considerations allow us to model the exciton ensemble in ZnO and GaN using a V-type scheme, and consider trions as a four-level system, similarly to the case of GaAs.

Thus, the above approach can be developed to simulate the PE signal from ensembles of excitons and trions by increasing the number of states. These quasiparticles, described by four- and five-level models respectively, have different selection rules. Therefore, theoretical analysis predicts that the PE signal from excitons and

trions has different dependence on the polarization configuration of exciting pulses [122, 135].

2.3   Spin phenomena studied by photon echo

Consideration of protocols for spin-dependent PE gives rise to observation of fundamentally new effects [127, 128]. The application of a magnetic field perpendicular to the optical axis (Voigt geometry) causes the precession of the electron and hole spins at the Larmor frequency, which leads to mixing of states. The total spin Hamiltonian for an exciton is the sum of the terms corresponding to the Zeeman splitting of an electron H_e and a heavy hole H_h in a magnetic field, as well as the electron-hole exchange interaction H_{e-h} [143]:

$$H_e = \mu_B \sum_{i=x,y,z} g_{e,i} S_{e,i} B_i \tag{31}$$

$$H_h = -2\mu_B \sum_{i=x,y,z} (k_i J_{h,i} + q_i J_{h,i}^3) B_i \tag{32}$$

$$H_{e-h} = -\sum_{i=x,y,z} a_i S_{e,i} J_{h,i} + b_i S_{e,i} J_{h,i}^3 \tag{33}$$

Here S_i, J_i - spin projection operator of electron and hole, respectively, $g_{e,i}$ - electron g-factor components, k_i, q_i - hole Zeeman splitting constants, a_i, b_i - spin-spin interaction constants. Due to HH-LH subband splitting in QWs, one can consider the effective spin operator of the heavy hole $\widetilde{S}_h$ [143], and the total spin Hamiltonian will be given by:

$$\hat{H}_Z = \sum_{i=x,y,z} \mu_b (g_{e,i} S_{e,i} - g_{h,i} \widetilde{S}_{h,i}) B_i - c_i S_{e,i} \widetilde{S}_{h,i}, \tag{34}$$

$$g_{h,x} = 3q_x, g_{h,y} = -g_{h,x}, g_{h,z} = 6k_z + \frac{27}{2}q_z, c_x = \frac{3}{2}b_x, c_y = -\frac{3}{2}b_y, c_z = 3a_z + \frac{27}{4}b_z. \tag{35}$$

At $\vec{B} = (B_x, 0, 0)$ $\hat{H}_Z$ has the following form in the basis of exciton states {0,+1;-1;+2;-2}:

$$\hat{H}_Z = \frac{\hbar}{2} \begin{pmatrix} 0 & 0 & 0 & 0 & 0 \\ 0 & \delta_0/\hbar & \delta_1/\hbar & \omega_e & \omega_h \\ 0 & \delta_1/\hbar & \delta_0/\hbar & \omega_h & \omega_e \\ 0 & \omega_e & \omega_h & -\delta_0/\hbar & \delta_2/\hbar \\ 0 & \omega_h & \omega_e & \delta_2/\hbar & -\delta_0/\hbar \end{pmatrix} \tag{36}$$

$$\omega_{e,h} = \frac{g_{e,h}\mu_b B_x}{\hbar}, \ \delta_0 = c_z/2, \ \delta_1 = (c_x + c_y)/2, \ \delta_2 = (c_x - c_y)/2 \tag{37}$$

In the protocol of spin-dependent photon echo in a transverse magnetic field, these contributions to the total Hamiltonian are taken into account between the action of optical pulses during free precession, which leads to the appearance of oscillations in the PE signal. Such calculation was done for exciton model [136]. Protocols for two- and three-pulse spin-dependent PE from an ensemble of trions were considered as well, which results were experimentally confirmed [127–129, 131].

2.4   Time-resolved detection of picosecond photon echo

In order to study the ultrafast optical coherent dynamics of excitons and trions we used the degenerate FWM and PE technique with picosecond time resolution in the dissertation. The section 1.3 is devoted to the review of studies by this method, and the modeling of the PE protocol is provided in the section 2.1.4.

The objects under study in all subsequent chapters are semiconductor nanostructures with I-type QWs, which are optically active thin layers with pronounced exciton and trion resonances. A detailed description of the samples will be given in the following experimental chapters.

To conduct the experiments described in chapter 5, the author built an experimental setup for detection of a degenerate FWM at St. Petersburg State University (SPbSU) [144]. The arrange of the key components of the setup is shown in the figure 16. The setup was built by analogy with the original setup implemented at the Technical University of Dortmund, Germany (TU Dortmund) in the laboratory of prof. M. Bayer. The author obtained experimental results presented in chapters 3, 4 using that setup. These chapter also provide some differences in the setups used at that time.

Consider the scheme from figure 16. The setup was described in the author's
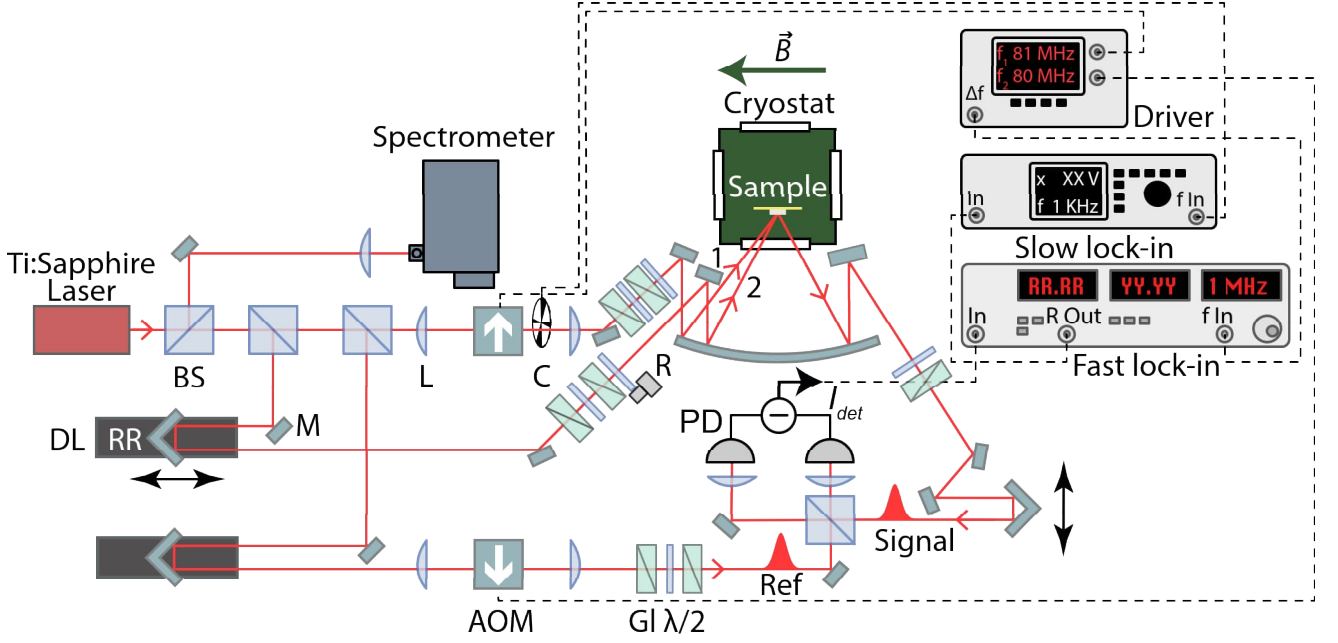
Figure 16: The experimental setup for time-resolved detection of FWM and PE by means of the optical heterodyne technique.

work [144]. All experiments were carried out at helium temperatures. Cooling the system down to a few degrees Kelvin makes it possible to avoid additional dephasing of excitons due to exciton-phonon scattering. To do this, the sample is placed in liquid helium inside the variable temperature inset (VTI) of a helium closed-cycle cryostat and cooled down to a temperature of $T = 1.5$ K by pumping out the VTI. Optical excitation of the sample is carried out using spectrally narrow laser pulses with a duration of about 3 ps, generated by a tunable Ti:sapphire laser with a pulse repetition rate of $f_{Laser} = 80.82$ MHz. The spectral width of the pulse is about 1 meV (figure 17(a)) which is comparable with the typical binding energy of the trion and biexciton. It provides us opportunitiy to study a selected ensemble of quasiparticles without exciting other ensembles which have closely spaced spectral lines.

The laser beam is passing through a set of beam-splitting cubes (BS) and is split into three separate optical paths, designated as the first (1), the second (2) and the reference (Ref). Additionally, a small portion of the laser light was split off to detect the laser spectrum using a spectrometer with a installed charge-coupled device linear detector. The manipulation of the time delay between pulses 1-2 τ_{12} and the delay of the reference pulse relative to the first τ_{Ref} was implemented by placing retroreflectors (RR) installed on motorized optical delay lines (DL). The time delay can be set in the range of 0-2000 ps in increments of 0.1 ps. Pulses 1

and 2 are directed by flat mirrors (M) to a spherical mirror with a focal length of $f = 70$ cm, after which the beams are directed to the sample with projections of wave vectors along the sample plane $\boldsymbol{k}_1$ and $\boldsymbol{k}_2$ and are focused into a spot with diameter about 200 µm. The wave vectors are close to the normal to the sample plane (about $3 - 4°$), and the difference angle between them is less than $1°$ (figure 16). The coherent response from the sample (Signal) consists of several components - the reflected 1st and 2nd pulses with wave vector projections $\boldsymbol{k}_1$ and $\boldsymbol{k}_2$ and the FWM response with the wave vector projection $\boldsymbol{k}_{FWM} = 2\boldsymbol{k}_2 - \boldsymbol{k}_1$. After collimation by the same spherical mirror, these components are directed parallel to each other to a retroreflector. The displacement of the latter allows to select which component of the signal component to be directed to a non-polarizing beam splitter, where the signal is mixed with a reference pulse. A pair of mixed beams outgoing from the two sides of the beam splitter is focused on the photodiodes of the balanced photoreceiver.

Interferometric optical heterodyning is utilized for detection of the signal, the basics of which are described in [40]. The essence of the technique lies in mixing a weak signal with a reference pulse, the carrier frequencies of which are detuned in the megahertz range. To do this, a pair of synchronized traveling wave acoustic-optical modulators (AOM) are installed into the channels 1st and Ref. The frequencies of AOMs are set independently in the range of 75-85 MHz by a driver. The optical frequencies of the 1st and Ref beams are shifted by $f_1 = -81$ MHz and $f_{Ref} = +80$ MHz, respectively, a result of the diffraction of the first beam to -1 order and the reference beam to +1 order. Therefore, the optical frequency of the FWM signal is shifted by $f_{FWM} = -f_1 = +81$ MHz. As a result of mixing the FWM signal with the reference pulse, the photocurrent on each of the receivers consists of a constant component proportional to the sum of the intensities of the signal and the reference pulse, and an interference component oscillating at the difference frequency $\Delta f = f_{FWM} - f_{Ref} = 1$ MHz. The use of a balanced detection scheme results in the subtraction of the constant components and the doubling of the desired interferometric signal I_{Det}:

$$I_{det} \propto \int_{T_{Det}} [e^{i\Delta f t} E_{FWM}(t) E_{Ref}^*(t - \tau_{Ref}) + c.c.] dt, \tag{38}$$

where T_{Det} is the period of integration by the photodetector, determined by the

frequency bandwidth, $E_{FWM}(t)$ is the envelope of the FWM signal, $E^*_{Ref}(t - \tau_{Ref})$ is the envelope of the reference pulse delayed by τ_{Ref} relative to the first pulse. Since $\Delta f \ll 1/T_{Det}$, the modulation factor can be considered as a slowly varying function on a given time scale and it can be moved outside the integral sign, so that the integral is a cross-correlation between the FWM signal and the reference pulse. Next, the signal is fed to the input of a high-frequency lock-in amplifier (Fast lock-in), the reference frequency of which is set by the AOM driver Δf. Since the setup does not posses complete interference stability, the quadrature components of the detected signal X, Y experience significant fluctuations. Therefore, the absolute amplitude $R = \sqrt{X^2 + Y^2}$ is taken from the output of the high-frequency lock-in amplifier. For further improvement of the detection sensitivity, the first beam was additionally chopped by a mechanical chopper at a frequency of 1 KHz. The second synchronous detection is performed by a low-frequency lock-in amplifier at the chopper frequency. As a result, when scanning the reference pulse delay τ_{Ref}, highly sensitive background-free detection of the cross-correlation modulus between the signal amplitude and the reference pulse is provided.
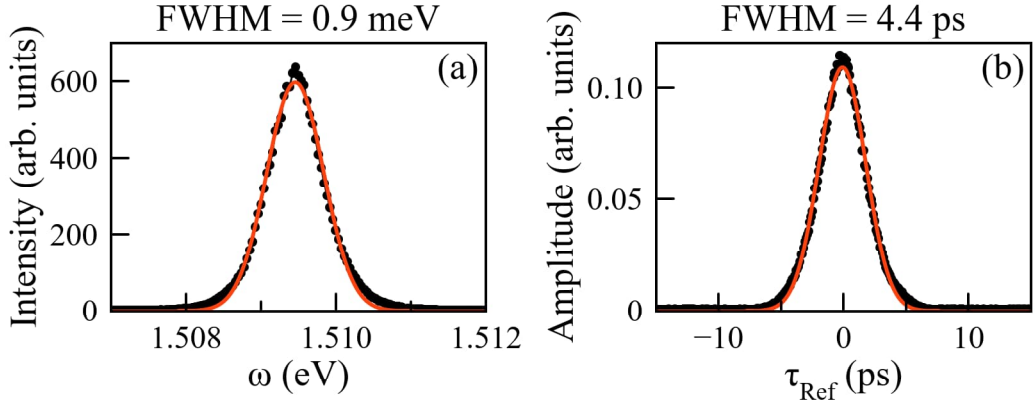

Figure 17: Spectrum (a) and auto-correlation function (b) of a laser pulse. Red solid lines correspond to fitting by Gaussian function.

Since reflected excitation pulses follow parallel to the FWM signal, the cross-correlation between each of them and the reference pulse can be measured by parallel shifting the retroreflector. The frequency of detection by high-frequency lock-in is equal to the side-bands $|f_{Ref} - f_1 - 2f_{Laser}|$ and $|f_{Ref} - f_{Laser}|$ for detecting the reflected first and second pulses, respectively. When excitation is out of resonance, the reflected signal will have only a non-resonant reflection component from the smooth surface of the sample, so the measured signal corresponds to the autocorrelation

function of the original pulses. Such measurements allow one to calibrate the time delays between excitation pulses and determine the duration of the pulses, as shown in the figure 17(b).
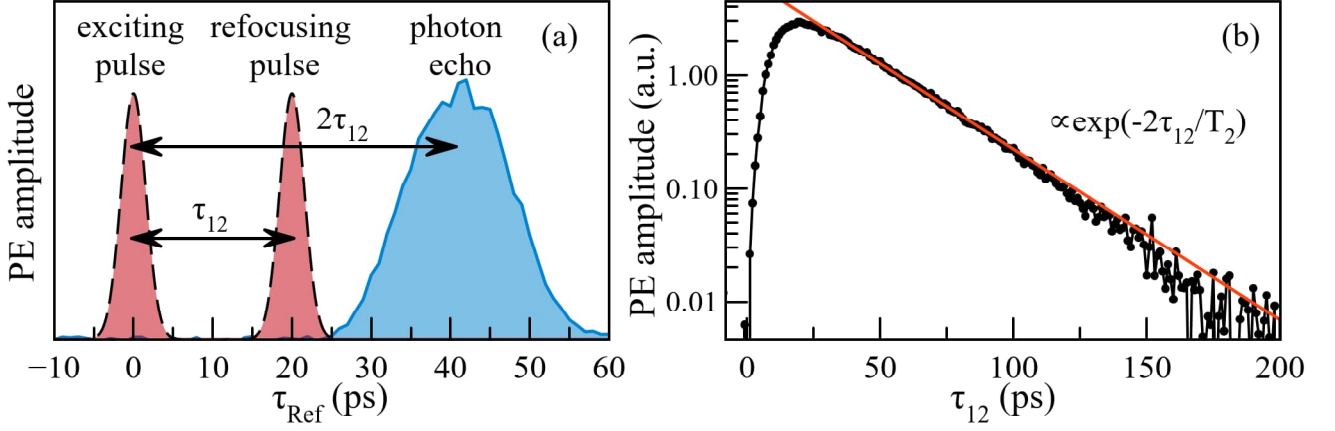

Figure 18: (a) Temporal profile of two-photon (primary) photon echo from exciton ensemble in 3-nm thick InGaAs QW. Exciting pulses are schematically illustrated. (b) kinetics of primary PE amplitude decay with increasing τ_{12}.

Figure 18(a) shows the temporal profile of the modulus of a two-pulse PE amplitude from an exciton ensemble. The shape of the signal is a Gauss profile and corresponds to the classical PE from an inhomogeneous ensemble. Since the duration of the PE is much longer than the duration of the reference pulse, we can neglect broadening caused by convolution and assume that the measured profile reflects the true temporal behavior of the PE. The key type of measurement of this work is shown in the figure 18(b). This is simultaneous scanning of the delays τ_{12} and τ_{Ref} and detection of the exponential decay of the amplitude of the photon echo peak $P_{PE} \propto e^{-2\tau_{12}/T_2}$, measured at $\tau_{Ref} = 2\tau_{12}$. Since the two-pulse PE arrives at the time $t = 2\tau_{12}$, the scanning step of the reference pulse delay τ_{Ref} is 2 times more than the scanning step of τ_{12}. The three-pulse echo signal occurs at time $t = 2\tau_{12} + \tau_{23}$, so the scanning step τ_{Ref} is the same as the step for τ_{23}. The experimental setup posses large number of degrees of freedom - pairs of crossed Glan prisms (Gl) with a half-wave plate ($\lambda/2$) between them allow for independent pulse power attenuation. The cryostat has superconducting magnets producing a magnetic field up to $B = 6$ T, which was used for spin-dependent PE measurements. The magnetic field vector is directed horizontally along the sample plane perpendicular to the direction of light (figure 16), which corresponds to Voigt geometry. Hereafter, we will denote the horizontal direction along the magnetic field vector by the index H and the vertical

direction perpendicular to it by V.

The experimental setup provides setting linear excitation and detection polarizations of arbitrary direction in the plane perpendicular to the wave vector (plane (H,V)) using a set of wave plates, some of which are mounted in motorized rotators (R). This makes it possible to measure the polarimetric dependences of the primary PE amplitude from excitons and trions in the geometry H$\varphi \to$H and H$\varphi \to$V, where H denotes the linear polarization horizontally oriented relative to the laboratory reference system, V - vertically oriented linear polarization, φ - linear polarization in the plane (H,V), which is rotated by the scanning angle φ relative to the horizontal direction. The first two indexes denote the polarization of the first and second pumping pulses, and the last index denotes the polarization which is detected. Such measurements make it possible to determine the structure of the energy levels of the sample under study, as was shown in the previous chapter. Also, measurements in several polarization configurations are necessary to obtain information on the g-factor of the exciton in the spin-dependent PE experiment.

All experiments were performed in automated mode. For this purpose, software was written that allowed to obtain the signal from the Lock-in, measure the properties of the exciting laser pulse - wavelength, spectral width; to set and scan power and polarization of exciting pulses, as well time delays τ_{12}, τ_{Ref}.

Chapter 3. Photon echo from excitons and trions in ZnO/(Zn,Mg)O quantum wells

The chapter is devoted to the experimental study of the coherent optical dynamics of excitons and trions in the structure with ZnO/(Zn,Mg)O. The chapter contains a brief introduction, a description of the sample, and the original experimental part. The analysis of the experimental data is followed by conclusion.

3.1   Introduction to chapter

Historically, gallium arsenide-based nanostructures were the first to be studied in the subject of coherent optical dynamics. However, they have a significant limitation: excitonic effects are observed only at helium temperatures due to the relatively low exciton binding energy of the order of units meV. Structures based on zinc oxide are more attractive from this point of view, since the exciton binding energy of about 60 meV allows us to observe excitonic effects up to room temperature [140]. Thanks to the development of growth technology of zinc oxide nanostructures it has been possible to create ultraviolet laser sources, including vertical-cavity surface-emitting lasers [145], LEDs [146], solar cells [147] other opto-electronic and spintronic devices as well [148]. Among the many ZnO-based structures of particular interest are quantum wells (QWs), whose parameters can be tuned depending on the task [149, 150]. The optical properties of the QWs are determined not only by neutral excitons (X), but also by excitonic complexes trions (T), which are observed in the presence of resident charge carriers. Magneto-optical techniques have been applied to the observation and study of trions in ZnO/(Zn,Mg)O QWs [41, 151] . Four-wave mixing and photon echo techniques have recently been successfully applied to study the picosecond coherent dynamics of donor-bound excitons in ZnO epitaxial layers at helium temperatures [101]. The homogeneous width and inhomogeneous broadening of the exciton transition in bulk ZnO were also determined [152] and the coherent properties of biexitons in ZnO/(Zn,Mg)O at room temperature were studied [153].

This chapter is devoted to the application of the FWM technique to study the coherent optical dynamics of excitons and trions in the ZnO/(Zn,Mg)O QW.These studies made it possible to advance the understanding of the energy structure of exciton states in such quantum wells, determine dephasing and energy relaxation

times for excitons and trions, and reveal how quasiparticle localization and phonon scattering affect on the exciton dephasing. Most of the results of the chapter were published in the co-author's paper [154] and were used in the author's aspirantura graduate qualification work at St. Petersburg State University.

3.2   The sample description

Figure 19: Structure of the sample ZMO1036 containing five ZnO/(ZnMg)O QWs.

The semiconductor heterostructure with five ZnO/(ZnMg)O QWs was used for the study, the scheme of which is shown in figure 19. The sample (ZMO1036) was grown on a sapphire substrate along the crystallographic C-axis by radial source molecular beam epitaxy. The sample consists of a 2 nm thick MgO nucleation layer, a half-micron (Zn,Mg)O buffer layer, five 3.5 nm thick ZnO QWs with 8.5 nm thick (Zn,Mg)O barriers, and a top layer of (Zn,Mg)O. To increase resident electrons density, δ-doping of QWs was applied by two Sb layers symmetrically located inside the barriers at a distance of 4 nm from the first and last QWs [155]. Since zinc oxide is intrinsically an n-type semiconductor, the presence of resident electrons leads to the appearance of [41] trion spectral lines. The application of δ-doping in the investigated structure led to an increase in the resident electrons density and to a more pronounced FWM signal from the trion ensemble. We estimate the doping level inside the QW barriers to be approximately 2×10^{12} cm^{-2}. The sample was grown on the substrate at 300 ° C. An additional annealing of the buffer layer for 5 minutes at 590 ° C was performed before the deposition of the QWs. The magnesium content in the buffer layer and in the barriers is $x = 0.09$, which leads to small built-in electric fields [150].
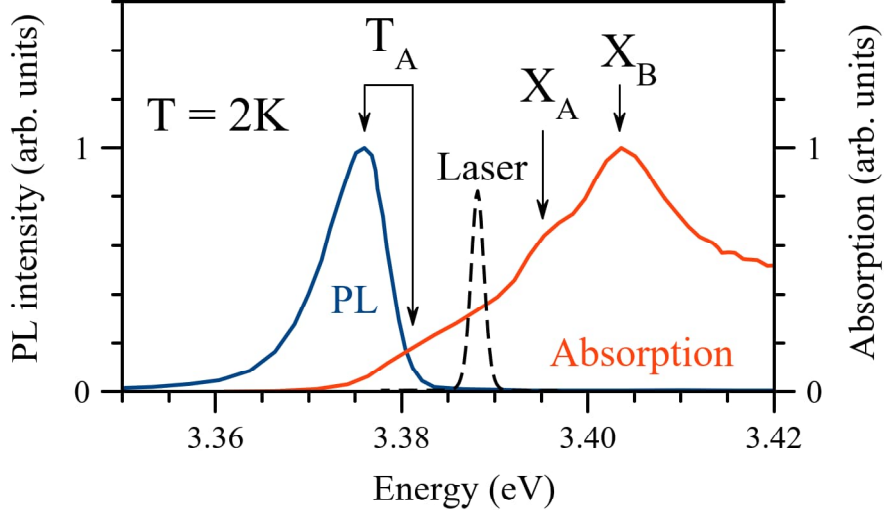
3.3   Sample characterization

Figure 20: Photoluminescence spectrum (blue) absorption spectrum (red) in the region of exciton and trion resonances measured at $T = 2$ K. Resonances are marked by vertical arrows. Dashed lines corresponds to typical spectrum of a laser pulse used for PE measurements.

The basic optical properties of the structure were studied by means of PL and absorption methods, these spectra are shown in figure 20. The measurements were carried out in the similar manner to the procedure described in [41], and the basics of the PL are given in the first chapter of the dissertation. In these spectra one can observe several features similar to those published in recent studies of ZnO/(Zn,Mg)O quantum wells using magneto-optical techniques [41, 42]. The peak at 3.375 eV in the PL spectrum corresponds to the recombination of the T_A trion. This transition manifests itself as a shoulder at 3.381 eV in the absorption spectrum. The Stokes shift of the order of 6 meV and the half-width of the PL peak of 9 meV indicate a significant inhomogeneous broadening of the T_A trion resonance due to localization. The absorption spectrum also contains two features not observed in the PL spectrum. They are located at 3.395 and 3.405 eV and correspond to A (X_A) and B (X_B) excitons.

3.4   Spectrally resolved photon echo

To study the coherent optical dynamics of excitons and trions, the PE technique with picosecond time resolution was applied. The experimental setup is similar to that given in the previous section 2.4. The main differences are as follows. Since
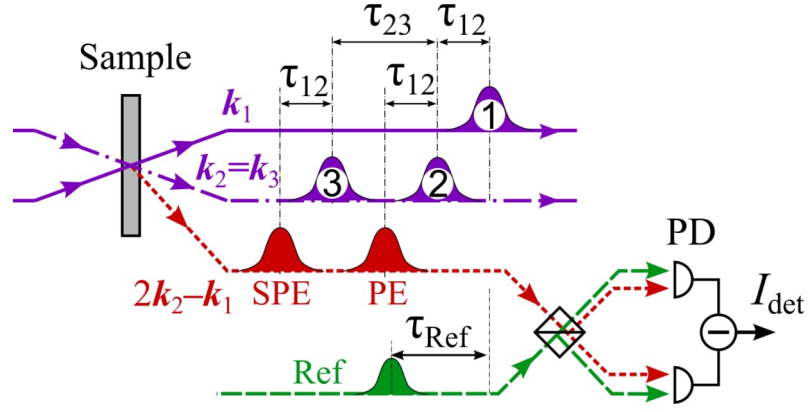
Figure 21: Schematic of optical excitation of the sample and FWM signal detection.

the energies of the excitonic and trion transitions are of the order of 3.4 eV, the second harmonic of the titanium-sapphire laser pulse with a repetition frequency $f_{Laser} = 75.75$ MHz was used for resonant excitation. The ultraviolet pulses outgoing from the frequency-doubling crystal have a duration of about 1.3 ps, whose spectrum is shown in figure 20. To measure the three-pulse stimulated (SPE), an additional delay line was introduced to control the time delay of the third exciting pulse relative to the first pulse τ_{13}. The third pulse was mixed with the second pulse and hit the sample with the same wave vector $k_3 = k_2$ as shown in figure 21. Since the substrate is transparent, the FWM signal was detected in the transmission geometry.
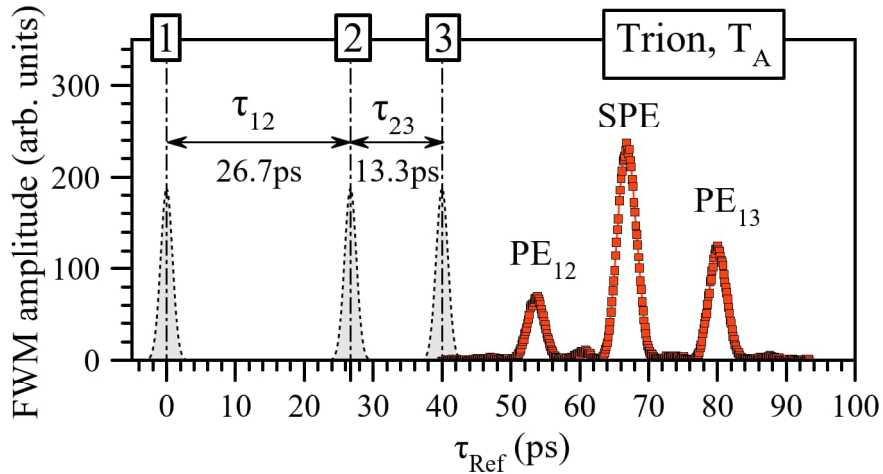

Figure 22: FWM temporal profile upon excitation of the system by a sequence of three pulses separated in time.

When a structure with multiple quantum wells (MQW) ZnO/(Zn,Mg)O is excited in the spectral range of X_A and T_A transitions, the FWM manifests itself as a photon echo. Figure 22 shows a typical temporal profile of the FWM when

the sample is excited by a sequence of three laser pulses with delays $\tau_{12} = 26.7$ ps and $\tau_{23} = 13.3$ ps with laser photon energy $E = 3.378$ eV. The signal consists of three separate PE peaks occurring at the expected time moments: PE_{12} at $\tau_{Ref} = 2\tau_{12} = 53.4$ ps and PE_{13} at $\tau_{Ref} = 2(\tau_{12} + \tau_{23}) = 80$ ps – two-pulse spontaneous PE produced by a sequence of pulses 1-2 and 1-3; SPE at $\tau_{Ref} = \tau_{23} + 2\tau_{12} = 66.7$ ps – three-pulse SPE produced by all three pulses.
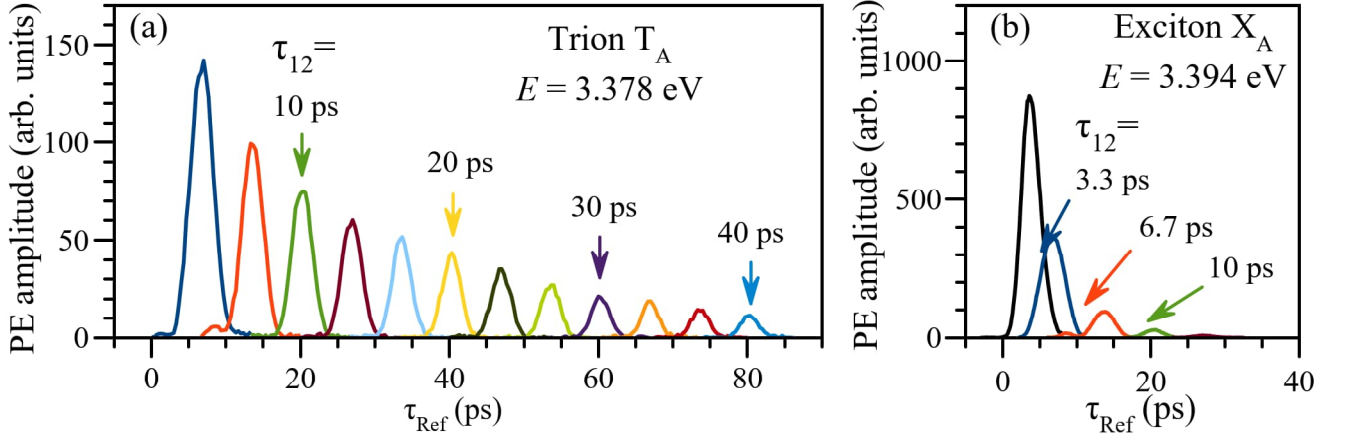

Figure 23: Temporal profiles of two-pulse PE from trions T_A (a) and excitons X_A (b) at different delays τ_{12}.

According to discussion in Chapter 2, increasing the delay τ_{12} in the two-pulse experiment leads to an exponential decay of the PE amplitude, from which we can derive the irreversible phase relaxation (dephasing) time T_2 of the state, which determines the homogeneous line width. Figure 23(a) and 23(b) show the decay of the PE profile from the ensembles of T_A trions measured at $E = 3.378$ eV and of excitons X_A measured at $E = 3.394$ eV, when a delay τ12 delay is scanning.
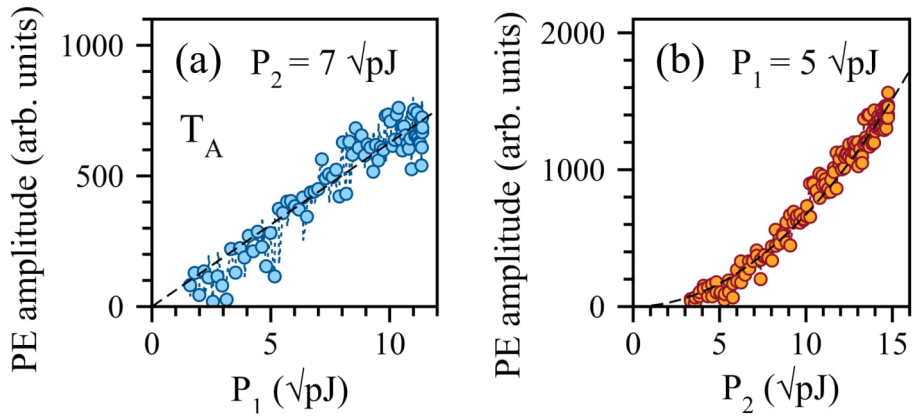

Figure 24: The amplitude of spontaneous PE from trions T_A as a function of amplitudes of the first and second pulses. Dashed lines correspond to linear (a) and parabolic (b) function.
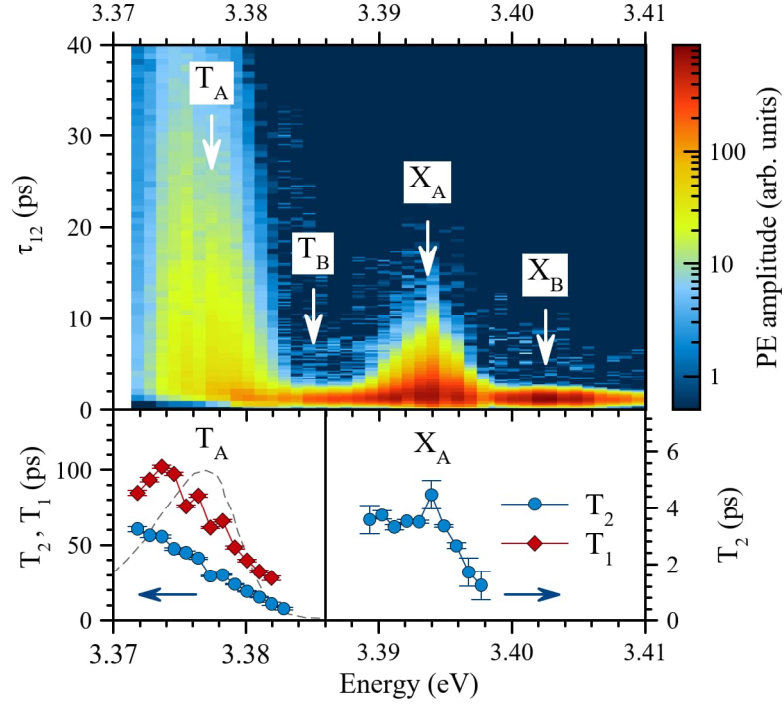
Figure 25: Color-map of the spontaneous PE amplitude as a function of energy E and delay τ_{12}. Bottom panel - spectral dependence of times T_2 and T_1. Additional PL spectrum is depicted by solid curve on the left bottom panel.

It has been verified that the exciting with the maximum available energy density of pulses (200 nJ/cm^2) does not lead to deviation from $\chi^{(3)}$ regime of measurements and it does not cause significant additional excitation induced dephasing. Figure 24(a) and 24(b) show the dependence of the PE amplitude from T_A trions at $\tau_{12} = 26.7$ ps as a function of the amplitudes (square root of the energy) of the first and second excitation pulses. The echo amplitude expectably grows linearly (figure 24(a)) and parabolically (figure 24(b)), which corresponds to the $\chi^{(3)}$ regime .

Spontaneous PE and stimulated PE kinetics were measured with spectral resolution in the region of excitonic and trion optical transitions. A review of similar studies on GaAs-based nanostructures is given in Chapter 1 [104]. During the measurements, the central wavelength of the tunable laser was fixed while delays τ_{12} and τ_{23} were scanning. In contrast to the [114] femtosecond technique, the use of picosecond laser pulses and ability to precisely tune laser wavelength make it possible to study the coherent dynamics of quasiparticles by selective excitation of the ensemble of interest.

A panoramic picture of the spectral dependence of the PE decay kinetics, measured in the spectral region of the optical transitions X_A, X_B and T_A, T_B in

steps of about 1 meV, is shown in figure 25. These data clearly show the difference in the dynamics of the two types of quasiparticles. Note that the dynamics of X_A and T_A has a long-lived character in contrast to the X_B and T_B. The latter possess significantly stronger but short-lived signal (look at log-scale by color). The coherence of excitons X_B and trions T_B decays on the sub-picosecond timescale, so the temporal profile is limited by the duration of the laser pulses. The kinetics of spontaneous PE from the T_A trions are shown in figure 26(a). One can observe a nearly mono-exponential decay character at $\tau_{12} > 10$ ps. In the decay curves of the spectral region above 3.376 eV one can notice a spike in the signal at the first few picoseconds, associated with the contribution from the T_B trions. By approximating the kinetics by exponential decay in different parts of the spectrum, we can obtain T_2 value of T_A trions and X_A excitons. These values are shown in the bottom panel of the figure 25. For both ensembles, an increase of the optical coherence time is observed as the transition energy decreases. The maximum observed T_2 time of T_A trions reaches 60 ps. For X_A excitons, the maximum value of T_2 is 4.5 ps, which is significantly longer than the T_2 of free excitons in the ZnO epitaxial layer exhibiting subpicosecond-scale dephasing [101]. One reason for such a short exciton coherence time may be the efficient formation of trions from excitons due to the relatively large density of resident electrons. This fact also manifests itself as weak PL signal from excitons X_A, which is not observable in a linear scale in the figure 20. It is worth noting the strong difference in behavior between the trions and excitons of the two types A and B. We believe that this difference in the properties of coherent dynamics is due to fast energy relaxation from the high-energy states of the B subband to the low-energy states of the A subband.

The population dynamics of the excited state was investigated by the three-pulse stimulated photon echo method. For this purpose, we fix the delay $\tau_{12} = 13.3$ ps and scan the delay τ_{23} by detecting the signal amplitude at delay $\tau_{Ref} = 2\tau_{12} + \tau_{23}$. The kinetics of the spectrally resolved population decay of the T_A trions is shown in figure 26 (b). We can not say that these curves have a true monoexponential decay, but it is possible to distinguish a fast component at the beginning and a long-lived tail. By approximating the rapidly decaying part by an exponential decay $P_{PE} \propto e^{-\tau_{23}/T_1}$, we obtained the spectral dependence of the value of T_1 for the trion transition T_A, shown in the bottom left panel of the figure 25. One can see that the time T_1 increases with decreasing trion energy and reaches
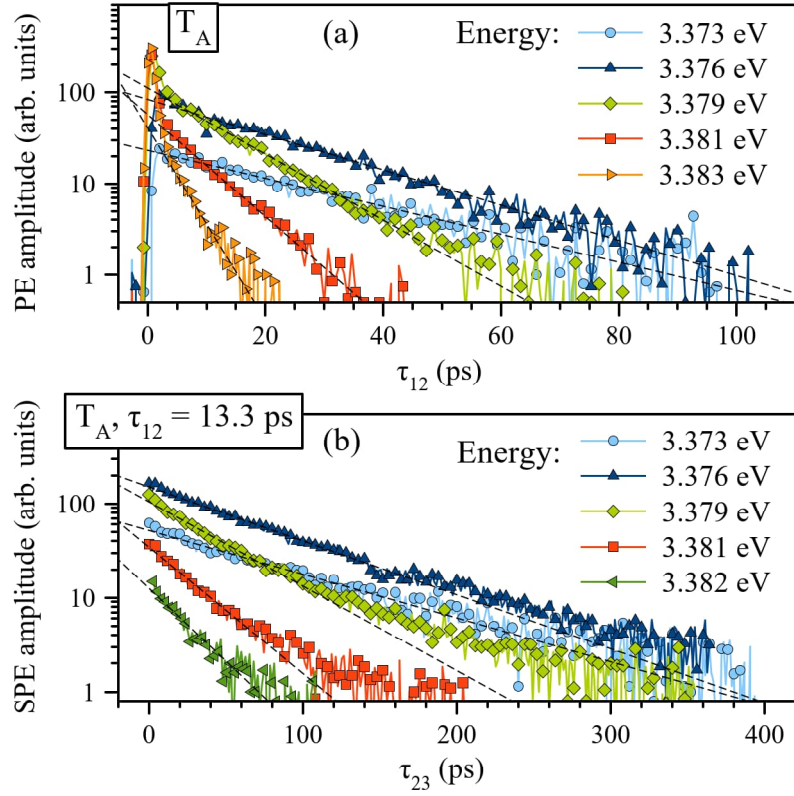
Figure 26: Kinetics of spontaneous PE decay (a) and SPE decay (b) measured with spectral resolution in the region of the T_A trion transition.

a value of 102 ps. The ratio $T_2 \approx 0.5 \cdot T_1$ indicates the presence of additional dephasing mechanisms in addition to the energy relaxation of the ensemble. From the approximation of the long-lived component, we obtained energy relaxation time values in the range up to 250 ps, which is in agreement with the T_A lifetime of 200 ps obtained earlier in a similar structure with ZnO/(Zn,Mg)O MQW using the time-resolved PL measurement [42].

3.5   Temperature-dependent study of coherent dynamics

Temperature measurements of FWM are extensively used to study the phonon-assisted dephasing and energy relaxation of excitons and exitonic complexes [100, 101, 105, 156–159]. We detected the kinetics of spontaneous PE and SPE decay from trions with energy $E = 3.376$ eV as a function of sample temperature in the range $T = 1.4 : 15$ K. The kinetics are shown in figure 27(a) and (b), and the extracted values of irreversible dephasing rate $\Gamma_2 = \hbar/T_2$, energy relaxation rate $\Gamma_1 = \hbar/T_1$ and pure dephasing rate $\Gamma_c = \Gamma_2 - \Gamma_1/2$ are shown in figure 27(c).

Firstly, one can see that the population dynamics is weakly dependent on tem-
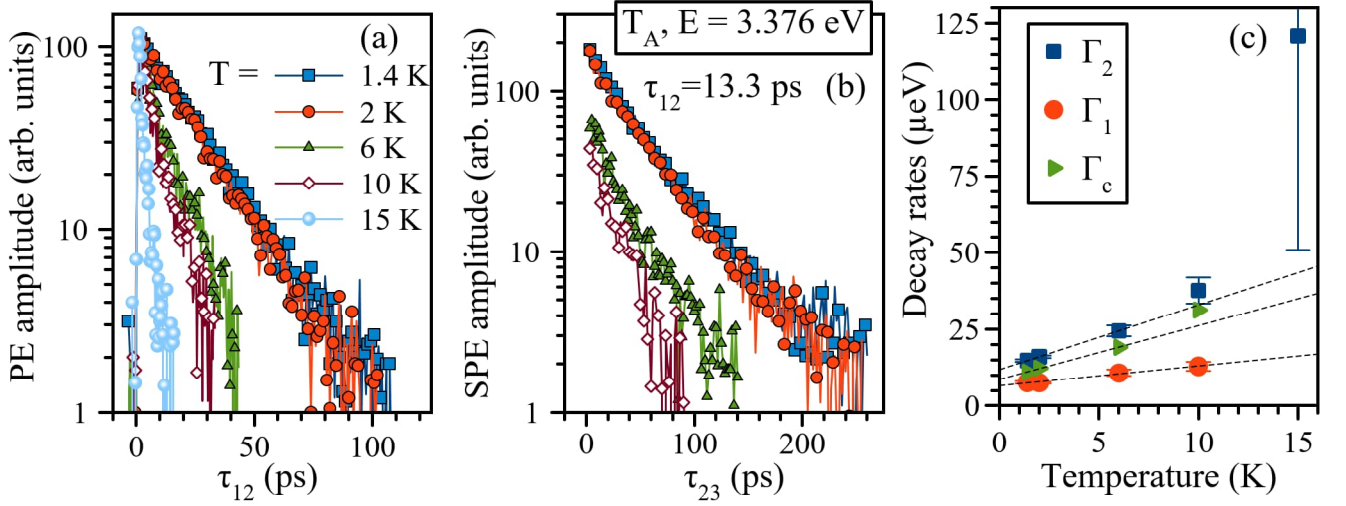
Figure 27: PE (a) and SPE (b) decays from trions measured at spectral region 3.376 ev as a function of temperature. (c) Temperature dependence of dephasing rate Γ_2 (squares), energy relaxation rate Γ_1 (circles), and pure dephasing rate Γ_c (triangles). Linear approximation is plotted by dashed lines.

perature up to $T = 10$ K, while a monotonic decrease in the SPE amplitude with increasing temperature is noticeable. Some increase in the population relaxation rate with increasing temperature may be a sign of trion delocalisation accompanied by absorption of acoustic phonons, as previously observed in GaAs/AlGaAs quantum wells [156, 157] and CdTe/CdMgTe [105, 158]. It is worth noting that these works considered a nonlinear increase in the total dephasing rate Γ_2, rather than a separate component of $\Gamma_1/2$, corresponding to the energy relaxation. However, the delocalization process leads to a change in the population of localized states, so we can draw an analogy between our data and the published results.

From the available experimental data it is difficult to distinguish between the linear and non-linear regime of Γ_2 due to the inaccuracy of the extracting of decay rate from fitting and of the sample temperature in the region $T > 4.2$ K, since at such temperatures the sample is not immersed in liquid helium, but in helium vapour leading to a weak thermal contact. It also limits the accuracy of pure dephasing data Γ_c. One can distinguish a linear growth with coefficient $\gamma \approx 2$ μeV/K related to trion scattering on acoustic phonons and a residual dephasing $\Gamma_d \approx 9$ μeV, which is independent of temperature, so that $\Gamma_c = \Gamma_d + \gamma T$. The linear dependence of the dephasing rate is more typical for free exciton complexes than for strongly localized states [105]. The calculated coefficient γ was found to be close to the recently determined value for donor-bound excitons D_0X_A in the ZnO epitaxial layer [101]

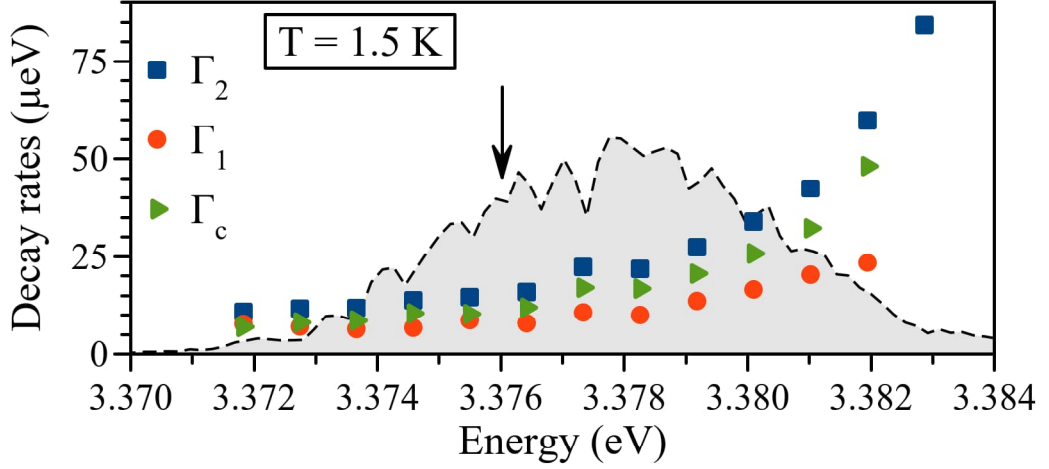(about 2 μeV/K). However, in the latter case a temperature-independent dephasing Γ_d was not observed.

Figure 28: Spectral dependence of Γ_2, Γ_1 and Γ_c, extracted from the data presented in figure 25. Gray curve corresponds to spontaneous PE spectrum, measured at $\tau = 6.67$ ps. Arrow indicates spectral point where temperature measurements were done.

In order to determine the origin for the additional trion dephasing, the spectral dependencies of Γ_1, Γ_2 and Γ_c were extracted from the data presented in figure 25. The results are presented in figure 28. One can see that all rates Γ_1, Γ_c and total Γ_2 increase strongly with increasing trion energy, i.e. the effects of dephasing and energy relaxation depend significantly on trion localization. At $T = 1.5$ K the contribution of elastic scattering on acoustic phonons can be neglected ($\gamma T \approx 3$ μeV). Therefore we can say that in this case the main contribution to the pure dephasing rate is governed by the temperature-independent contribution Γ_d.

3.6   An analysis of the experimental results

The observed monotonic increase of Γ_1 and Γ_2 rates of A trions and A excitons with increasing energy as well as the presence of a Stokes shift between the PL and absorption spectra can be explained by the localization of these quasiparticles on the fluctuations of the quantum well potential. Such fluctuations arise, for example, due to variations in the thickness of the well width, the content of the barriers and presence of built-in electric fields resulting from the inhomogeneous distribution of donors in the doping layer. The different degree of localization of particles within the inhomogeneously broadened ensemble can lead to a spread of the oscillator strength,

which defines population relaxation rate Γ_1. Due to the fact that the exciton and trion binding energies are larger than the characteristic value of the localisation energy, the latter mostly affects the wave function of the center of mass rather than the relative motion of electrons and holes in the exciton or trion [104]. The problem of trion localization have been considered so far in the quantum wires only [160]. In the case of localized excitons in the QW a relatively weak decrease of the oscillator strength has been found [161], which cannot cause such a dramatic change of time T_1 shown in figure 28. Therefore, we conclude that this change is caused by the non-radiative relaxation of trions inside the random potential landscape accompanied by phonon emission.

The strong increase of the dephasing rate Γ_d with increasing energy of trions T_A can also be explained by localization of the trions. High-energy trions are weakly localized or even non-localized. Such trions may experience elastic scattering at rough interfaces of the quantum well. In such scattering process the energy of the trion is retained, but phase is lost.

Additionally, the effect of spectral diffusion of trions within an inhomogeneous ensemble on phase and energy relaxation has been estimated. The results of these measurements [154] show that the contribution of spectral diffusion to the trion energy relaxation rate, measured in the center of the spectral line, Γ_{SD} is about 5 μeV, which is consistent in order of magnitude with the Γ_1 change within the spectral region shown in figure 28. However, a contribution of this effect does to the total trion dephasing rate $\Gamma_{SD}/2 \approx 2.5$ meV is not substantial in this case.

A similar effect of exciton and trion localization on coherent dynamics has been observed previously in heterostructures of different composition [104, 157, 162]. Although a recent study of the coherent dynamics of exciton complexes in a single CdTe/CdMgTe quantum well has shown an opposite decrease in coherence time as the energy of excitons localized on the neutral donor D_0X [115] decreases. It is worth noting that such effects depend significantly on the growth technology and the design of the heterostructure. By optimizing the growth parameters the QW excitons can be localized, weakly localized or completely delocalized, and the contributions of different dephasing mechanisms can take place so that a detailed analysis is required in each individual case.

3.7 Conclusion

We have investigated the picosecond coherent dynamics of excitons and trions in ZnO/(Zn,Mg)O MQW by means of the technique of two- and three-pulse photon echo using spectrally narrow laser pulses. The difference in the coherent dynamics of A and B excitons and trions was shown experimentally. The subpicosecond dynamics of type B quasiparticles is determined by fast relaxation to A states. We have successfully demonstrated a strong decrease of pure dephasing rate and energy relaxation rate with an increasing of the degree of trion localization T_A at low temperature. The reasons for this are a smaller influence of elastic scattering at roughness of the QW interface and non-radiative relaxation, as well as spectral diffusion inside the inhomogeneous trion ensemble, respectively. In addition, manybody interactions are less pronounced for strongly localized particles, however we have not observed significant effect of excitation-induced dephasing in the available excitation power range.

Chapter 4. Long-lived photon echo from exciton in (In,Ga)N/GaN multiple quantum well

The chapter is devoted to the study of the coherent optical dynamics of excitons in an (In,Ga)N/GaN 100 multiple quantum wells by two-pulse and three-pulse photon echo in the ultraviolet spectral range. The chapter contains a brief introduction, a description of the sample under study, the results of original studies of PL and PE spectroscopy in the region of exciton transition and measurements of PE decay kinetics at different temperatures. At the end of the chapter an analysis of the results is given, indicating a strong localization of excitons on the structure fluctuations, similar to the localization of particles in quantum dots. Main results were published in the author's paper [163].

4.1   Introduction to chapter

The optical properties of gallium nitride-based nanostructures are similar to the aforementioned zinc oxide-based systems. Thanks to the large value of exciton binding energy, (In,Ga)N/GaN QWs are widely used in optoelectronics, for example, as a platform for ultraviolet light-emitting diodes and lasers [164]. However, the growth quality of the structures, as in the case of zinc oxide, is still imperfect so far, and the structures possess composition disorder along the well plane, which naturally affects the optical and transport properties of the optical excited states [164–167]. The main reason of the disorder is the thermodynamic tendency to separate the InN-GaN phases during the structure growth [167]. The nature of the disorder depends significantly on the growth conditions [168, 169], and procedures such as increasing the growth temperature [168], hydrogen admixture [170], usage of structure annealing [171] or growth interruption [172] can be used to control the phase separation process. The presence of fluctuations leads to spatial localization of excitons in deformation potential [165, 166], which, firstly, leads to an inhomogeneous broadening of the exciton resonance, and, secondly, to a decrease of exciton oscillator strength due to inhomogeneous local electric fields. In addition, localized states are less influenced by inelastic scattering and non-radiative relaxation on such structural defects as dislocations. Taking into account these peculiarities, localized excitons in (In,Ga)N/GaN QWs can are expected to have a long dephasing time.

For a detailed analysis of the effect of composition fluctuations on the coherent

properties of excitons in (In,Ga)N/GaN QWs, the two- and three-pulse PE technique is extremely useful, providing a rich set of information about dephasing, energy relaxation, and determination of the homogeneous width hidden due to significant inhomogeneous broadening. To date, only a few work have been published in which FWM was used to study the coherent properties of excitons in bulk GaN [173, 174] epitaxial layers [175, 176] and GaN-based QWs [117, 177]. These studies show fairly short exciton times T_2 in the subpicosecond range. However, all the mentioned works used the femtosecond technique, which is characterized by a significant impact of many-body processes on the dephasing rate. This chapter of the dissertation is devoted to the study of coherent dynamics using picosecond technique, the main results of which are presented in the paper of the candidate [163].

4.2 The sample under study

Metalorganic chemical vapour deposition was used to grow the investigated structure. A substrate consists of sapphire with a 2 μm thick grown GaN layer. A subsequent 700 nm thick GaN buffer layer was grown at 1030 °C and a pressure of $2 \cdot 10^4$ Pa. Next, an array of 100 2.5 nm thick (In,Ga)N/GaN QWs was grown. The sample has a composition and thickness gradient of the structure layers because substrate rotation was not performed during the growth.

X-ray diffraction analysis of the structure provided estimates for the average indium concentration in the well of about 7.5 % and the barrier thickness of 69.5 nm [178] . For such a periodic structure, the Bragg reflection condition can be satisfied, which appears as a peak in the reflection spectrum [169]. At helium temperatures, this peak is located in the energy region of 3.393 eV (365.4 nm) and has a width of about 32 meV (3.5 nm). In this chapter, excitons with a lower transition energy are studied, so we do not expect significant effects associated with the crossing of exciton and Bragg resonances.

4.3 Sample characterization

To determine the basic optical properties of excitons in MQWs, we carried out time-resolved PL spectroscopy with a streak camera in transmission geometry at $T = 1.5$ K. Optical excitation was performed by a picosecond laser pulse with an energy of 3.44 eV (360 nm). The data measured with a time resolution of about
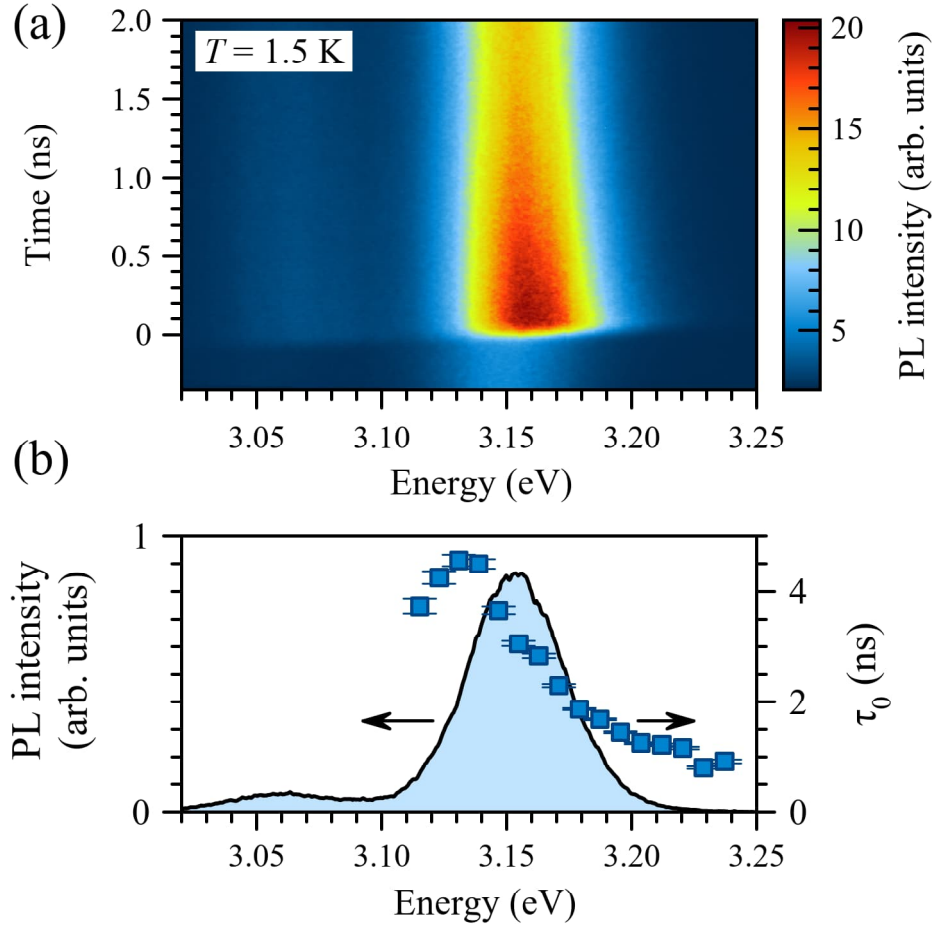
20 ps are shown in figure 29(a).

Figure 29: (a) Time-resolved PL spectrum. (b) Spectral dependence of extracted exciton lifetime τ_0 (squares) superimposed on the time-integrated PL spectrum (line).

The measurements show emission from a wide spectral region with a decay time distribution that varies significantly within the emission region. The time-integrated PL spectrum, which is shown in figure. 29(b), comprises of two Gaussian peaks with a large inhomogeneous broadening. The main peak located at an energy of 3.154 eV has a full width at half height (FWHM) of 46 meV corresponding to exciton emission, and an additional peak at FWHM 62 meV is a phonon replica shifted from the exciton peak to an optical phonon energy of 89.5 meV [179]. The PL kinetics were approximated using exponential decay for a set of energies. Spectal dependence of exciton lifetime τ_0 is presented in figure 29(b). The results show an almost monotonic increase of τ_0 from 0.8 to 4.5 ns with decreasing exciton transition energy.
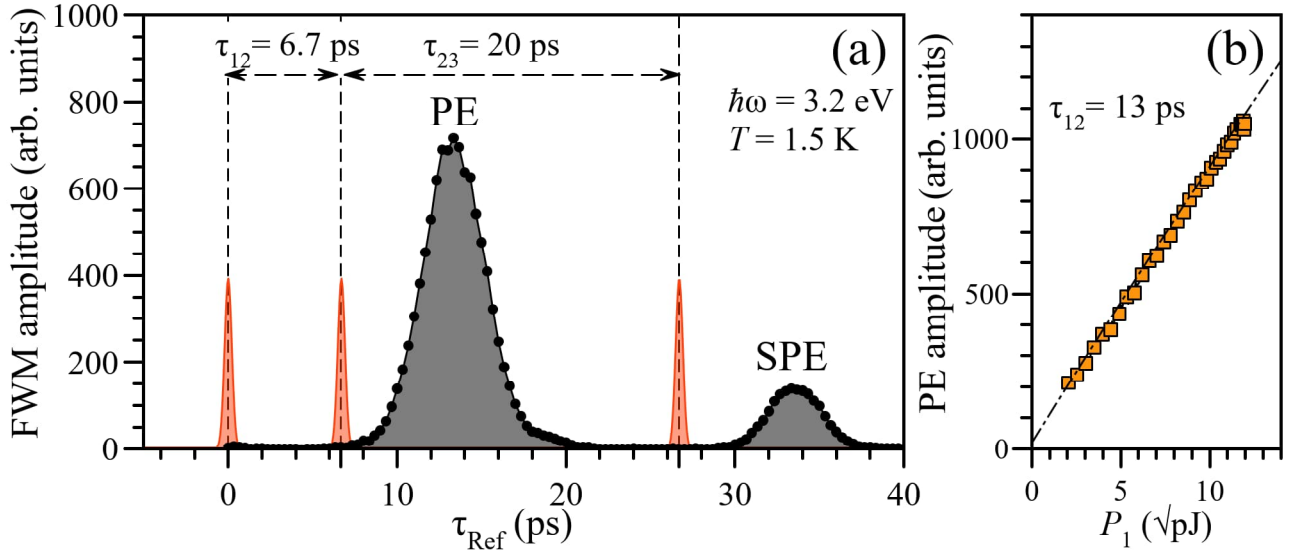
Figure 30: (a) FWM temporal profile (black), consisting of PE and SPE peaks. Red peaks indicate arrival time of exciting pulses. (b) PE Amplitude as a function of amplitude of the first pulse P_1 with superimposed linear fit.

4.4 Spectrally resolved photon echo

The coherent dynamics of excitons in (In,Ga)N/GaN MQW was studied using the two- and three-pulse PE technique (see figure 21). The FWM experimental setup was used in a configuration similar to that presented in the 3.4 section. Excitation by a sequence of three pulses with $\tau_{12} = 6.7$ ps and $\tau_{23} = 20$ ps with a photon energy $\hbar\omega = 3.20$ eV leads to the appearance of a FWM transient signal, which temporal profile is shown in figure 30(a). It consists of two Gaussian-shaped peaks: the first is located at $2\tau_{12} = 13.3$ ps and corresponds to the spontaneous PE, and the second occurs at the time $2\tau_{12} + \tau_{23} = 33.3$ ps and corresponds to SPE. The FWHM of the PE peak is 4.3 ps, which is determined by the convolution of the true PE profile with a reference pulse of duration of about 2.0–2.4 ps (1.5–1.8 meV). An increase of the first pulse amplitude P_1, defined as the square root of the pulse energy, to the maximum available, corresponding to an energy density of 200 nJ/cm^2, does not lead to a deviation from the linear growth of the PE amplitude, as shown in figure 30(b). In this case, the intensities of the second and third pulses were at least two times lower during the measurements. Therefore, we can assume that the measurements correspond to the $\chi^{(3)}$ regime.

The use of the spectrally narrow picosecond technique made it possible to selectively excite excitons with different localization energies and to measure the PE
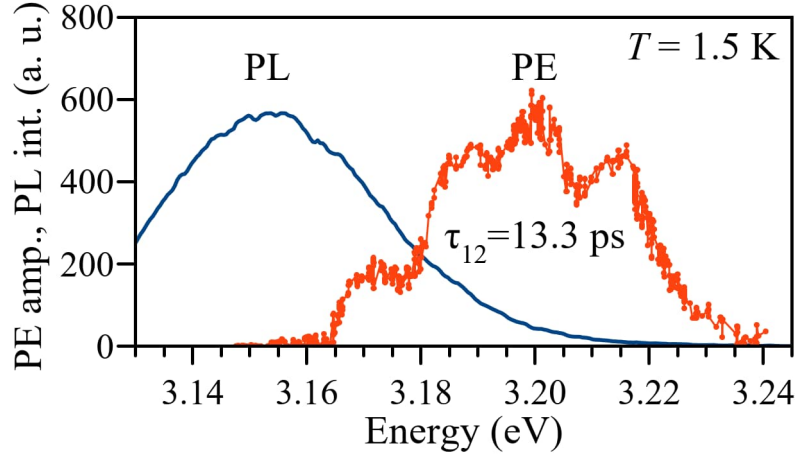
Figure 31: PL (blue) and spontaneous PE spectra (red) in the range of exciton resonance.

with spectral resolution. Figure 31 shows the dependence of the spontaneous PE amplitude from inhomogeneous exciton ensemble in the (In,Ga)N/GaN MQW at $T = 1.5$ K as a function of the central laser energy with superimposed PL spectrum from figure 29(b). The time delay was fixed to $\tau_{12} = 13.3$ ps. The figure demonstrates the observation of the spontaneous PE signal in an extraordinary wide spectral range of photon energy $E = 3.16 - 3.24$ eV (382–392 nm). The spectrum has periodic modulation, which we attribute to Fabry-Perot cavity interference between light reflected from the sample surface and from the GaN/sapphire substrate interface [178]. With this modulation taken into account, the spectrum of the primary PE can be approximated by a Gaussian contour with FWHM 43 meV (≈ 5 nm). Such a large inhomogeneous broadening compared to the spectral width of the laser pulse ≈ 1.7 eV, as well as a short duration of the PE, confirm that the PE response is formed by a subensemble within the laser pulse spectral region. At the same time, a comparison of the absorption and PL spectra for similar samples at room temperature gave a shift of the order of 20 meV [178].

Measurement of the spontaneous PE amplitude as a function of delay τ_{12} at a fixed photon energy makes it possible to obtain the signal decay kinetics. Figure 32(a) shows a color-map of the spectral dependence of the spontaneous PE decay kinetics in the region of the exciton transition, and a set of kinetics for several photon energies is shown in figure 32(b). The measurements show almost monoexponential decay in the presented spectral range, which is expected for our model. Approximation of the kinetics using the exponential decay $\propto \exp(-2\tau_{12}/T_2)$ gives the value of the dephasing time T_2 and the corresponding dephasing rate $\Gamma_2 = \hbar/T_2$.
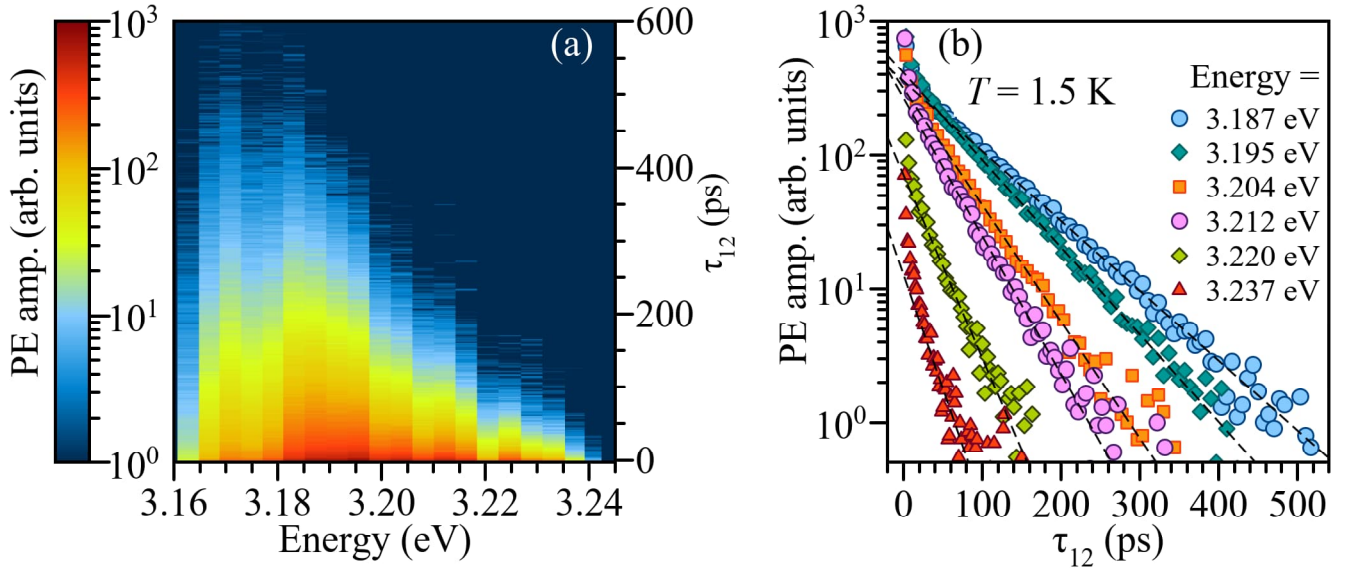
Figure 32: (a) Color-map of the spontaneous PE amplitude as a function of both time delay τ_{12} and photon energy with a step of 4 meV. (b) Set of decay kinetics of spontaneous PE amplitude (dots) at different photon energy with approximation by exponential curves (dashed).

The spectral dependence of these quantities is shown in figure 33. The figure shows a monotonic increase of time T_2 from 45 to 255 ps within a wide region of the exciton transition, which corresponds to an increase of the decay rate Γ_2 from 2.6 to 15 μeV as the photon energy increases.

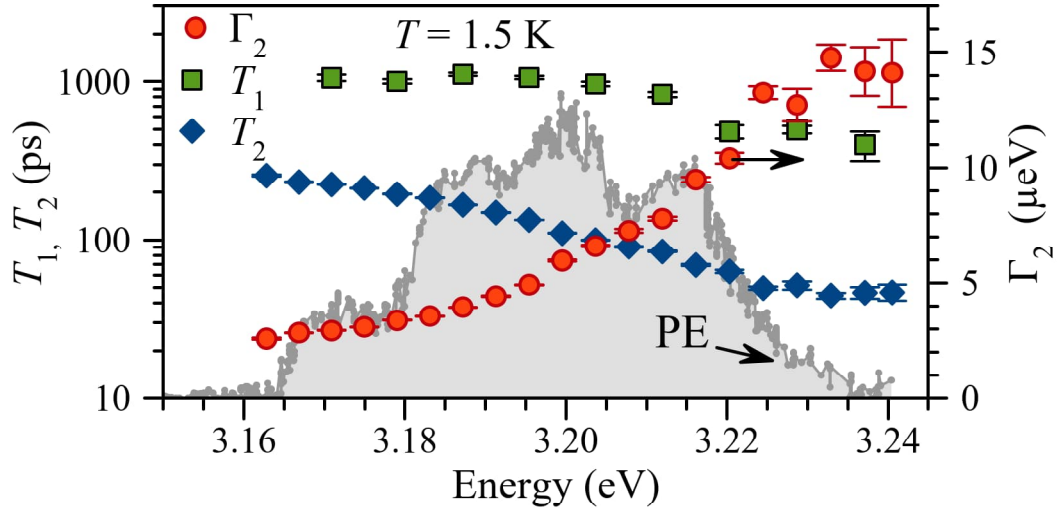Figure 33: (a) Spectral dependence of times T_1 (green), T_2 (blue) and rate Γ_2 (red) within the spontaneous PE spectrum (grey) from figure 31.

Similarly, spectral measurements of the three-pulse SPE decay were carried out. During the measurements, for a given photon energy, we scanned the delay τ_{23} while delay τ_{12} was fixed and the SPE amplitude was detected. The measurements

show exponential decay $\propto \exp(-\tau_{23}/T_1)$ with the population relaxation time T_1 . Experimental curves for a set of photon energies are shown in figure 34. The data demonstrate non-trivial population dynamics in the initial time period. Approximation of the curve section with $\tau_{23} > 50$ ps gives the spectral dependence T_1 shown in figure 33. The dependence also shows a monotonic increase of time T_1 from 0.4 to 1 ns with decreasing photon energy inside the exciton spectral range. The obtained values of T_1 are several times larger than the corresponding values of T_2 and are closer to the exciton lifetimes τ_0 extracted from time-resolved PL kinetics, which are in the range $0.9 - 2$ ns. For the segment $\tau_{23} < 50$ ps, due to the lack of a dynamic range of the SPE amplitude change, one can only give an approximate estimate of the relaxation time T_1 in the range of 50-100 ps, which is much closer to the obtained values of the dephasing time T_2.
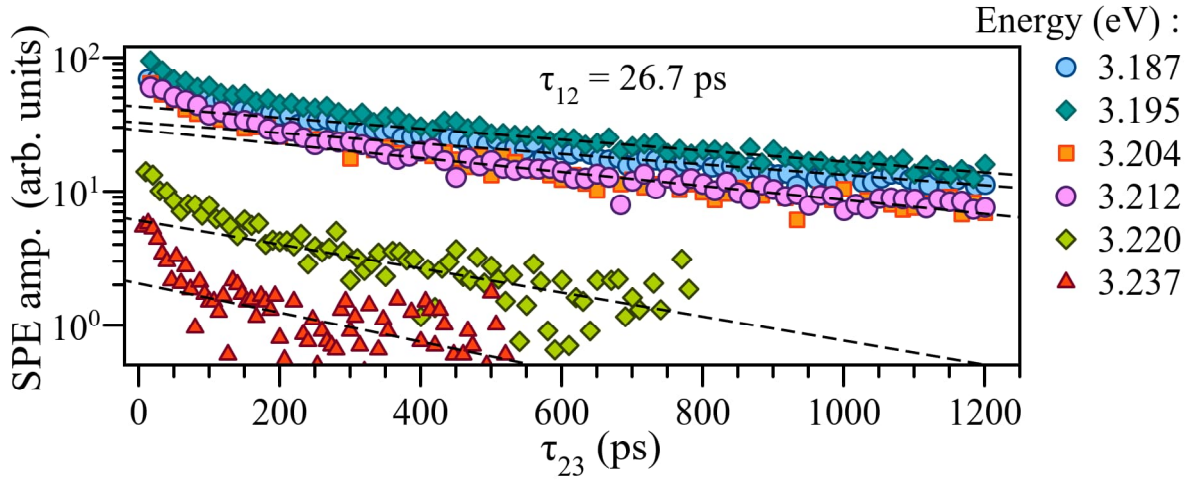

Figure 34: SPE decay kinetics (dots) measured at several values of photon energy with superimposed exponential approximation (dashed).

4.5 Temperature dependent measurements of photon echo

The influence of phonons on the coherent dynamics of excitons can be analyzed by measuring the FWM signal decay kinetics at different temperatures [101, 105, 156–159]. The strength of this method for studying exciton and trion dephasing processes in ZnO/(Zn,Mg)O MQWs is demonstrated in the previous chapter, so we applied the approach to study (In,Ga)N/GaN multiple QW. The PE and SPE decay kinetics of excitons measured at photon energy $\hbar\omega = 3.183$ eV and different sample temperatures are shown in figure 35(a) and (b) respectively. The spontaneous PE signal decays much faster with increasing temperature, while the SPE decay
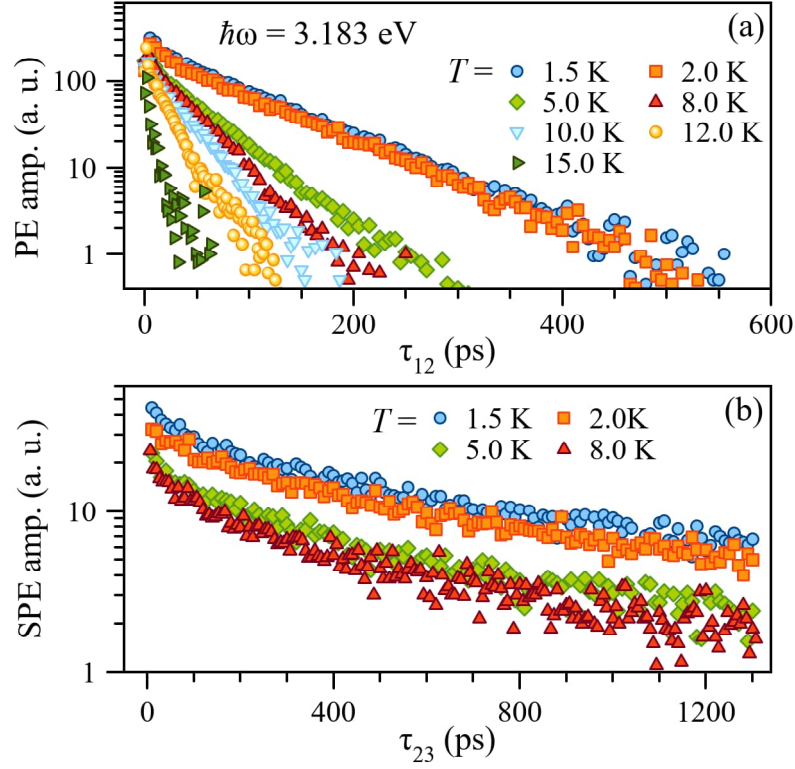
Figure 35: Spontaneous PE (a) and SPE (b) decay kinetics measured at different temperature.

kinetics mainly experience only a decrease of the amplitude at a fixed delay τ_{23}, while the decay rate does not change significantly in the available temperature range. Approximation of the kinetics by exponential function gives us the temperature dependence of T_1, T_2 and the corresponding Γ_1, Γ_2 values, which are shown in figure 36(a) and (b).

The temperature dependence of the dephasing rate can be approximated by the dependence $\Gamma_2 = \Gamma_2^0 + \gamma T + b_1/(e^{E_1/k_B T} - 1)$, plotted in figure 36 (b). The linear increase at $T < 10$ K with the coefficient $\gamma = 0.7$ μeV/K corresponds to dephasing due to scattering of excitons by acoustic phonons. The extracted coefficient γ is close to the value we obtained for trions in the ZnO/(Zn,Mg)O MQW and to the reported values for donor-bound excitons in the ZnO epitaxial layer [101] (≈ 2 μeV/K).

The nonlinear increase in the dephasing rate at $T > 10$ K cannot be related to scattering by longitudinal optical phonons, whose energy is about 90 meV in such structures. Approximation by an activation-type dependence gives the value $E_1 = 5.7$ meV, which can characterize the typical localization energy. A similar behavior of the dephasing rate was previously observed for localized excitons in QDs [180]. Thus, we see that acoustic phonons can significantly affect the coherent
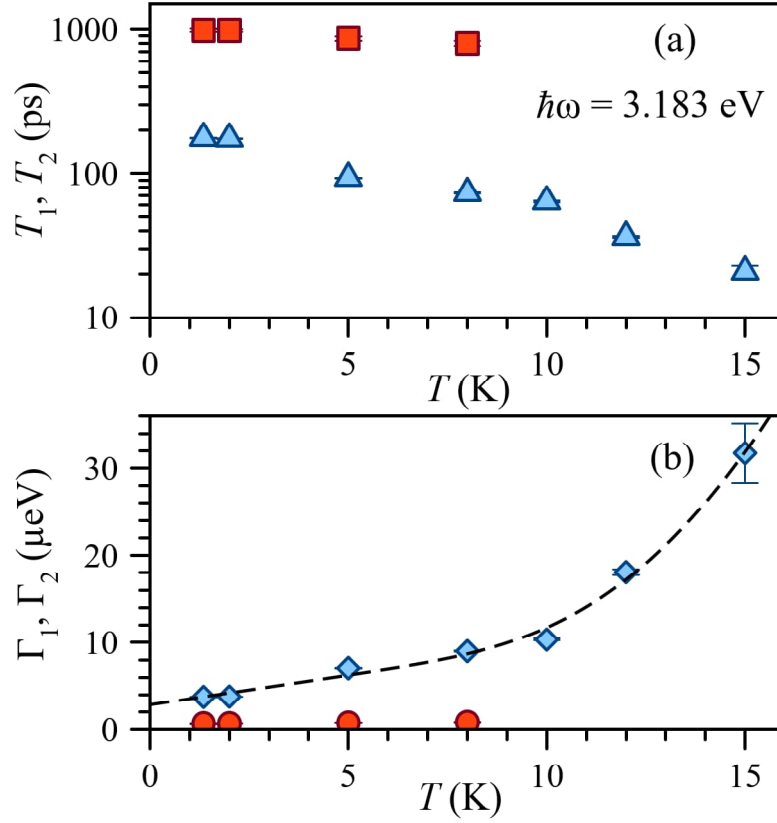
Figure 36: Temperature dependence of times T_1, T_2 (a) and corresponding rates Γ_1, Γ_2 (b).

dynamics of excitons in (In,Ga)N/GaN QWs.

4.6 Discussion

The spectral dependencies of the exciton energy and phase relaxation times $T_{1,2}$ can be related to the influence of exciton localization in QW fluctuating potential. The observed monotonic growth of T_1 and T_2 with decreasing exciton transition energy resembles the spectral dependence of the relaxation times of the T_A trions in the ZnO/(Zn,Mg)O MQW which was considered in the previous chapter. However, (In,Ga)N/GaN nanosctructures are substrantionally different due to the presence of a significant compositional inhomogeneity, the nature of which significantly depends on the growth technology. During the growth of the sample under study, special attention was paid to reducing the inhomogeneous broadening [169]. Nevertheless, a significant Stokes shift of about 20 meV at $T = 300$ K and 40 meV at $T = 1.5$ K reveals a pronounced spatial localization of excitons in the QW and consequently a large inhomogeneity.

The peculiarities of potential fluctuations in (In,Ga)N/GaN QWs as well as the causes of their origin were studied by various methods, such as transmission electron microscopy [168], near-field optical microscopy [181], and scanning tunneling luminescence spectroscopy [182]. In the last work, it was shown that the micro-photoluminescence spectra show the presence of significant potential fluctuations with characteristic sizes of about 3 nm, which can be considered as fluctuation quantum dots. Exciton Bohr radius in GaN is also about 3 nm [183], so we can assume that localization and piezoelectric effects make an impact on the radiative relaxation rate, which determines T_1.

Another possible reason for the increase of the exciton relaxation rate with increasing transition energy is the enhancement of the light-exciton interaction due to the special spatial periodicity of the structure. When the condition of Bragg diffraction from the QWs at the exciton transition frequency is satisfied, a superradiant exciton-polariton mode arises in the QW as a result of the electromagnetic coupling of the N QW, and the radiative decay rate increases N times [184]. Such effects were observed in FWM experiments in GaAs-based Bragg structures [185]. However, as mentioned earlier, the PE signal was measured in a longer wavelength range than the spectral location of the Bragg peak at helium temperatures (3.392 eV), so we do not expect such an effect in our case. Moreover, the observed large inhomogeneous broadening of about 43 meV compared to the homogeneous width on the order of 20 μeV makes a superradiant regime at low temperatures highly inlikely .

Temperature measurements showed a relatively weak effect of acoustic phonons on exciton dephasing with a linear coefficient of 0.7 μeV/K. This fact also indicates a strong localization of excitons in the fluctuating potential similar to the potential of fluctuating quantum dots. For comparison, the linear coefficient for exciton-phonon scattering in InGaAs/GaAs QDs was as small as $\gamma = 0.5$ μeV/K [186], or was absent up to the measurement accuracy [180].

The presented study of the picosecond coherent dynamics of excitons in (In,Ga)N/GaN QWs is the first work of this kind, so direct comparison of the obtained results with published works becomes difficult. In most of the works devoted to the study of strongly localized excitons the micro-photoluminescence method was used to study the properties of individual states at low temperatures. The PL spectra of a single $In_{0.15}Ga_{0.85}N$/GaN QW 3 nm thick at $T = 4$ K have peaks corresponding to individual exciton states with linewidths up to 800 μeV [187]. The

implementation of mesas with size of 0.2 μm for $In_{0.1}Ga_{0.9}N/GaN$ MQWs made it possible to observe the PL lines of individual highly localized excitons with a width of 400 μeV at $T = 4$ K [188]. The authors also concluded that spatial indium accumulation leads to the localization of excitons at the QD-like potential minima. For comparison, we can estimate the homogeneous width $2\hbar\Gamma_2$ for $T = 4$ K. Taking into account the contribution of the exciton-phonon interaction $2\gamma T \approx 6$ μeV, the width $2\hbar\Gamma_2$ is in the range of 11–35 μeV depending on the transition energy. The value is an order of magnitude smaller than the previously reported values obtained by micro-PL spectroscopy. As a possible reason for the value discrepancy, one can suggest the influence of the broadening of the PL spectral lines due to spectral wandering (spectral jitter) caused by the fluctuation of the static potential during signal acquisition.

4.7 Conclusion

We have detected a photon echo signal in the ultraviolet range from localized excitons in a periodic structure with (In,Ga)N/GaN QWs. Utilizing the two-pulse picosecond PE technique, we were able to measure the homogeneous width of localized excitons with spectral resolution at helium temperature. The obtained experimental data showed the coherent dynamics of excitons in our structure at much longer timescale compared to previous studies of similar structures with a higher indium content by the micro-photoluminescence. The exciton dephasing time reaches 255 ps, which is much longer than the typical dephasing times for localized excitons in quantum wells A^{III}-B^V GaAs/(Al,Ga)As [157], (In,Ga)As/GaAs [189] and A^{II}-B^{VI} structures CdTe/(Cd,Mg)Te [115] and ZnO/(Zn,Mg)O [154], in which dephasing times are in the range of tens of picoseconds. Spectral measurements demonstrate a monotonic fivefold increase of the dephasing time as the localization of excitons increases.

Chapter 5. Spin-dependent photon echo from excitons in InGaAs/GaAs quantum well subject to a transverse magnetic field

This chapter presents an experimental study of the spin-dependent photon echo from an ensemble of excitons in a thin (In,Ga)As/GaAs quantum well subject to a magnetic field applied along the sample plane. The chapter contains a brief introduction, a description of the sample, experimental data on linear and nonlinear spectroscopy of exciton resonance, an analysis of the model describing optical coherence precession between bright and dark exciton states, and a comparison of experimental results with theoretical predictions. The main results of the chapter are reflected in the author's publications [144, 190, 191].

5.1   Introduction to chapter

The preservation of coherence is a key property of the system considered as a platform for all-optical information processing in the classical and quantum way. In this context, increasing the dephasing time of the system is a relevant task. The potential of the spin-dependent PE technique as a powerful nonlinear tool for investigating the coherent dynamics of exciton complexes in nanostructures is demonstrated in the section 1.3.2. The combined use of the action of light pulses on the structure and the application of an external magnetic field makes it possible to combine the advantages of these two phenomena and obtain ultrafast optical control of the system state and long-lived information storage in the spin subsystem [127, 128].

Coherent control protocols based on spin-dependent PE involve, as an obligatory initial step, the transfer of optical phase information between states with different spin projections by applying a transverse magnetic field. The implementation of this step imposes a condition on the system $T_2 > 2\pi/\Omega$, where T_2 is the optical dephasing time and Ω - angular Larmor precession frequency. In the case of relatively small magnetic fields $B \approx 1$ T, suitable systems are an ensemble of trions [127, 128] or donor-bound excitons [129] with long time T_2 and a relatively large g-factor value. However, the use of neutral excitons in this kind of protocol has not been successfully implemented so far. The limiting factors include the fast

dephasing of excitons, as was shown in chapter 3.

This chapter will present original research on the application of neutral excitons as a platform for coherent optical control with a spin degree of freedom. For this purpose, we have chosen a model system, which is a high-quality sample with a single (In,Ga)As/GaAs QW. Previous studies of such structures have demonstrated an extremely low non-radiative broadening of the exciton spectral lines, whose value is comparable with the radiative width determined by the radiative recombination rate [81]. Such structures manifest an effective transfer of optical coherence into the exciton system, which allows us to observe a relatively long time T_2. It gives us a fundamental opportunity to observe several periods of oscillations of electron and hole spins in the exciton in the spin-dependent PE signal.

The fundamental difference between charged and neutral excitons lies in the energy level structure discussed in section 2.2. In addition to bright excitons that actively interact with light, there are dark excitons that do not directly interact with light. In the case of GaAs-based QWs, such states are excitons with the total angular momentum projection onto the growth axis of the structure $S_z = \pm 2$, for which optical transitions are forbidden. Such dark excitons do not have a direct radiative recombination channel, so their T_1 time must be longer than the T_1 time of bright excitons. If the main mechanism of phase relaxation is associated with energy relaxation, then a similar relationship is also expected for dephasing times T_2.

Information about dark exciton states can be obtained in various ways. The incoherent luminescence of dark excitons was found in two-dimensional structures of transition metal dichalcogenides by applying a transverse magnetic field of tens of Tesla [192, 193], as well as by using the coupling with surface plasmon polaritons [194]. Dark exciton emission has also been demonstrated in QW [195], QD [196] and carbon nanotubes [197]. For coherent control of the dark exciton spin state, biexciton states were used without the application of an external magnetic field in single QDs [198, 199]. The FWM revealed spin-flip transitions between bright and dark excitons in GaAs/AlGaAs QWs [200] and colloidal CdSe/CdS QDs [201]. It is also worth mentioning the work on the study of the influence of a magnetic field on the exciton coherent dynamics on the femtosecond time-scale [202, 203]. The oscillations in the two-pulse PE signal as a result of mixing of bright and dark excitons were modelled theoretically [136], but have not been experimentally

demonstrated so far. In this chapter, we provide the experimental implementation of such a protocol for a spin-dependent picosecond two-pulse photon echo, which includes long-lived dark excitons.

5.2 The sample under study

A high-quality sample was grown by molecular beam epitaxy on a GaAs substrate along the (100) direction. The sample was grown at the Nanophotonics Resource Center at SPbSU. During the growth process, the substrate was rotated to increase the homogeneity of the structure. A 1000 nm thick GaAs buffer layer was grown on the substrate, followed by a single 3 nm thick InGaAs quantum well with an indium concentration of about 3–4 %. The cap layer of GaAs with a thickness of 170 nm was grown on a QW layer.

5.3 Linear spectroscopy of the structure

The basic optical properties of the structure were determined using linear techniques such as reflection and PL spectroscopy. Reflection spectroscopy was carried out at a low optical excitation density in order to minimize nonlinear effects. Optical excitation was carried out at the Brewster angle by linearly polarized light, the electric field vector of which lies in the plane of incidence (p-polarization). The laser beam was focused into a spot 150×50 µm. The resonant reflection of light from a QW in such a geometry was considered in the 1.2.3 section, and the reflectivity spectrum in the vicinity of the exciton resonance can be approximated by the Lorentzian curve, according to the expression 7 [189, 204]. The approximation makes it possible to determine the values of the radiative width $\hbar\Gamma_0$ and the nonradiative broadening $\hbar\Gamma_{\mathrm{NR}}$.

The reflectivity spectrum from a sample with an (InGa)As/GaAs QW at $T = 10$ K is shown in figure 37(a). One can see an isolated resonance corresponding to the transition of a heavy hole exciton in a QW (X). The peak is centered at the photon energy $E_X = 1.510$ eV and has an amplitude of 0.1 and a half-width at half-maximum (HWHM) of 105 µeV. Approximating the peak by the Lorentzian contour, which is shown by the dash-dotted line, we obtain the values for the radiative width $\hbar\Gamma_0^X = 35 \pm 3$ µeV and the non-radiative broadening $\hbar\Gamma_{NR}^X = 70 \pm 3$ µeV. The ratio $\hbar\Gamma_{NR}^X \approx 2\hbar\Gamma_0^X$ gives us an estimation of the efficiency of optical coherence transfer
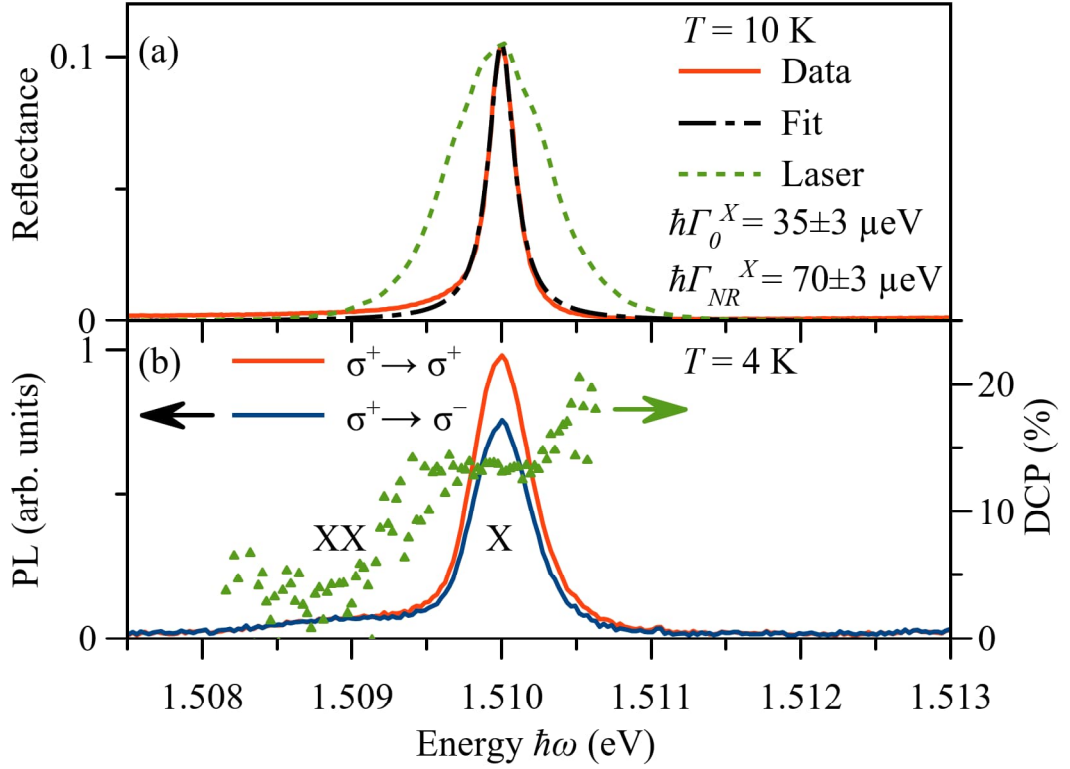
Figure 37: (a) Reflectivity spectrum measured in the Brewster geometry (solid), fitting by Lorentzian curve (long-and-short-dashed curve), and excitation laser spectrum (short-dashed curve) used for the FWM experiment. (b) PL spectra for $\sigma\pm$ polarized excitation and copolarized (red) and cross-polarized (blue) detection and DCP spectrum (triangles).

between light and excitons which indicates the high quality of the sample.

The PL spectra measured at $T = 4$ K are shown in figure 37(b). For excitation, laser radiation with circular polarization ($\sigma+$) was tuned to exciton resonance in bulk GaAs ($\hbar\omega = 1.515$ eV). The beam was focused on the sample surface into a spot about 50 μm in diameter. The PL signal was detected in copolorized $\sigma+$ (red curve) and cross-polarized $\sigma-$ (blue curve) circular polarization. With these measurements, the degree of circular polarization of the PL signal was calculated as follows: $DCP = \frac{I^+ - I^-}{I^+ + I^-}$, where $I^\pm$ is the intensity of co-circularly-polarized (cross-circularly-polarized) PL with respect to the excitation polarization. The main peak corresponding to the X exciton has almost no Stokes shift with respect to the line in the reflectivity spectrum. On the low-energy side, an additional peak is observed, which we attribute to the emission of heavy hole biexcitons (XX). One of the arguments in favor of such an identification is the lower degree of DCP in the XX region compared to the exciton luminescence X, which partially preserves the initial polarization of the exciting light, as shown in figure 37(b). Such behavior

is typical for an exciton-biexciton system [205]. The splitting between the peaks $E_{b(XX)} = 1.1 \pm 0.2$ meV is close to the published biexciton binding energies in GaAs/AlGaAs and InGaAs/GaAs QWs [205–207].

These measurements demonstrate how important it is to utilize the picosecond laser technique for studying the exciton coherent optical dynamics in this case. Femtosecond excitation by pulses with a spectral width of the order of 20 meV was extensively used to study similar structures by FWM and PE [104, 207–209]. Such spectrally broad excitation leads to the instantaneous excitation of various ensembles of quasiparticles, including excitons, trions, and biexcitons. As a result, the FWM signal exhibits a nontrivial oscillating temporal behavior even in the absence of an external magnetic field. The use of spectrally narrow picosecond laser pulses in this work allows us to selectively address only the exciton ensemble eliminating many-body interactions. Thus, the following PE measurements were carried out with the laser tuned to the X exciton resonance, so we can omit biexciton states in the subsequent data analysis.

5.4   Photon echo from excitons in (In,Ga)As/GaAs QW
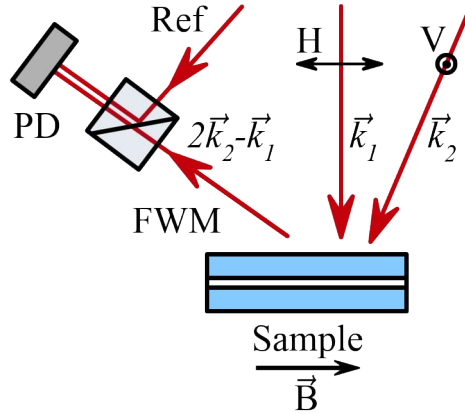
Figure 38: The schematic of excitation and detection of PE signal from the sample with InGaAs/GaAs QW subject to an in-plane external magnetic field (Voigt geometry).

To study the coherent dynamics of excitons subject to a transverse magnetic field, we used the technique of a spin-dependent two-pulse spontaneous PE. To carry out these experiments, an experimental setup was built at Resource Center "Nanophotonics" of St. Petersburg State University, the scheme of which and the

Figure 39: (a) Temporal profile of spontaneous PE from excitons in QW, measured at several delays τ_{12}.

principle of operation are described in the section 50. The schematic of the current implementation of the setup is shown in figure 38. The key feature compared to previous experiments is the application of an external transverse magnetic fi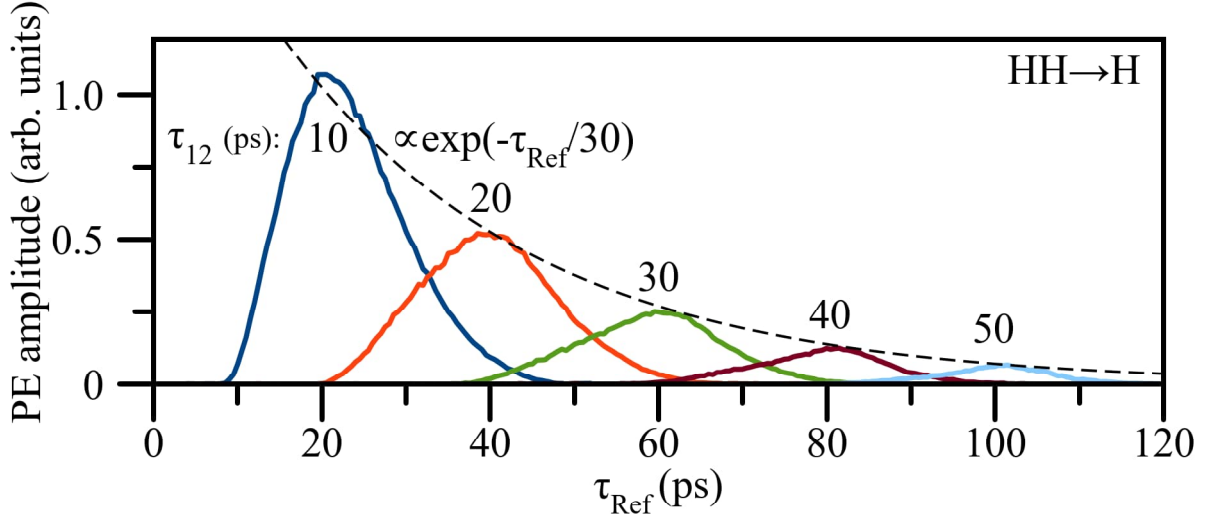eld $\vec{B}$, which is directed along the sample plane and is parallel to the horizontal direction of the laboratory frame of reference (H), while the light is incident close to normal to the sample plane. This configuration corresponds to the Voigt geometry. The measurements were carried out using linear polarized excitation and detection. The polarization configuration is denoted below as $XY \rightarrow Z$, where X and Y are the polarization of the first and second exciting pulses, and Z is the detected signal polarization. The main polarizations of the experiment: horizontal (H), parallel to the vector $\vec{B}$, and vertical (V), orthogonal to the vector $\vec{B}$.

5.4.1 Zero magnetic field

Figure 39 demonstrates the FWM signal from an exciton ensemble in the (In,Ga)As/GaAs QW, measured with a picosecond time resolution in the HH→H geometry at zero magnetic field for several delays τ_{12}. The signal, as expected, has a form of the spontaneous PE peak, which reaches its maximum at the time $\tau_{Ref} = 2\tau_{12}$. In contrast to the ZnO/(Zn,Mg)O and (In,Ga)N/GaN structures, the shape of the echo profile from the exciton ensemble under study tends to the form of a Gaussian peak with FWHM of about 20 ps when τ_{12} increases. Note that the depicted signal is a cross-correlation between the FWM signal and the reference
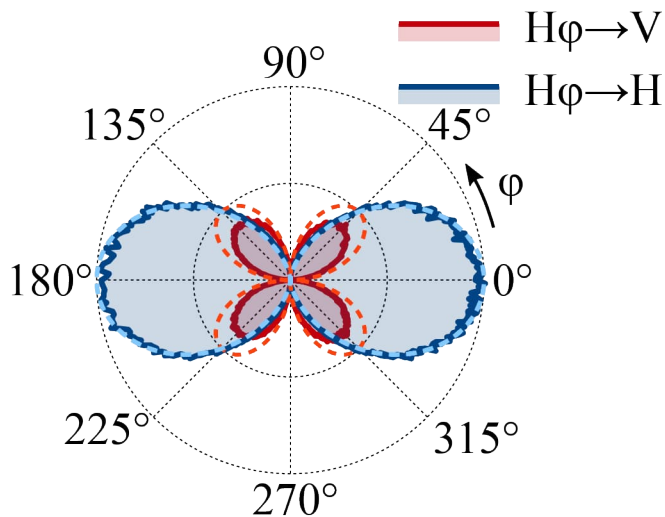
Figure 40: PE amplitude at $\tau_{12} = 15$ ps as a function of the angle between the linear polarization planes of the first and second exciting pulses φ, when the first pulse is polarized along the H direction, and detection was performed along the H direction (blue) and orthogonal V direction (red). The solid and dashed lines correspond to the experimental data and theoretically predicted response, respectively [135].

pulse with FWHM of 3 ps. However, such a long time profile of cross-correlation allows us to assume that the detected signal reflects the near-true temporal profile of the PE while the additional broadening due to convolution of the signal with the reference pulse can be neglected. Such a long duration of the PE signal corresponds to a relatively small inhomogeneous broadening of the frequency distribution about 92 μeV. As the delay τ_{12} increases, the PE peak decays exponentially with the dephasing time $T_2 = 30$ ps. Further, we will focus on the magnitude of the peak PE amplitude, that is, the magnitude of the cross-correlation signal at $\tau_{Ref} = 2\tau_{12}$.

To confirm the excitonic nature of the ensemble under study, we applied the recently developed method of PE polarimetry [135, 136]. Since excitons and trions (as well as donor-bound excitons) have different polarimetric dependencies of the PE on the polarization excitation configuration, we can use this property to determine the type of quasi-particles that form the PE signal. The analysis of these dependencies is given in 2.2. In particular, when the exciton ensemble is excited by linearly polarized pulses rotated relative to each other by an angle φ, the PE signal will also be linearly polarized, the polarization plane will coincide with the one of the second pulse, while the amplitude of the signal will depend harmonically on φ $\propto \cos(\varphi)$ [135].

Polarimetric measurements of the PE signal are shown in figure 40. They represent the dependence of the PE amplitude on the angle φ when a linearly polarized

signal is detected along direction H (blue curve) and V (red curve) and the first excitation pulse was always linearly polarized along direction H. The curve H$\varphi \to$H has two maxima of the same amplitude, and the curve H$\varphi \to$V has four symmetrical maxima, the amplitude of which is almost half the value of the maxima of the curve H$\varphi \to$H. This is indeed the behavior which is theoretically expected for the exciton model (shown in figure 40 by the dotted line), and which has been demonstrated on the exciton ensemble in the CdTe/(Cd,Mg)Te QW [135]. The qualitative agreement between the experimental data and theoretical simulations confirms the fact that the investigated resonance corresponds to an ensemble of neutral excitons.

5.4.2   Photon echo in a transverse magnetic field

The key experiment of this work is the measurement of the PE amplitude decay when time delay τ_{12} is scanning which we will call PE decay. Figure 41 shows a set of such decays measured in HH→H (a) and VV→V (b) geometries when an external transverse magnetic field (Voigt geometry) is applied in the range $B = 0 - 6$ T. In a zero magnetic field, the behavior is identical for both geometries, characterized by a monoexponential decay with bright exciton dephasing time $T_2^b = 30$ ps. Note that these curves show no sign of exciton-biexciton beats [209] since the picosecond technique allows us to fine-tune the central laser wavelength to exciton resonance. This fact allows us to omit the biexciton states in our further theoretical consideration.

The application of a transverse magnetic field in the Voigt geometry along the H direction, leads to a radical change in the signal. Oscillations begin to appear in the PE decays in both geometries. In the case of HH→H, the frequency of these beats increases monotonically with the field B, while in the VV→V geometry the kinetics changes slightly in the range of fields $B \geq 2$ T. Let us also note that the signal experiences nontrivial behavior at $B = 1$ T in the geometry HH→H and at magnetic fields from 1 T to 6 T in the geometry VV→V. In these cases, instead of harmonic oscillations, we observe aperiodic regime, at which PE signal reaches a minimum only once and then decays with a longer characteristic time compared to the initial T_2^b. All these peculiarities point to the importance of constructing a theoretical model that correctly describes the dependence of the PE signal on delay τ_{12}, magnetic field B, and polarization configuration.
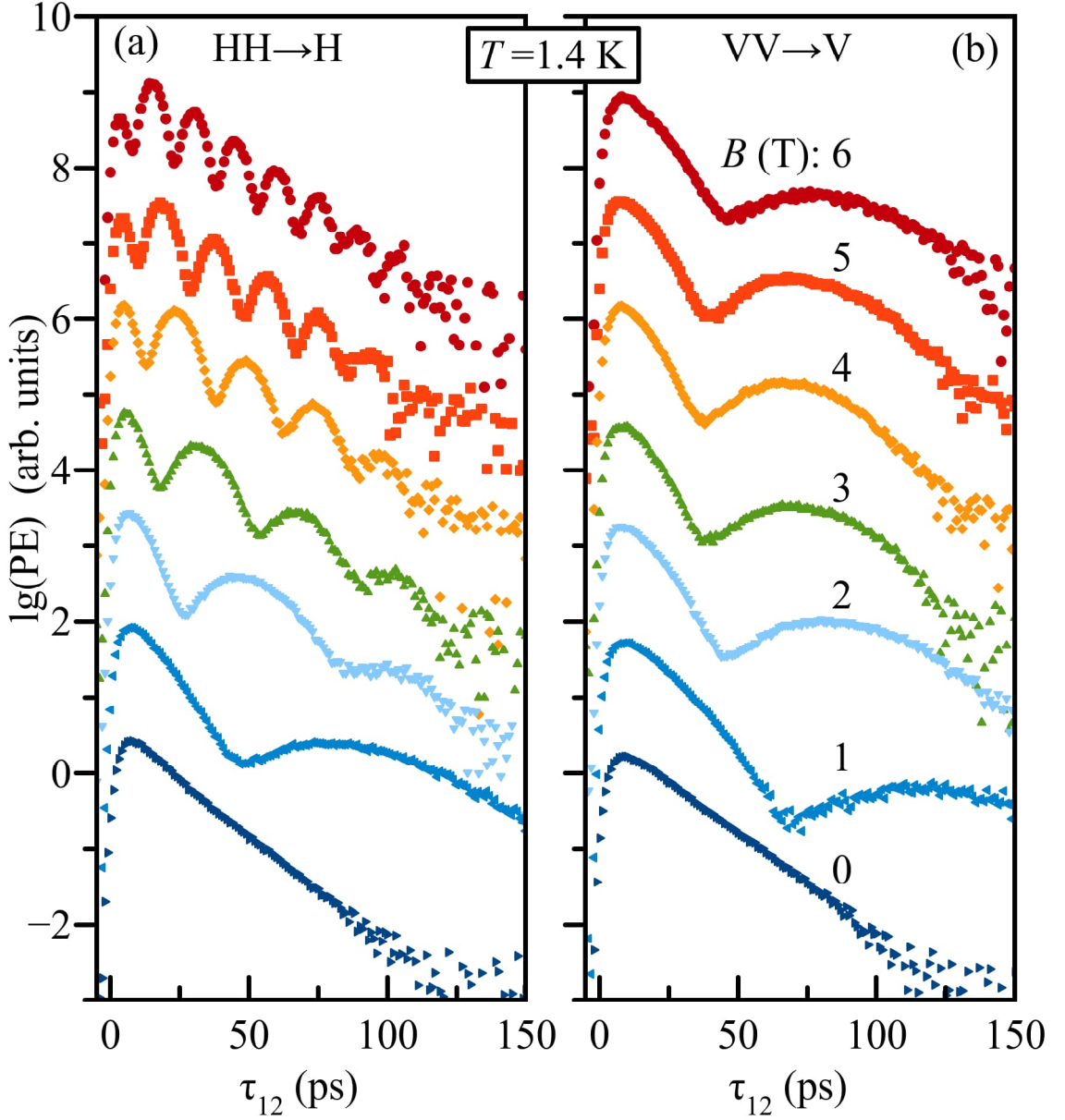
Figure 41: The kinetics of decay kinetics of PE amplitude from excitons subject to transverse magnetic field (Voigt geometry). The curves are offset vertically for clarity.

5.5 Model of an exciton ensemble in a quantum well subject to a transverse magnetic field

Let us consider the model of excitons with a heavy hole in a QW, which is described in the section 2.2. It consists of 5 states characterized by the projection of the total angular momentum (for brevity, we will call it spin below) onto the quantization axis S_z: the ground state of the crystal with $S_z = 0$, a pair of bright exciton states with $S_z = \pm 1$, and a pair of dark exciton states with $S_z = \pm 2$. The

Figure 42: Schematic representation of exciton states and the interaction of excitons with light in a transverse magnetic field. Black arrows indicate allowed optical transitions under the action of circularly polarized light $\sigma\pm$, dotted ellipses correspond to the Larmor precession of the electron (blue) and heavy hole (red) spins.

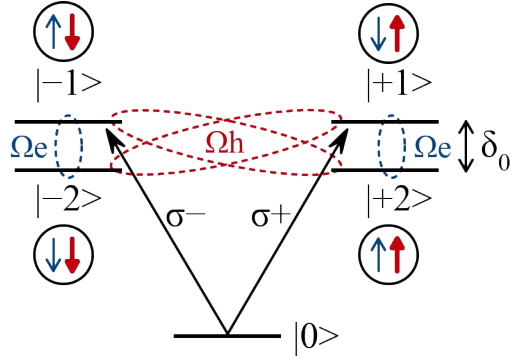level scheme is shown in figure 42. These excitons are formed from electrons in the conduction band with spin $s^e = 1/2$ ($l^e = 0$, $s^e = 1/2$) and heavy holes in the valence band with spin $j^{hh} = 3/2$ ($l^{hh} = 1$, $s^{hh} = 1/2$) [58, 139, 210, 211].

Let us show that the observed oscillations in the PE decays are caused by the action of a magnetic field on excitons. The transverse magnetic field in the Voigt geometry causes the Larmor precession of the electron and hole spins in the exciton, depicted by dotted ovals in figure 2.2. The precession of the electron spin projection $s_z^e = \pm 1/2$ leads to the mixing of bright exciton states $S_z = +1$ ($S_z = -1$) with dark states $S_z = +2$ ($S_z = -2$), while the heavy hole spin precession $j_z^{hh} = \pm 3/2$ mixes the states $S_z = +1$; ($S_z = -1$) with states $S_z = -2$ ($S_z = +2$) [58, 143, 212]. Indeed, such mixing of bright and dark excitons occurs during the formation of photon echo [127, 128].

The spin-dependent PE experiment can be considered analytically by solving the Lindblad equation (23) for the exciton density matrix ρ by analogy with the case discussed in section 2.1.4. The same approach was used to analyze the spin-dependent PE from trions in the CdTe/(Cd,Mg)Te [127, 130]. The equation has the following form:

$$\dot{\rho} = -\frac{i}{\hbar}[\hat{H}, \rho] + \Gamma, \tag{39}$$

where $\hat{H}$ is the Hamiltonian of the exciton system, and Γ is the phenomenologically introduced relaxation matrix containing only phase relaxation terms. In our case, it is important to take into account the dephasing rates for both bright γ_b and dark γ_d excitons. The Hamiltonian includes three terms describing the unperturbed exciton system, the interaction with light, and the action of a transverse magnetic field,

respectively. In a zero field, the exchange interaction between an electron and a hole in an exciton causes a splitting of the exciton states, as shown in section 2.3. The splitting between doublets of bright and dark excitons is determined by the isotropic exchange interaction constant δ_0. The anisotropic exchange interaction leads to an additional splitting of these doublets [58, 143], but we will not take it into account for simplicity of calculations, since the anisotropic exchange interaction is usually much weaker than the isotropic one. The total Hamiltonian has the following form in the basis of exciton states $S_z = \{0; +1; -1; +2; -2\}$:

$$\hat{H} = \frac{\hbar}{2}\begin{pmatrix} 0 & f_+^* e^{i\omega t} & f_-^* e^{i\omega t;} & 0 & 0 \\ f_+ e^{-i\omega t} & 2\omega_0 + \delta_0/\hbar & 0 & \omega_e & \omega_h \\ f_- e^{-i\omega t} & 0 & 2\omega_0 + \delta_0/\hbar & \omega_h & \omega_e \\ 0 & \omega_e & \omega_h & 2\omega_0 - \delta_0/\hbar & 0 \\ 0 & \omega_h & \omega_e & 0 & 2\omega_0 - \delta_0/\hbar \end{pmatrix}. \tag{40}$$

Here ω_0 is the angular frequency of the exciton resonance, ω is exciting light angular frequency, ω_e and ω_h are the angular frequencies of the Larmor precession of the electron and hole spins, respectively, and $f_\pm$ is the coefficient proportional to the envelope of the circularly polarized components of exciting light pulse $E_{\sigma\pm}$:

$$f_\pm(t) = -\frac{2e^{i\omega t}}{\hbar} \int \mathrm{d}(\boldsymbol{r}) E_{\sigma_\pm}(\boldsymbol{r}, t) d^3 r, \tag{41}$$

where $\mathrm{d}(\boldsymbol{r})$ is the transition matrix element of the dipole moment between the ground state and the bright exciton state. Rotating wave approximation will be used for the calculation, we will also assume that the time profile of the laser pulses has a rectangular shape. A further significant simplification is to separate in time the interaction with the laser pulses and the evolution of the system at the rest of the time [127–129, 136]. Such a procedure is justified, since the pulse duration (3 ps) is significantly shorter than the dephasing times and the Larmor precession period at the considered magnetic field range. Therefore, we can neglect relaxation and precession in the magnetic field during the action of the pulses.

The analysis shows that the macroscopic polarization is determined by the elements of the density matrix ρ_{12} and ρ_{13}, which, as a result of integration over an ensemble of excitons with an inhomogeneously broadened resonant frequency ω_0,

has a maximum in the form of an echo pulse at $t = 2\tau_{12}$. The final expression for the PE amplitude, P, for collinear linearly polarized excitation and detection has the form:

$$P(\alpha) \propto e^{-2\gamma\tau_{12}} \underbrace{\left| R_H \cos^2\alpha + R_V \sin^2\alpha \right|^2}_{R}, \tag{42}$$

where $\gamma = \frac{\gamma_b + \gamma_d}{2}$ is the average dephasing rate, α is the angle between the light polarization plane and the magnetic field direction. Components $R_{H,V}$ are defined as follows:

$$R_{H,V} = \cos(\Omega_{H,V}\tau_{12}) + \frac{i\frac{\delta_0}{2\hbar} - \Delta\gamma}{\Omega_{H,V}} \sin(\Omega_{H,V}\tau_{12}), \tag{43}$$

where $\Omega_{H,V}$ is the effective Larmor precession frequency:

$$\Omega_{H,V} = \sqrt{\Omega_{H0,V0}^2 + \left(\frac{\delta_0}{2\hbar} + i\Delta\gamma\right)^2}, \tag{44}$$

$$\Omega_{H0,V0} = \frac{\omega_e \pm \omega_h}{2}, \quad \Delta\gamma = \frac{\gamma_b - \gamma_d}{2}. \tag{45}$$

P has the simplest form for $\alpha = 0°$, corresponding to the geometry HH→H (see figure 38), and for $\alpha = 90°$ (VV→V geometry), therefore the main measurements were carried out in these polarization configurations.

5.6   Experimental results and discussion

The expression for P (42) makes it possible to describe all the presented PE decays in the entire available range of the magnetic field. Below we will consider in more detail the most significant features of the model in comparison with experimental data. To do this, we will refer to figure 43, where the most illustrative cases are provided.

In a zero field, the expression (42) reduces to a monoexponential decay $P \propto e^{-2\gamma_b\tau}$ corresponding to the classical case of PE from an ensemble of bright excitons, the fitting of the data is shown in figure 43(a). For $B > 0$, an oscillating term R is superimposed on the exponential damping. The coherence oscillation between light and dark exciton states with different dephasing rates $\gamma_{b,d}$ leads to significant changes, namely the precession frequency $\Omega_{H,V}$ henceforth depends on the difference $\Delta\gamma$. The expression for R can be represented as a combination of oscillating and non-
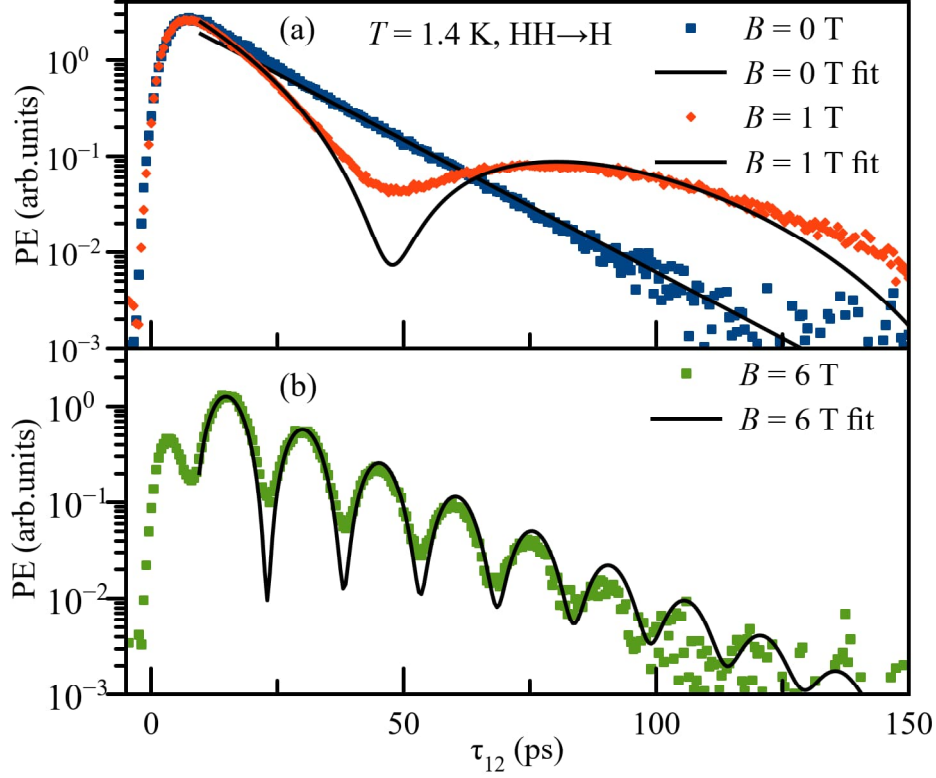
Figure 43: Photon echo decays from excitons (dots) and fit by the model 42 (solid) at $B = 0; 1$ T (a) and $B = 6$ T (b).

oscillating components, the ratio between which determines the temporal behavior of the signal. However, under the conditions $\Delta\gamma \ll |\Omega_{H0,V0}|$ and $\delta_0/\hbar \to 0$, the behavior is close to the product of exponential decay and a single frequency harmonic function. If the dephasing rates are the same $\gamma_b = \gamma_d$ the expression (42) coincides with the result of the previous modelling [136]:

$$P_{H,V} \propto e^{-2\gamma_b\tau_{12}} \left(\cos^2(\Omega_{H,V}\tau_{12}) + \frac{\delta_0^2}{4\hbar^2} \frac{\sin^2(\Omega_{H,V}\tau_{12})}{\Omega_{H,V}^2} \right). \tag{46}$$

A similar situation with a small decay time correction is realized for large fields $B \geq 3$ T in the HH→H geometry, as shown in figure 41. The most illustrative case is observed at $B = 6$ T, which is shown together with the approximation in figure 43(b). The implementation of the automated fitting made it possible to simultaneously fit a series of experimental curves measured in the geometries HH→H, VV→V DD→D, and DX→D using common fitting parameters. The indices D and X correspond to linear polarizations rotated with respect to the direction of the field (H direction) by the angle $\pi/4$ and $3\pi/4$. The DX→D geometry corresponds to cross-linear excitation and signal detection, and the expression for the PE ampli-
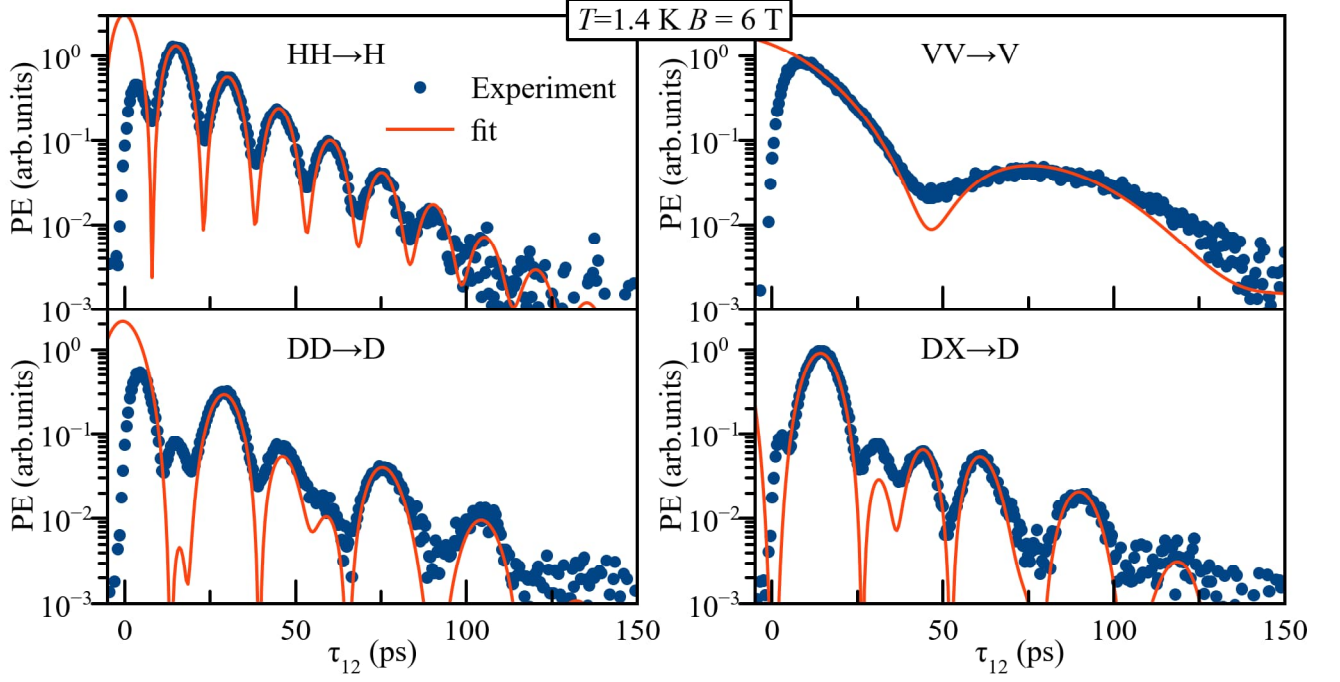
Figure 44: Exciton PE decay (blue dots) at $B = 6$ T, measured in various polarization geometries. Red line illustrates the fit with common parameters for all four measurements.

tude in this geometry has the form:

$$P_{DX \to D} \propto e^{-2\gamma\tau_{12}} | \cos(\Omega_H \tau_{12}) - \cos(\Omega_V \tau_{12}) + i(\frac{\delta_0}{2\hbar} + i\Delta\gamma)\times$$
$$\times \left[\frac{\sin(\Omega_H \tau_{12})}{\Omega_H} - \frac{\sin(\Omega_V \tau_{12})}{\Omega_V} \right] |^2 \qquad (47)$$

Figure 44 depicts one of such series measured at $B = 6$ T. One can see the qualitative and quantitative agreement between the theoretical dependence and the experimental data in the dynamic range of signal of three orders of magnitude.

The PE decay kinetics obtained at $B = 1 - 3$ T in HH→H geometry and at $B > 1$ T in VV→V geometry demonstrate non-trivial behavior characterized by aperiodic signal oscillation. However, the presented model correctly describes the measurement data, as shown in figure 43(b). To get a clearer picture of the processes taking place, we have considered in detail a simplified case with a negligible value of the exchange interaction [190]. Next, we present the result of the analysis for the aperiodic regime.

5.7 Nonoscillatory regime

Let us consider the aperiodic behavior of the system in more detail, simplifying the initial problem. First, let us assume $\delta_0 = 0$. Second, let us show that, using linearly polarized excitation, the problem of the dynamics of a five-level system can be reduced to the problem of a three-level system. In order to do this, we have to change from the basis of excitonic states $\{0; +1; -1; +2; -2\}$ to the basis of linear states $\{0; H1; V1; H2; V2\}$:

$$|H1\rangle = \tfrac{|+1\rangle + |-1\rangle}{\sqrt{2}}, \quad |H2\rangle = \tfrac{|+2\rangle + |-2\rangle}{\sqrt{2}},$$

$$|V1\rangle = \tfrac{|+1\rangle - |-1\rangle}{\sqrt{2}}, \quad |V2\rangle = \tfrac{|+2\rangle - |-2\rangle}{\sqrt{2}}. \tag{48}$$

The Hamiltonian of the system has the following form in this basis:

$$\hat{H}_{lin} = \begin{pmatrix} 0 & f_H^* e^{i\omega t} & i f_V^* e^{i\omega t} & 0 & 0 \\ f_H e^{-i\omega t} & \hbar\omega_0 & 0 & \hbar\Omega_{H0} & 0 \\ -i f_V e^{-i\omega t} & 0 & \hbar\omega_0 & 0 & \hbar\Omega_{V0} \\ 0 & \hbar\Omega_{H0} & 0 & \hbar\omega_0 & 0 \\ 0 & 0 & \hbar\Omega_{V0} & 0 & \hbar\omega_0 \end{pmatrix}, \tag{49}$$

where $f_{H,V}(t) = -e^{i\omega t} \int \mathrm{d}(\boldsymbol{r}) E_{H,V}(\boldsymbol{r},t) d^3 r$, $E_H = \frac{E_+ + E_-}{\sqrt{2}}$, $E_V = \frac{i(E_+ - E_-)}{\sqrt{2}}$. It can be shown that states $|H1\rangle, |V1\rangle$ will experience phenomenological dephasing at the rate of bright states γ_b, while states $|H2\rangle, |V2\rangle$ will decay with the rate γ_d. If the exciting light is linearly polarized along the direction H ($E_V = 0$), a three-level subsystem can be selected, the dynamics of which will be isolated from the other states. The diagram of the states in both bases, as well as the three-level subsystem is shown in figure 45. The Hamiltonian of the subsystem in the basis $\{0; H1; H2\}$ has the form:

$$\hat{H}_H = \begin{pmatrix} 0 & f_H^* e^{i\omega t} & 0 \\ f_H e^{-i\omega t} & \hbar\omega_0 & \hbar\Omega_{H0} \\ 0 & \hbar\Omega_{H0} & \hbar\omega_0 \end{pmatrix}. \tag{50}$$

Therefore, the evolution of the system in the PE protocol in the geometries HH→H and VV→V can be found by solving the Lindblad equation (39) for the three-level system. To calculate the PE signal, we only need to determine the
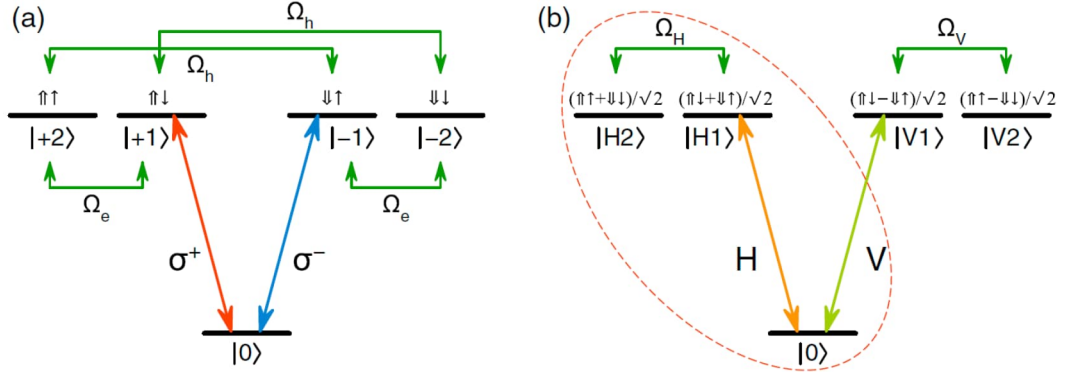
Figure 45: Diagram of exciton states in the basis $\{0; +1; -1; +2; -2\}$ (a) and in the linear basis $\{0; H1; V1; H2; V2\}$ (b). Green arrows indicate Larmor precession of electron and hole spins in exciton, vertical arrows illustrate allowed optical transitions. Dashed oval indicates three-level subsystem.

evolution of the density matrix elements $\rho_{01} = \rho_{10}^*$ and $\rho_{02} = \rho_{20}^*$. Let's assume that the system is initially in the ground state and ρ has a only non-zero element $\rho_{00} = 1$. For clarity we consider the first pulse with the area $\Theta = \frac{2}{\hbar}|f_H t_p| = \pi/2$, and the second pulse with the area π. Then the action of the first $\pi/2$-pulse leads to change of the elements $\rho_{01}(0) = -\frac{i}{2}$, $\rho_{02}(0) = 0$. The second π-pulse inverts the system $\rho_{01}(\tau_{12} + 0) = \rho_{01}(\tau_{12})^* + C_1$, $\rho_{02}(\tau_{12} + 0) = C_2$, where $\rho_{0j}(\tau_{12})$ and $\rho_{0j}(\tau_{12} + 0)$ denote the elements ρ before and after the action of the pulse, and C_1 and C_2 are constants that do not contribute to the PE signal.

The evolution of the elements $\rho_{0j}(\tau_{12})$ in the interval between pulses under the action of a transverse magnetic field can be found within the rotating wave approximation by analogy with the case described in section 2.1.4. The dynamics of the transformed density matrix $\tilde{\rho}$ for a system with zero detuning ($\omega = \omega_0$) will be governed by the relaxation term Γ and the Hamiltonian:

$$\hat{H}_T = \begin{pmatrix} 0 & 0 & 0 \\ 0 & 0 & \hbar\Omega_{H0} \\ 0 & \hbar\Omega_{H0} & 0 \end{pmatrix}. \tag{51}$$

From the Lindblad equation for the $\tilde{\rho}$ matrix, one can obtain a closed system of equations:

$$\begin{cases} i\dot{\tilde{\rho}}_{01} = -\Omega_{H0}\tilde{\rho}_{02} - i\gamma_b\tilde{\rho}_{01} \\ i\dot{\tilde{\rho}}_{02} = -\Omega_{H0}\tilde{\rho}_{01} - i\gamma_d\tilde{\rho}_{02} \end{cases}. \tag{52}$$

Let us change to Bloch equation variables $u_\alpha = 2\text{Re}(\tilde{\rho}_{0\alpha})$, $v_\alpha = -2\text{Im}(\tilde{\rho}_{0\alpha})$ ($\alpha =$

$1, 2$), noting that $u_1 = v_2 = 0$ throughout the experiment:

$$\begin{cases} \dot{v}_1 = -\Omega_{H0}u_2 - \gamma_1 v_1 \\ \dot{u}_2 = \Omega_{H0}v_1 - \gamma_2 u_2 \end{cases}. \tag{53}$$

The action of the first $\pi/2$-pulse sets the initial conditions for the given system: $v_1(0) = 1$ and $u_2(0) = 0$. Then the evolution of the system during the time between pulses $t = \tau_{12}$ is determined by the solution:

$$\begin{cases} v_1(\tau_{12}) = e^{-\gamma\tau_{12}}\left(\cos(\Omega\tau_{12}) - \frac{\Delta\gamma}{\Omega}\sin(\Omega\tau_{12})\right) \\ u_2(\tau_{12}) = e^{-\gamma\tau_{12}}\frac{\Omega_{H0}}{\Omega}\sin(\Omega\tau_{12}) \end{cases}, \tag{54}$$

where $\Omega = \sqrt{\Omega_{H0}^2 - \Delta\gamma^2}$ is the effective Larmor frequency coinciding with Ω_H at $\delta_0 = 0$. The expression (54) defines the dynamics during both the interval between the pulses $t = 0..\tau_{12}$, and after the action of the second pulse $t = \tau_{12}..2\tau_{12}$. The only difference is initial conditions. Macroscopic polarization P according to section 2.1.4 is given by $P = \text{Tr}(\hat{d}\rho) = 2\text{Re}\left(d\rho_{01}(\Omega_{H0}, t)\right)$. The final expression for PE amplitude has the form:

$$P_{PE} \sim e^{-2\gamma\tau_{12}}\left|\cos(\Omega\tau_{12}) - \frac{\Delta\gamma}{\Omega}\sin(\Omega\tau_{12})\right|^2. \tag{55}$$

The solution (55) for the three-level system is consistent with the solution for the five-level system (42) at $\delta_0 = 0$. The zeros in the PE kinetics correspond to the zeros of the element $v_1(\tau_{12})$ responsible for the macroscopic polarization. The relation $\Omega_{H0}/\Delta\gamma$ determines the sign of the radical expression for Ω, and therefore one can observe oscillating behavior ($\Omega_{H0} > \Delta\gamma$), critical regime ($\Omega_{H0} = \Delta\gamma$) and the aperiodic regime ($\Omega_{H0} < \Delta\gamma$). The expression for the PE amplitude in these modes is:

$$P_{PE} \sim \begin{cases} e^{-2\gamma\tau_{12}}\left(\cos(\Omega\tau_{12}) - \frac{\Delta\gamma}{\Omega}\sin(\Omega\tau_{12})\right)^2, & \Omega_{H0} > \Delta\gamma; \\ e^{-2\gamma\tau_{12}}(1 - \Delta\gamma\tau_{12})^2, & \Omega_{H0} = \Delta\gamma; \\ e^{-2\gamma\tau_{12}}\left(\cosh(|\Omega|\tau_{12}) - \frac{\Delta\gamma}{|\Omega|}\sinh(|\Omega|\tau_{12})\right)^2, & \Omega_{H0} < \Delta\gamma. \end{cases} \tag{56}$$
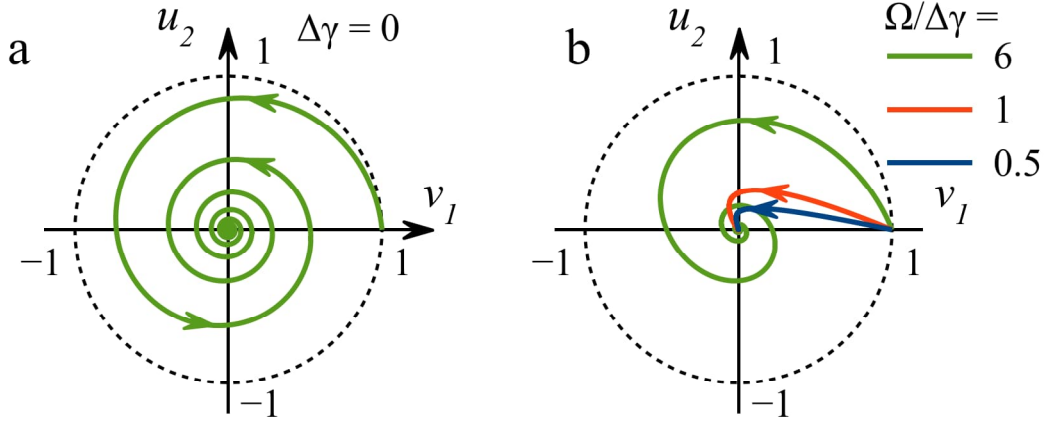
Figure 46: The evolution trajectory of elements v_1, u_2 at $\Delta\gamma = 0$ (a) and in the case of different dephasing rates (b) at $\Omega/\Delta\gamma = 6$ (green), $\Omega/\Delta\gamma = 1$ (red) and $\Omega/\Delta\gamma = 0.5$ (blue).

The behavior in these modes can be clearly demonstrated by depicting the solution (54) as an evolution trajectory on the (v_1, u_2) plane, as shown in figure 46. At $\Delta\gamma = 0$, the evolution of the system over time τ_{12} is uniform concentric spiral twisting towards the center (figure 46(a)), intersections of the u_2 axis correspond to zeros of PE signal. Figure 46(b) demonstrates how, as $\Delta\gamma$ increases, this spiral first stretches (green curve), then passes through the critical regime (red curve) to aperiodic behavior (blue curve). The aperiodic regime looks like an "infinite" fall to the center of coordinates after crossing the y-axis.

Indeed, an analysis of the experimental data shows that the aperiodic behavior of the PE decay is observed at $B \leq 1$ T in the HH→H geometry, which is caused by the difference in the dephasing rates of the bright and dark states. Note that an analogous result can be obtained for the perpendicular geometry VV→V. In this geometry, we also observe aperiodic behavior in the entire available range of magnetic fields, since the frequency Ω_V changes slightly with increasing magnetic field, in contrast to the monotonically increasing frequency Ω_H.

To demonstrate the transition through the critical regime, we measured the PE decay kinetics in the HH→H geometry in the range of low magnetic fields with a small step in the field magnitude. The measurement results are shown in figure 47. They demonstrate a smooth transition from monoexponential decay with the dephasing time of bright excitons to an oscillating regime through the aperiodic one. An additional proof of the aperiodic behavior is the presence of a distinct signal maximum measured at a long delay $\tau_{12} = 250$ ps during the B-scan. At $B \approx 0.5$ T the maximum is reached which corresponds to the critical regime.

Note that the signal at time $\tau_{12} = 150$ ps increases by about an order of magnitude when the field $B \approx 0.5$ T is applied. At the same time, according to the solution of the simplified model (46) [136], which does not take into account the difference in dephasing rates, the kinetics should always be limited from above by the exponential decay curve at zero field. Experimental observation of an increase in the amplitude, as well as decay time at large delays, clearly demonstrates the manifestation of the coherent dynamics of long-lived dark excitons. The simple model, whose approximation is shown in green in figure 47 (b), cannot adequately describe the dynamics at large delays. The consideration of different dephasing rates provides a good approximation of the experimental data using the expression 55. It can be shown that in the aperiodic regime the signal tends to monoexponential decay with the dark exciton dephasing time γ_d at large τ_{12} [190]. An analysis of the decay kinetics at $B = 0.4$ T provides a value for dark exciton dephasing time $T_2^d = 250 \pm 30$ ps, which is more than eight times the dephasing time of bright excitons. We attribute this large difference to the absence of a radiative recombination channel for dark excitons, which limits the coherent dynamics of bright excitons. Thus, we have shown that the application of the spin-dependent PE protocol for an ensemble of excitons can be used to increase the optical coherence time of the system.

5.8 Larmor precession in photon echo

Under the condition $\Omega_{H0} = \Omega_{V0}$, the decay kinetics in collinear geometries should be the same, but in figure 41 we clearly see the difference between the measurements in the HH→H and VV geometries →V. This fact indicates the presence of both electron and hole spin precession occurring during the spin-dependent PE experiment. Therefore, to obtain more complete information about the spin dynamics of an electron and a hole in an exciton, it is necessary to carry out measurements in both geometries.

The considered model (42) allows us to approximate the data from figure 41, which provides information about the Larmor precession frequencies of the electron ω_e and hole spin ω_h in the exciton. The analysis results are shown in figure 48. The frequency ω_e linearly depends on the magnetic field. From the approximation of the data by the expression $\omega_e = \frac{g_{e,\perp}\mu_B B}{\hbar}$, we obtain the value for the electron
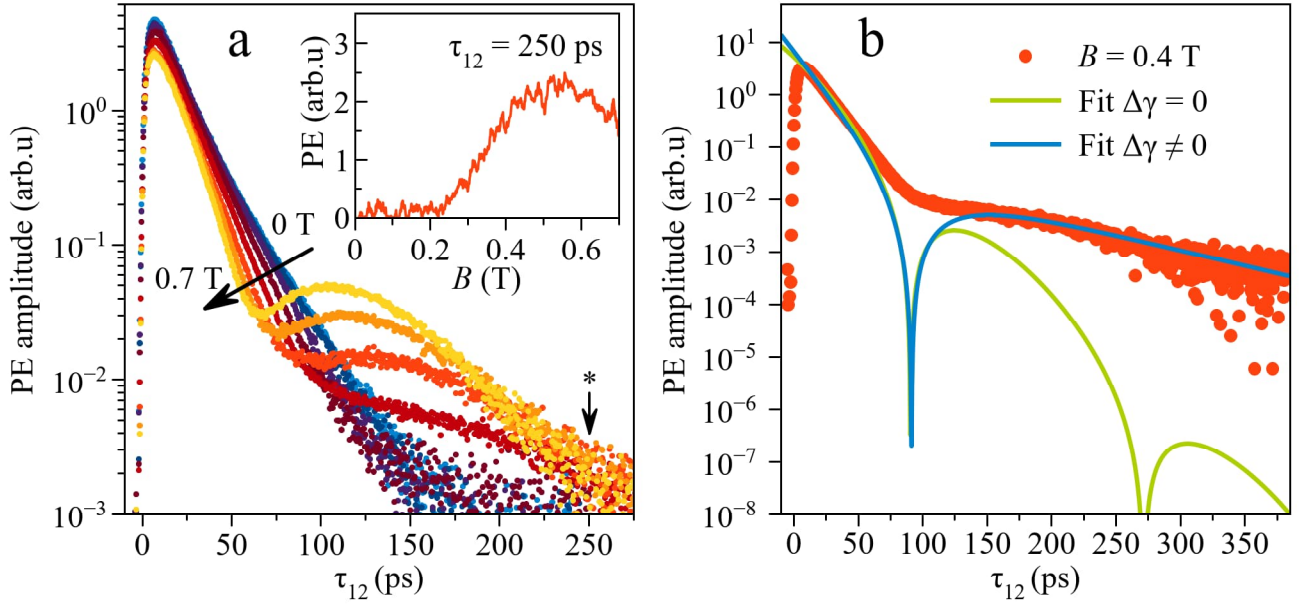
Figure 47: (a) PE amplitude decay kinetics measured at a transverse magnetic field $B = 0 - 0.7$ T in the geometry HH→H. A star denotes time delay at which smooth B-scan was measured. Inset shows PE amplitude at $\tau_{12} = 250$ ps as a function of a magnetic field B.(b) Experimentally measured kinetics at $B = 0.4$ T (red dots) and its approximation with $\Delta\gamma = 0$ (green) and $\Delta\gamma \neq 0$ (blue).
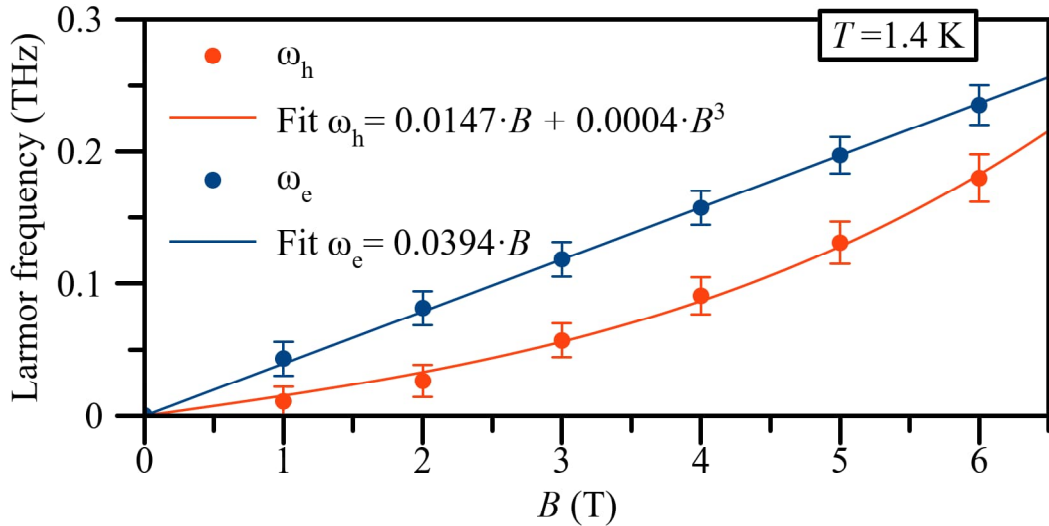
Figure 48: Electron (blue) and heavy hole (red) Larmor precession frequencies, extracted from spin-dependent PE decay kinetics, as a function of applied magnetic field. Corresponding linear and cubic fit are plotted by solid lines.

g factor in the well plane $|g_{e,\perp}| = 0.44 \pm 0.05$. This value coincides with that for bulk GaAs [210, 213, 214] and is close to the values for thin InGaAs/GaAs QWs [215, 216]. The obtained value indicates that the electronic wave function is mainly distributed inside the barriers of the GaAs well, which is expected in the case of a low percentage of indium in the thin well layer.

The measurements also reveal the presence of hole spin precession. Moreover, the frequency ω_h depends non-linearly on the applied magnetic field magnitude. The corresponding in-plane hole g factor becomes comparable with that for an electron at $B = 6$ T and reaches the maximum value $|g_{h,\perp}| \approx 0.3$. The hole g-factor is known to be highly anisotropic in GaAs-based nanostructures [217] due to the hole sub-band splitting with spin projections $\pm 3/2$ and $\pm 1/2$ due to the lowering of dimensionality. Therefore, heavy holes do not experience Zeeman splitting in a transverse field due to the zero matrix element of the operators $J_x = J_y = 0$ [143, 215, 216]. The non-Zeeman interaction of heavy holes is admissible by the symmetry of the Luttinger Hamiltonian and is described by the cubic terms J_x^3, J_y^3 and the Luttinger coefficient q [217, 218]. The latter is usually also considered a small correction or is set to zero for simplicity. Despite this, there are several studies in the literature about the detection of a non-zero value of $g_{h,\perp}$, which was mainly associated either with the coefficient q [219] or the presence of anisotropic perturbations [130, 131, 217].

The obtained value of $|g_{h,\perp}|$ is in the range of reported values for InGaAs/GaAs QDs $0.15 - 0.6$, in which mechanical stresses and admixture of light-hole states take place [220, 221]. The recently reported dependence of the in-plane hole g factor on the magnitude of the applied magnetic field was a consequence of the mixing of the states of a heavy and light hole [222]. In addition, the third order perturbation theory predicts a contribution to $|g_{h,\perp}|$ [218]. The experimental points are well approximated by the cubic dependence shown in figure 48, however, the obtained coefficient of the cubic term is three orders of magnitude greater than the expected value, determined by the heavy-hole–light-hole splitting. In our case, all the above mechanisms can take place, and additional measurements are needed to identify individual contributions, as, for example, were carried out in a work on spin-dependent echo in CdTe/(Cd,Mg)Te QWs and (In,Ga) As/GaAs QDs [130, 131].

Note that in contrast to other techniques for studying spin coherent dynamics the spin-dependent photon echo has an advantage of the capability to measure the

electron and hole Larmor precession frequencies in the range of low magnetic fields. It is since the signal experiences beats at the sum or difference frequency, depending on the polarization geometry. Spin-dependent PE measurements provide us only the absolute value of the g factors, and from the data we see that both of them have same sign. Since electron g-factor was determined to have a negative sign [215, 216], the hole g factor is also negative.

Zeros of the PE signal are expected when there is no polarization in optically active states ($\rho_{01} = \rho_{02} = 0$) at the moment of arrival of the second exciting pulse $t = \tau_{12}$. The data shows (figure 41) that the oscillating decay does not reach zero. At least two mechanisms can lead to this behaviour. The first is related to the exchange interaction responsible for the splitting of bright and dark exciton states in a zero external field. From the approximation of the data shown in figure 43 we can provide an upper estimate for $\delta_0 \leq 10$ µeV. The second mechanism is associated with the presence of an inhomogeneous spread of g-factors, which can reach one third of the g-factor of a heavy hole in InGaAs/GaAs QDs [223]. The inhomogeneity leads to smoothing of the oscillations in the vicinity of PE zeros and to the contrast decrease at a high field magnitude and long time delay. The spread can be included in the model by convolution of the expression for the PE amplitude with the Gaussian distribution of the heavy hole g factor $P_\Sigma \sim \int P e^{-\frac{(g_h - g_{h0})^2}{2\Delta g_h^2}} dg_h$, where P_Σ is the integrated PE amplitude, P is the PE amplitude from the sub-ensemble with g_h, g_{h0} – the average value of the g-factor and Δg_h is the spread of the g-factor. Figure 43 shows the best approximation with a spread of $\frac{\Delta g_h}{g_h} = 0.03$. Since in the presented experiments both of these mechanisms manifest themselves in a similar way, we can only give upper estimations for the quantities δ_0 and $\frac{\Delta g_h}{g_h}$.

5.9   Conclusion

In this chapter, we have demonstrated the experimental observation of the oscillating behavior of spin-dependent two-pulse photon echo from an exciton ensemble in a narrow (In,Ga)As/GaAs QW subject to external transverse magnetic field in the Voigt geometry. The oscillations are due to the Larmor precession of the electron and hole spin forming the exciton. The presence of long-lived dark exciton states led to the observation of a new aperiodic regime of the spin-dependent PE signal. In this regime the dephasing time can be increased by more than 8 times due

to the mixing of bright and dark exciton states. The developed theoretical model correctly describes all the main features of the coherent dynamics and makes it possible to obtain a rich set of information about the dephasing time of bright and dark excitons, the electron and hole g factors, and the exchange interaction constant. The high accuracy of the method in relatively low magnetic fields made it possible not only to detect a nonzero in-plane hole g factor, but also to reveal the nonlinear dependence of the hole Larmor precession on the applied transverse magnetic field.

Conclusion

The dissertation demonstrates the successful application of the picosecond photon echo technique and its further development for a comprehensive experimental study of the coherent optical dynamics of excitons and trions in semiconductor quantum wells in the infrared and ultraviolet spectral ranges. The main results of the dissertation are the following:

1. We have shown how the technique of two- and three-pulse photon echo using narrow-spectrum laser pulses, can be used to comprehensively study the picosecond coherent dynamics of excitons and trions in a 5 ZnO/(Zn,Mg)O multiple quantum well structure even at the presence of a large inhomogeneous broadening. The method we use clearly demonstrates the possibility of separation of various contributions to the phase and energy relaxation of an ensemble of quasiparticles. The difference of the coherent dynamics of excitons and trions of both types A and B was experimentally shown. The T_A trions were found to be the most long-lived states, whose time T_2 is in the range from 8 to 60 ps, and the time T_1 vary from 28 to 102 ps. The main dephasing channel of T_A trions at $T = 1.5$ K is not associated with energy relaxation, but is determined by pure dephasing. Temperature measurements made it possible to distinguish the contribution to the T_A trion dephasing associated with acoustic phonons scattering. We have succeeded in demonstrating a strong decrease of dephasing and energy relaxation rates with rising T_A trion localization degree at low temperature. We attribute this behavior to a less pronounced elastic scattering on the roughness of the quantum well interface and to decreased nonradiative energy relaxation inside the inhomogeneous trion ensemble.

2. The dissertation presents the first experimental investigation of the picosecond coherent dynamics of excitons in a multiple-quantum-well structure with a hundred (In,Ga)N/GaN quantum wells in ultraviolet spectral region revealed by the photon echo. The work has shown that in such structures localized excitons retain optical coherence at times of hundreds of picoseconds, and the energy relaxation time T_1 reaches 1 ns with increasing localization. Temperature studies have revealed the non-linear increase of the exciton dephasing rate. The obtained experimental results indicate a strong quantum dot-like localization of excitons on the QW potential fluctuations.

3. We have experimentally demonstrated for the first time the oscillating behavior of the spin-dependent two-pulse photon echo from excitons in a narrow (In,Ga)As/GaAs QW subject to an external transverse magnetic field in the Voigt geometry. According to the theoretical model describing the experimental data the observed oscillations are related to the Larmor precession of the spin of an electron and a hole forming an exciton. The observation became possible only due to the selection of a high-quality structure in which the exciton dephasing time is long enough to make a complete oscillation cycle. We consider the successful implementation of the protocol of spin-dependent PE on an exciton ensemble as a demonstration of manipulation of optical coherence by an external magnetic field. The presence of long-lived dark exciton states led to the observation of a new aperiodic regime of the spin-dependent photon echo. In this regime the dephasing time can be increased from 30 up to 250 ps by mixing bright and dark exciton states. The developed theoretical model made it possible to correctly describe all the main features of the dynamics and obtain a rich set of information on the dephasing time of bright and dark excitons, the electron and hole g factors, and the exchange interaction constant. The high accuracy of the method in the range of low magnetic fields made it possible not only to detect a nonzero in-plane hole g factor, but also to reveal the nonlinear dependence of the hole Larmor precession on the applied transverse magnetic field.

Acknowledgments

for their support during the writing of the dissertation.

Appendix A. Additional theoretical aspects

A.1   Density matrix formalism

To describe quantum systems, as a rule, the formalism of wave functions of states and their expansion in terms of basis functions of stationary states are used. In the case of quantum mixtures, a more convenient approach is the description using the density matrix, which formalism is described in detail in the monographs [224, 225]. Let us consider a system in a pure quantum state, for which the wave function Ψ can be written explicitly, taking into account all phase factors. For such a system, the observed value A is determined by quantum expectation value according to the rule:

$$\langle A \rangle = \langle \Psi | \hat{A} | \Psi \rangle , \qquad (57)$$

where $\hat{A}$ is the Hermitian operator of the physical quantity A. Choosing an orthonormal basis $|n\rangle$, one can write the expansion in the basis of the wave function $|\Psi\rangle = \sum_n c_n |n\rangle$ and substitute it into the expression 57. Then

$$\langle A \rangle = \langle \sum_m c_m^* m | \hat{A} | \sum_n c_n n \rangle = \sum_{n,m} c_m^* c_n \langle m | \hat{A} | n \rangle = \sum_{n,m} c_m^* c_n A_{mn} \qquad (58)$$

Let us introduce a matrix ρ, the elements of which are determined by the coefficients of the expansion of Ψ in terms of the basis, paying attention to the order of the coefficients, $\rho = \sum_{n,m} c_n c_m^* |n\rangle \langle m| = |\Psi\rangle \langle \Psi|$). In a result we obtain:

$$\langle A \rangle = \sum_{n,m} \rho_{nm} A_{mn} = \sum_n (\rho A)_{nn} = \mathrm{Tr}(\rho A) = \mathrm{Tr}(A\rho) \qquad (59)$$

We see that to calculate the expectation value of the $\langle A \rangle$, it suffices to know the density matrix ρ and the matrix of the physical quantity operator $\hat{A}$. Note that the diagonal terms of ρ_{nn} are equal to the population of the corresponding state, as can be seen from the definition of ρ. In the case of a pure state of the system, the calculation of the expectation value using the density matrix is equivalent to the calculation in terms of the wave function Ψ. However, the situation changes significantly when passing from a pure state to a mixed state, which cannot be expanded into a linear combination in $|n\rangle$ basis states, since the coefficients c_n are

generally unknown.

Consider an ensemble of N completely identical closed systems. Let assume, that for each such system the wave function Ψ could be determined, but it is impossible to know it. Suppose we only know the probability distribution ω_α ($\sum_\alpha \omega_\alpha = 1$) for the system to be in state ψ_α. This distribution is the same for all systems due to the identity of the systems. Then among them there will be approximately $N\omega_\alpha$ systems in the ψ_α state for each α (the probability is the statistical weight of each expectation value). We will focus on the average value of $\langle A \rangle_\alpha$ over the ensemble, that is, averaged over all N systems.

$$\langle A \rangle_\alpha = \frac{1}{N} \sum_\alpha N\omega_\alpha \langle A \rangle_{\Psi_\alpha} \tag{60}$$

Substitute expression $\langle A \rangle_{\Psi_\alpha} = \sum_{n,m} c_m^{\alpha *} c_n^\alpha A_{mn}$ into (60), reducing N:

$$\langle A \rangle_\alpha = \sum_{\alpha,n,m} \omega_\alpha c_m^{\alpha *} c_n^\alpha A_{mn} = \sum_{n,m} A_{mn} \underbrace{\sum_\alpha \omega_\alpha c_m^{\alpha *} c_n^\alpha}_{=\widetilde{\rho}_{nm}} = \sum_{n,m} A_{mn} \widetilde{\rho}_{nm} = \mathrm{Tr}(A\widetilde{\rho}) \tag{61}$$

Thus, we can compose a density matrix for the case when the exact state Ψ is unknown, but there is only a set of possible states $\{\Psi\}_\alpha$ and the probabilities to find a system in them $\{\omega\}_\alpha$. Moreover, the problems of one system in a mixed state or of an ensemble of copies of this system, each of which is in a certain but unknown state with the probability distribution ω_α, are equivalent.

A.2 Evolution operator and the von Neumann equation

The Schrödinger equation for the wave function ψ determines the time evolution of a quantum system. An alternative way is to introduce the an evolution operator $U(t)$ [224], which transforms the initial state $\psi(0)$ into the state $\psi(t)$:

$$\psi(t) = U(t)\psi(0) \tag{62}$$

In this case, the Schrödinger equation reduces to the operator equation:

$$i\hbar \frac{\partial U(t)}{\partial t} = H(t)U(t), \; U(0) = I \tag{63}$$

If Hamiltonian H does not explicitly depend on time, the solution of the equation (62) has the form:

$$U(t) = e^{-(i/\hbar)Ht} \tag{64}$$

Thus, the evolution of the system can be determined either by solving the Schrödinger equation or by finding the evolution operator $U(t)$.

Let us now consider an ensemble of quantum mechanical systems described by the density matrix according to (61):

$$\rho = \sum_\alpha \omega_\alpha \left| \psi_\alpha \right\rangle \left\langle \psi_\alpha \right|. \tag{65}$$

The functions ψ_α evolve according to the expression (62), so the evolution operator $U(t)$ determines also the temporal evolution of density matrix:

$$\rho(t) = U(t)\rho(0)U^*(t) \tag{66}$$

If the Hamiltonian does not explicitly depend on time, then according to (64)

$$\rho(t) = e^{-(i/\hbar)Ht}\rho(0)e^{(i/\hbar)Ht} \tag{67}$$

By differentiating (66), one can get the von Neumann equation:

$$i\hbar\frac{\partial \rho(t)}{\partial t} = [H(t), \rho(t)]. \tag{68}$$

We have shown that the evolution of the density matrix can be determined either by solving the von Neumann equation (68) or by finding the explicit form of the evolution operator $U(t)$ and substituting it into the equation (66).

Abbreviation list

QW - quantum well

MQW - multiple quantum well

QD - quantum dot

FWM - four-wave mixing

PE - photon echo

SPE - stimulated photon echo

PL - photoluminescence

LH - light hole

HH - heavy hole

TR-FWM - time-resolved four-wave mixing

TI-FWM - time-integrated four-wave mixing

FWHM - full width at half maximum

HWHM - half width at half maximum

References

1. *Frenkel J.* On the transformation of light into heat in solids. I // Phys. Rev. — 1931. — Vol. 37, no. 1. — P. 17–44.

2. *Frenkel J.* On the Transformation of Light into Heat in Solids. II // Phys. Rev. — 1931. — May. — Vol. 37, no. 10. — P. 1276–1294.

3. *Wannier G. H.* The structure of electronic excitation levels in insulating crystals // Phys. Rev. — 1937. — Vol. 52, no. 3. — P. 191–197.

4. *Mott N. F.*, *Littleton M. J.* Conduction in polar crystals. I. Electrolytic conduction in solid salts // Trans. Faraday Soc. — 1938. — Vol. 34, no. 9. — P. 485–499.

5. *Mott N. F.* Conduction in polar crystals. II. The conduction band and ultraviolet absorption of alkali-halide crystals // Trans. Faraday Soc. — 1938. — Vol. 34. — P. 500–506.

6. *Gross E.*, *Karryev N.* Optical spectrum of an exciton // The Proceedings of the USSR Academy of Sciences. — 1952. — Vol. 84. — P. 471.

7. *Abiyasa A.* [et al.]. Theoretical Investigation of Excitonic Gain in ZnO–$Mg_xZn_{1-x}O$ Strained Quantum Wells // IEEE J. Quantum Electron. — 2006. — May. — Vol. 42, no. 5. — P. 455–463.

8. *Khramtsov E. S.* [et al.]. Radiative decay rate of excitons in square quantum wells: Microscopic modeling and experiment // J. Appl. Phys. — 2016. — May. — Vol. 119, no. 18. — P. 184301.

9. *Ivchenko, Eugenius L.* Optical Spectroscopy of Semiconductor Nanostructures. — Harrow, UK : Alpha Science International, Ltd, 2005.

10. *Claus Klingshirn.* Semiconductor Optics. — Heidelberg : Springer-Verlag Heidelberg, 2005.

11. *Kärtner F. X.*, *Ippen E. P.*, *Cundiff S. T.* Femtosecond Laser Development // Femtosecond Opt. Freq. Comb Princ. Oper. Appl. — Boston : Kluwer Academic Publishers. — P. 54–77.

12. *Sibbett W.*, *Lagatsky A. A.*, *Brown C. T. A.* The development and application of femtosecond laser systems // Opt. Express. — 2012. — Mar. — Vol. 20, no. 7. — P. 6989.

13. *Hegarty J.*, *Sturge M. D.* Studies of exciton localization in quantum-well structures by nonlinear-optical techniques // J. Opt. Soc. Am. B. — 1985. — July. — Vol. 2, no. 7. — P. 1143.

14. *Hegarty J.* Excitons in GaAs Quantum Wells: Interface Disorder and Mobility //. — 1986. — P. 280–288.

15. *Chemla D. S.*, *Miller D. A. B.* Room-temperature excitonic nonlinear-optical effects in semiconductor quantum-well structures // J. Opt. Soc. Am. B. — 1985. — July. — Vol. 2, no. 7. — P. 1155.

16. *Peyghambarian N.*, *Gibbs H. M.* Optical nonlinearity, bistability, and signal processing in semiconductors // J. Opt. Soc. Am. B. — 1985. — July. — Vol. 2, no. 7. — P. 1215.

17. *Shen Y.* Basic considerations of four-wave mixing and dynamic gratings // IEEE J. Quantum Electron. — 1986. — Aug. — Vol. 22, no. 8. — P. 1196–1203.

18. *Shah J.* Ultrafast Spectroscopy of Semiconductors and Semiconductor Nanostructures. Vol. 115. — Berlin, Heidelberg : Springer Berlin Heidelberg, 1996. — (Springer Series in Solid-State Sciences).

19. *Armstrong J. A.* [et al.]. Interactions between Light Waves in a Nonlinear Dielectric // Phys. Rev. — 1962. — Sept. — Vol. 127, no. 6. — P. 1918–1939.

20. *Shen I. R.* The Principles of Nonlinear Optics / ed. by S. A. Akhmanova. — Moscow : Nauka, 1989.

21. *Kopvillem U. K.*, *R. N. V.* Light echo in paramagnetic crystals // Physics of metals and metal science. — 1963. — Vol. 15, no. 2. — P. 313.

22. *Kurnit N. A.*, *Abella I. D.*, *Hartmann S. R.* Observation of a photon echo // Phys. Rev. Lett. — 1964. — Vol. 13, no. 19. — P. 567–568.

23. *Cundiff S. T.* Coherent spectroscopy of semiconductors // Opt. Express. — Washington, D.C., 2008. — Mar. — Vol. 16, no. 7. — P. 4639.

24. *Poltavtsev S. V.* [et al.]. Photon Echo from Localized Excitons in Semiconductor Nanostructures // Phys. Solid State. — 2018. — Aug. — Vol. 60, no. 8. — P. 1635–1644.

25. *Hellwarth R. W.* Generation of time-reversed wave fronts by nonlinear refraction // J. Opt. Soc. Am. — 1977. — Jan. — Vol. 67, no. 1. — P. 1.

26. *Cronin-Golomb M.* [et al.]. Theory and Applications of Four-Wave Mixing in Photorefractive Media // IEEE J. Quantum Electron. — 1984. — Vol. 20, no. 1. — P. 12–30.

27. *Zel'dovich B. Y., Pilipetsky N. F., Shkunov V. V.* OPC in Four-Wave Mixing // Princ. Phase Conjug. — 1985. — P. 144–170.

28. *He G. S.* Optical phase conjugation: Principles, techniques, and applications // Prog. Quantum Electron. — 2002. — Vol. 26, no. 3. — P. 131–191.

29. *Fleuret J.* Optical computing units using four-wave mixing and amplitude coding // Appl. Opt. — 1984. — Vol. 23, no. 10. — P. 1609.

30. *Samartsev V. V., Zuikov V. A., Nefed'ev L. A.* Optical memory based on long-lived photon echo (review) // J. Appl. Spectrosc. — 1993. — Nov. — Vol. 59, no. 5/6. — P. 766–791.

31. *Samartsev V. V.* Coherent optical spectroscopy of promising materials for solid-state optical processors // Laser Phys. — 2010. — Feb. — Vol. 20, no. 2. — P. 383–446.

32. *Manykin E., Samartsev V.* Optical echo-spectroscopy / ed. by S. Akhmanov. — Moscow : Nauka, 1984.

33. *Tittel W.* [et al.]. Photon-echo quantum memory in solid state systems // Laser Photon. Rev. — 2010. — May. — Vol. 4, no. 2. — P. 244–267.

34. *Moiseev S. A.* Photon-echo quantum memory with complete use of natural inhomogeneous broadening // Phys. Rev. A - At. Mol. Opt. Phys. — 2011. — Vol. 83, no. 1. — P. 1–7.

35. *Minnegaliev M. M.* [et al.]. Quantum memory in the revival of silenced echo scheme in an optical resonator // Quantum Electron. — 2018. — Oct. — Vol. 48, no. 10. — P. 894–897.

36. *Buluta I., Ashhab S., Nori F.* Natural and artificial atoms for quantum computation // Reports Prog. Phys. — 2011. — Oct. — Vol. 74, no. 10. — P. 104401.

37. *Loss D., DiVincenzo D. P.* Quantum computation with quantum dots // Phys. Rev. A. — 1998. — Jan. — Vol. 57, no. 1. — P. 120–126.

38. *Puri S.*, *McMahon P. L.*, *Yamamoto Y.* Universal logic gates for quantum-dot electron-spin qubits using trapped quantum-well exciton polaritons // Phys. Rev. B. — 2017. — Mar. — Vol. 95, no. 12. — P. 125410.

39. *Widhalm A.* [et al.]. Ultrafast electric phase control of a single exciton qubit // Appl. Phys. Lett. — 2018. — Vol. 112, no. 11.

40. *Henneberger F.*, *Benson O.* Semiconductor quantum bits. — Singapore : Pan Stanford Publishing Pte. Ltd., 2008.

41. *Puls J.*, *Sadofev S.*, *Henneberger F.* Trions in ZnO quantum wells and verification of the valence band ordering // Phys. Rev. B. — 2012. — Jan. — Vol. 85, no. 4. — P. 041307.

42. *Kim J.* [et al.]. Charged carrier spin dynamics in ZnO quantum wells and epilayers // Phys. Rev. B. — 2016. — Jan. — Vol. 93, no. 4. — P. 045306.

43. *Declerck G.*, *Klaassen F.* Physics of Quantum Well Devices. Vol. 7. — Dordrecht : Kluwer Academic Publishers, 2002. — (Solid-State Science and Technology Library).

44. *Esmaeil Zadeh I.* [et al.]. Superconducting nanowire single-photon detectors: A perspective on evolution, state-of-the-art, future developments, and applications // Appl. Phys. Lett. — 2021. — Vol. 118, no. 19.

45. *Vorobyev L.* [et al.]. Optical properties of nanostructures / ed. by E. L. Ivchenko, L. Vorobyev. — Saint Petersburg : Nauka, 2001.

46. *Gaponenko S.* [et al.]. Optics of nanostructures. — 2005. — P. 326.

47. *Harrison P.*, *Valavanis A.* Quantum Wells, Wires and Dots. — Chichester, UK : John Wiley & Sons, Ltd, 05/2016.

48. Optical Properties of Semiconductor Nanostructures / ed. by M. L. Sadowski, M. Potemski, M. Grynberg. — Dordrecht : Springer Netherlands, 2000.

49. *Aliev G. N.* [et al.]. High-temperature efficiency of exciton-polariton processes in semiconductors and 2D systems // Int. Conf. Excit. Process. Condens. Matter. Vol. 2362 / ed. by J. Singh. — 02/1995. — P. 561–568.

50. *Belov P.* Energy spectrum of excitons in square quantum wells // Phys. E Low-dimensional Syst. Nanostructures. — 2019. — Aug. — Vol. 112. — P. 96–108.

51. *Belov P. A.*, *Yakovlev S. L.* Energy Levels of Excitons in Square Quantum Wells // Recent Prog. Few-Body Phys. — 2020. — P. 29–33.

52. *Hopfield J. J.*, *Thomas D. G.* Fine structure and magneto-optic effects in the exciton spectrum of cadmium sulfide // Phys. Rev. — 1961. — Vol. 122, no. 1. — P. 35–52.

53. *Andreani L. C.*, *Tassone F.*, *Bassani F.* Radiative lifetime of free excitons in quantum wells // Solid State Commun. — 1991. — Mar. — Vol. 77, no. 9. — P. 641–645.

54. *Citrin D. S.* Radiative lifetimes of excitons in quantum wells: Localization and phase-coherence effects // Phys. Rev. B. — 1993. — Feb. — Vol. 47, no. 7. — P. 3832–3841.

55. *Pelant I.*, *Valenta J.* Luminescence Spectroscopy of Semiconductors. — Oxford : Oxford University PressOxford, 02/2012.

56. *Dang G. T.*, *Kanbe H.*, *Taniwaki M.* Photoluminescence of an $Al_{0.5}Ga_{0.5}As$/GaAs multiple quantum well in the temperature range from 5 to 400 K // J. Appl. Phys. — 2009. — Vol. 106, no. 9.

57. *Jiang D. S.*, *Jung H.*, *Ploog K.* Temperature dependence of photoluminescence from GaAs single and multiple quantum-well heterostructures grown by molecular-beam epitaxy // J. Appl. Phys. — 1988. — Vol. 64, no. 3. — P. 1371–1377.

58. *Bayer M.* [et al.]. Fine structure of neutral and charged excitons in self-assembled In(Ga)As/(Al)GaAs quantum dots // Phys. Rev. B. — 2002. — May. — Vol. 65, no. 19. — P. 195315.

59. *Brunner K.* [et al.]. Sharp-line photoluminescence of excitons localized at GaAs/AlGaAs quantum well inhomogeneities // Appl. Phys. Lett. — 1994. — Vol. 64, no. 24. — P. 3320–3322.

60. *Brunner K.* [et al.]. Sharp-line photoluminescence and two-photon absorption of zero-dimensional biexcitons in a GaAs/AlGaAs structure // Phys. Rev. Lett. — 1994. — Vol. 73, no. 8. — P. 1138–1141.

61. *Kawai H.*, *Kaneko K.*, *Watanabe N.* Photoluminescence of AlGaAs/GaAs quantum wells grown by metalorganic chemical vapor deposition // J. Appl. Phys. — 1984. — Vol. 56, no. 2. — P. 463–467.

62. *Jung H., Fischer A., Ploog K.* Photoluminescence of $Al_xGa_{1-x}As$/GaAs quantum well heterostructures grown by molecular beam epitaxy - II. Intrinsic free-exciton nature of quantum well luminescence // Appl. Phys. A Solids Surfaces. — 1984. — Vol. 33, no. 2. — P. 97–105.

63. *Devine R. L.* Photoluminescence characterisation of InGaAs/GaAs quantum well structures // Semicond. Sci. Technol. — 1988. — Vol. 3, no. 12. — P. 1171–1176.

64. *Sekiguchi Y., Miyazawa S. I., Mizutani N.* Photoluminescence from GaAs/AlGaAs quantum wells grown at 350°C by conventional molecular beam epitaxy // Jpn. J. Appl. Phys. — 1991. — Vol. 30, 10A. — P. L1726–L1728.

65. *Vinattieri A.* [et al.]. Picosecond dynamics of resonantly-excited excitons in GaAs quantum wells // Solid State Commun. — 1993. — Vol. 88, no. 3. — P. 189–193.

66. *Damen T. C.* [et al.]. Dynamics of exciton formation and relaxation in GaAs quantum wells // Phys. Rev. B. — 1990. — Oct. — Vol. 42, no. 12. — P. 7434–7438.

67. *Trifonov A. V.* [et al.]. Nanosecond Spin Coherence Time of Nonradiative Excitons in GaAs/AlGaAs Quantum Wells // Phys. Rev. Lett. — 2019. — Apr. — Vol. 122, no. 14. — P. 147401.

68. *Eccleston R.* [et al.]. Exciton dynamics in a GaAs quantum well // Phys. Rev. B. — 1991. — July. — Vol. 44, no. 3. — P. 1395–1398.

69. *Blom P. W. M.* [et al.]. Selective exciton formation in thin GaAs/$Al_xGa_{1-x}As$ quantum wells // Phys. Rev. Lett. — 1993. — Dec. — Vol. 71, no. 23. — P. 3878–3881.

70. *Vinattieri A.* [et al.]. Picosecond dynamics of resonantly-excited excitons in GaAs quantum wells // Solid State Commun. — 1993. — Oct. — Vol. 88, no. 3. — P. 189–193.

71. *Deveaud B.* [et al.]. Enhanced radiative recombination of free excitons in GaAs quantum wells // Phys. Rev. Lett. — 1991. — Oct. — Vol. 67, no. 17. — P. 2355–2358.

72. *Hanamura E.* Rapid radiative decay and enhanced optical nonlinearity of excitons in a quantum well // Phys. Rev. B. — 1988. — July. — Vol. 38, no. 2. — P. 1228–1234.

73. *Feldmann J.* [et al.]. Linewidth dependence of radiative exciton lifetimes in quantum wells // Phys. Rev. Lett. — 1987. — Nov. — Vol. 59, no. 20. — P. 2337–2340.

74. *Colocci M.* [et al.]. Temperature Dependence of Exciton Lifetimes in GaAs/AlGaAs Quantum Well Structures // Europhys. Lett. — 1990. — July. — Vol. 12, no. 5. — P. 417–422.

75. *Eccleston R.* [et al.]. Density-dependent exciton radiative lifetimes in GaAs quantum wells // Phys. Rev. B. — 1992. — Vol. 45, no. 19. — P. 11403–11406.

76. *Wang H.* [et al.]. Spontaneous Emission of Excitons in GaAs Quantum Wells: The Role of Momentum Scattering // Phys. Rev. Lett. — 1995. — Apr. — Vol. 74, no. 15. — P. 3065–3068.

77. *Fox M.* Optical Properties of Solids. — New York : Oxford University Press, 2010.

78. *Benedict M. G., Trifonov E. D.* Coherent reflection as superradiation from the boundary of a resonant medium // Phys. Rev. A. — 1988. — Sept. — Vol. 38, no. 6. — P. 2854–2862.

79. *Poltavtsev S. V., Stroganov B. V.* Experimental investigation of the oscillator strength of the exciton transition in GaAs single quantum wells // Phys. Solid State. — 2010. — Sept. — Vol. 52, no. 9. — P. 1899–1905.

80. *Poltavtsev S. V.* [et al.]. Investigation of the mechanisms of exciton coherence relaxation in single GaAs/AlGaAs quantum wells by the methods of excitonic induction // Opt. Spectrosc. — 2008. — Oct. — Vol. 105, no. 4. — P. 511–516.

81. *Poltavtsev S. V.* [et al.]. Extremely low inhomogeneous broadening of exciton lines in shallow (In,Ga)As/GaAs quantum wells // Solid State Commun. — 2014. — Vol. 199. — P. 47–51.

82. *Shapochkin P. Y.* [et al.]. Excitonic Probe for Characterization of High-Quality Quantum-Well Heterostructures // Phys. Rev. Appl. — 2019. — Sept. — Vol. 12, no. 3. — P. 034034.

83. *Poltavtsev S. V., Ovsyankin V. V., Stroganov B. V.* Coherent resonant scattering and free induction decay of 2D-excitons in GaAs SQW // Phys. status solidi. — 2009. — Feb. — Vol. 6, no. 2. — P. 483–487.

84. *Chemla D.* Ultrafast Transient Nonlinear Optical Processes in Semiconductors // Nonlinear Opt. Semicond. I / ed. by E. Garmire, A. Kost. — Elsevier, 1998. — Chap. 3. P. 175–256.

85. *Schmitt-Rink S., Chemla D. S., Miller D. A.* Linear and nonlinear optical properties of semiconductor quantum wells // Adv. Phys. — 1988. — Vol. 38, no. 2. — P. 89–188.

86. *Trifonov A. V.* [et al.]. Nontrivial relaxation dynamics of excitons in high-quality InGaAs/GaAs quantum wells // Phys. Rev. B. — 2015. — Mar. — Vol. 91, no. 11. — P. 115307.

87. *Kurdyubov A. S.* [et al.]. Optical control of a dark exciton reservoir // Phys. Rev. B. — 2021. — July. — Vol. 104, no. 3. — P. 035414.

88. *Trifonov A. V.* [et al.]. Multiple-frequency quantum beats of quantum confined exciton states // Phys. Rev. B. — 2015. — Nov. — Vol. 92, no. 20. — P. 201301.

89. *Chemla D. S.* [et al.]. Room Temperature Excitonic Nonlinear Absorption and Refraction in GaAs/AIGaAs Multiple Quantum Well Structures // IEEE J. Quantum Electron. — 1984. — Vol. 20, no. 3. — P. 265–275.

90. *Miller D. A. B.* [et al.]. Degenerate four-wave mixing in room-temperature GaAs/GaAlAs multiple quantum well structures // Appl. Phys. Lett. — 1983. — June. — Vol. 42, no. 11. — P. 925–927.

91. *Lindberg M., Binder R., Koch S. W.* Theory of the semiconductor photon echo // Phys. Rev. A. — 1992. — Feb. — Vol. 45, no. 3. — P. 1865–1875.

92. *Yajima T., Taira Y.* Spatial Optical Parametric Coupling of Picosecond Light Pulses and Transverse Relaxation Effect in Resonant Media // J. Phys. Soc. Japan. — 1979. — Nov. — Vol. 47, no. 5. — P. 1620–1626.

93. *Loring R. F., Mukamel S.* Unified theory of photon echoes: The passage from inhomogeneous to homogeneous line broadening // Chem. Phys. Lett. — 1985. — Mar. — Vol. 114, no. 4. — P. 426–429.

94. *Allen L.*, *Eberly J. H.* Optical Resonance and Two-Level Atoms. — New York : John Wiley & Sons, inc, 1975.

95. *Hahn E. L.* Spin echoes // Phys. Rev. — 1950. — Vol. 80, no. 4. — P. 580–594.

96. *Steel D. G.*, *Cundiff S. T.* Photon Echoes in Disordered Semiconductor Quantum Wells // Laser Phys. — 2002. — Vol. 12, no. 8. — P. 1135–1147.

97. *Hegarty J.* [et al.]. Resonant degenerate four-wave mixing in GaAs multiquantum well structures // Appl. Phys. Lett. — 1982. — Jan. — Vol. 40, no. 2. — P. 132–134.

98. *Schultheis L.*, *Sturge M. D.*, *Hegarty J.* Photon echoes from two-dimensional excitons in GaAs-AlGaAs quantum wells // Appl. Phys. Lett. — 1985. — Nov. — Vol. 47, no. 9. — P. 995–997.

99. *Schultheis L.* [et al.]. Picosecond Phase Coherence and Orientational Relaxation of Excitons in GaAs // Phys. Rev. Lett. — 1986. — Oct. — Vol. 57, no. 14. — P. 1797–1800.

100. *Schultheis L.* [et al.]. Optical dephasing of homogeneously broadened two-dimensional exciton transitions in GaAs quantum wells // Phys. Rev. B. — 1986. — Dec. — Vol. 34, no. 12. — P. 9027–9030.

101. *Poltavtsev S. V.* [et al.]. Time-resolved photon echoes from donor-bound excitons in ZnO epitaxial layers // Phys. Rev. B. — 2017. — July. — Vol. 96, no. 3. — P. 035203.

102. *Honold a.* [et al.]. Collision broadening of two-dimensional excitons in a GaAs single quantum well // Phys. Rev. B. — 1989. — Sept. — Vol. 40, no. 9. — P. 6442–6445.

103. *Koch M.* [et al.]. Enhanced energy and phase relaxation of excitons in the presence of bare electrons // Phys. Rev. B. — 1995. — May. — Vol. 51, no. 19. — P. 13887–13890.

104. *Koch M.* [et al.]. Subpicosecond photon-echo spectroscopy on GaAs/AlAs short-period superlattices // Phys. Rev. B. — 1993. — Jan. — Vol. 47, no. 3. — P. 1532–1539.

105. *Brinkmann D.* [et al.]. Trion and exciton dephasing measurements in modulation-doped quantum wells: A probe for trion and carrier localization // Phys. Rev. B. — 1999. — Aug. — Vol. 60, no. 7. — P. 4474–4477.

106. *Feuerbacher B.* [et al.]. Quantum beats between the light and heavy hole excitons in a quantum well // Solid State Commun. — 1990. — June. — Vol. 74, no. 12. — P. 1279–1283.

107. *Leo K.* [et al.]. Subpicosecond four-wave mixing in GaAs/Al$_x$Ga$_{1-x}$As quantum wells // Phys. Rev. B. — 1991. — Sept. — Vol. 44, no. 11. — P. 5726–5737.

108. *Koch M.* [et al.]. Quantum beats versus polarization interference: An experimental distinction // Phys. Rev. Lett. — 1992. — Dec. — Vol. 69, no. 25. — P. 3631–3634.

109. *Chen X.* [et al.]. Temporally and spectrally resolved amplitude and phase of coherent four-wave-mixing emission from GaAs quantum wells // Phys. Rev. B. — 1997. — Oct. — Vol. 56, no. 15. — P. 9738–9743.

110. *Leo K.* [et al.]. Coherent oscillations of a wave packet in a semiconductor double-quantum-well structure // Phys. Rev. Lett. — 1991. — Jan. — Vol. 66, no. 2. — P. 201–204.

111. *Arimoto O.* [et al.]. Ultrafast quantum beats and optical dephasing of exciton systems in β-ZnP2 by spectrally resolved four-wave mixing // J. Phys. Soc. Japan. — 2003. — Vol. 72, no. 8. — P. 1863–1866.

112. *Mayer E. J.* [et al.]. Evidence of biexcitonic contributions to four-wave mixing in GaAs quantum wells // Phys. Rev. B. — 1994. — Vol. 50, no. 19. — P. 14730–14733.

113. *Mermillod Q.* [et al.]. Dynamics of excitons in individual InAs quantum dots revealed in four-wave mixing spectroscopy // Optica. — 2016. — Vol. 3, no. 4. — P. 377.

114. *Cundiff S. T.* [et al.]. Optical coherence in semiconductors: strong emission mediated by nondegenerate interactions // Phys. Rev. Lett. — 1996. — Aug. — Vol. 77, no. 6. — P. 1107–1110.

115. *Poltavtsev S. V.* [et al.]. Damping of Rabi oscillations in intensity-dependent photon echoes from exciton complexes in a CdTe/(Cd,Mg)Te single quantum well // Phys. Rev. B. — 2017. — Vol. 96, no. 7. — P. 1–7.

116. *Kosarev A. N.* [et al.]. Accurate photon echo timing by optical freezing of exciton dephasing and rephasing in quantum dots // Commun. Phys. — 2020. — Dec. — Vol. 3, no. 1. — P. 228.

117. *Gallart M.* [et al.]. Determining the nature of excitonic dephasing in high-quality GaN/AlGaN quantum wells through time-resolved and spectrally resolved four-wave mixing spectroscopy // Phys. Rev. B. — 2017. — July. — Vol. 96, no. 4. — P. 41303.

118. *Jakubczyk T.* [et al.]. Radiatively Limited Dephasing and Exciton Dynamics in $MoSe_2$ Monolayers Revealed with Four-Wave Mixing Microscopy // Nano Lett. — 2016. — Sept. — Vol. 16, no. 9. — P. 5333–5339.

119. *You J.* [et al.]. Nonlinear optical properties and applications of 2D materials: theoretical and experimental aspects // Nanophotonics. — 2018. — Dec. — Vol. 8, no. 1. — P. 63–97.

120. *Martin E. W.* [et al.]. Encapsulation Narrows and Preserves the Excitonic Homogeneous Linewidth of Exfoliated Monolayer $MoSe_2$ // Phys. Rev. Appl. — 2020. — Aug. — Vol. 14, no. 2. — P. 021002.

121. *Becker M. A.* [et al.]. Long Exciton Dephasing Time and Coherent Phonon Coupling in $CsPbBr_2Cl$ Perovskite Nanocrystals // Nano Lett. — 2018. — Vol. 18, no. 12. — P. 7546–7551.

122. *Trifonov A. V.* [et al.]. Photon Echo Polarimetry of Excitons and Biexcitons in a $CH_3 NH_3PbI_3$ Perovskite Single Crystal // ACS Photonics. — 2022. — Feb. — Vol. 9, no. 2. — P. 621–629.

123. *Nazarov R. S.* [et al.]. Photon echo from free excitons in a $CH_3NH_3PbI_3$ halide perovskite single crystal // Phys. Rev. B. — 2022. — June. — Vol. 105, no. 24. — P. 245202.

124. *Salewski M.* [et al.]. Photon echoes from (In,Ga)As quantum dots embedded in a Tamm-plasmon microcavity // Phys. Rev. B. — 2017. — Vol. 95, no. 3. — P. 35312.

125. *Poltavtsev S. V.* [et al.]. Photon echo transients from an inhomogeneous ensemble of semiconductor quantum dots // Phys. Rev. B. — 2016. — Vol. 93, no. 12. — P. 1–4.

126. *Wigger D.* [et al.]. Exploring coherence of individual excitons in InAs quantum dots embedded in natural photonic defects: Influence of the excitation intensity // Phys. Rev. B. — 2017. — Vol. 96, no. 16. — P. 1–12.

127. *Langer L.* [et al.]. Magnetic-Field Control of Photon Echo from the Electron-Trion System in a CdTe Quantum Well: Shuffling Coherence between Optically Accessible and Inaccessible States // Phys. Rev. Lett. — 2012. — Oct. — Vol. 109, no. 15. — P. 157403.

128. *Langer L.* [et al.]. Access to long-term optical memories using photon echoes retrieved from semiconductor spins // Nat. Photonics. — 2014. — Nov. — Vol. 8, no. 11. — P. 851–857.

129. *Poltavtsev S. V.* [et al.]. Quantum beats in the polarization of the spin-dependent photon echo from donor-bound excitons in CdTe/(Cd,Mg)Te quantum wells // Phys. Rev. B. — 2020. — Feb. — Vol. 101, no. 8. — P. 081409.

130. *Poltavtsev S. V.* [et al.]. In-plane anisotropy of the hole g factor in CdTe/(Cd,Mg)Te quantum wells studied by spin-dependent photon echoes // Phys. Rev. Res. — 2020. — Vol. 2, no. 2. — P. 1–14.

131. *Trifonov A. V.* [et al.]. Homogeneous optical anisotropy in an ensemble of InGaAs quantum dots induced by strong enhancement of the heavy-hole band Landé parameter q // Phys. Rev. B. — 2021. — Oct. — Vol. 104, no. 16. — P. L161405.

132. *Kosarev A. N.* [et al.]. Microscopic dynamics of electron hopping in a semiconductor quantum well probed by spin-dependent photon echoes // Phys. Rev. B. — 2019. — Sept. — Vol. 100, no. 12. — P. 121401.

133. *Smallwood C. L.*, *Cundiff S. T.* Multidimensional Coherent Spectroscopy of Semiconductors // Laser Photon. Rev. — 2018. — Dec. — Vol. 12, no. 12. — P. 1800171.

134. *Salewski M.* [et al.]. High-Resolution Two-Dimensional Optical Spectroscopy of Electron Spins // Phys. Rev. X. — 2017. — Aug. — Vol. 7, no. 3. — P. 031030.

135. *Poltavtsev S. V.* [et al.]. Polarimetry of photon echo on charged and neutral excitons in semiconductor quantum wells // Sci. Rep. — 2019. — Dec. — Vol. 9, no. 1. — P. 5666.

136. *Babenko I.* [et al.]. Studies of photon echo from exciton ensemble in (In,Ga)As quantum dots // J. Phys. Conf. Ser. — 2018. — Jan. — Vol. 951, no. 1. — P. 012029.

137. *Meier T., Thomas P., Koch S. W.* Coherent semiconductor optics. — Berlin, Heidelberg : Springer Berlin Heidelberg, 2007. — P. 1–319.

138. *Yanibekov I. I.* [et al.]. Difference in the behavior of the photon echo of excitons in InGaAs/GaAs quantum wells from the predictions of the model of two-level system ensemble // J. Phys. Conf. Ser. — 2020. — Mar. — Vol. 1482, no. 1. — P. 012020.

139. Spin Physics in Semiconductors. Vol. 157 / ed. by M. I. Dyakonov. — Berlin, Heidelberg : Springer Berlin Heidelberg, 2008. — (Springer Series in Solid-State Sciences).

140. *Klingshirn C.* ZnO: From basics towards applications // Phys. status solidi. — 2007. — Sept. — Vol. 244, no. 9. — P. 3027–3073.

141. *Rodina A. V.* [et al.]. Free excitons in wurtzite GaN // Phys. Rev. B - Condens. Matter Mater. Phys. — 2001. — Vol. 64, no. 11. — P. 1152041–11520419.

142. *Meyer B. K.* [et al.]. Bound exciton and donor–acceptor pair recombinations in ZnO // Phys. Stat. Sol. — 2004. — Vol. 241, no. 2. — P. 231–260.

143. *Kesteren H. W. van* [et al.]. Fine structure of excitons in type-II GaAs/AlAs quantum wells // Phys. Rev. B. — 1990. — Mar. — Vol. 41, no. 8. — P. 5283–5292.

144. *Solovev I. A.* [et al.]. Separation of inhomogeneous and homogeneous broadening manifestations in InGaAs/GaAs quantum wells by time-resolved four-wave mixing // J. Phys. Conf. Ser. — 2018. — Vol. 1124, no. 5.

145. *Kalusniak S.* [et al.]. Vertical cavity surface emitting laser action of an all monolithic ZnO-based microcavity // Appl. Phys. Lett. — 2011. — Jan. — Vol. 98, no. 1. — P. 011101.

146. *Tsukazaki A.* [et al.]. Repeated temperature modulation epitaxy for p-type doping and light-emitting diode based on ZnO // Nat. Mater. — 2004. — Dec. — Vol. 4, no. 1. — P. 42–46.

147. *Yip H.-L.* [et al.]. Polymer Solar Cells That Use Self-Assembled-Monolayer-Modified ZnO/Metals as Cathodes // Adv. Mater. — 2008. — June. — Vol. 20, no. 12. — P. 2376–2382.

148. *Djurišić A., Ng A., Chen X.* ZnO nanostructures for optoelectronics: Material properties and device applications // Prog. Quantum Electron. — 2010. — July. — Vol. 34, no. 4. — P. 191–259.

149. *Morhain C.* [et al.]. Internal electric field in wurtzite $ZnO/Zn_{0.78}Mg_{0.22}O$ // Phys. Rev. B. — 2005. — Dec. — Vol. 72, no. 24. — P. 241305.

150. *Bretagnon T.* [et al.]. Barrier composition dependence of the internal electric field in $ZnO/Zn_{1-x}MgxO$ quantum wells // Appl. Phys. Lett. — 2007. — May. — Vol. 90, no. 20. — P. 201912.

151. *Makino T.* [et al.]. Magneto-optical study of $ZnO/Mg_xZn_{1-x}O$ // Phys. Rev. B. — 2009. — Oct. — Vol. 80, no. 15. — P. 155333.

152. *Mallet E.* [et al.]. Accurate determination of homogeneous and inhomogeneous excitonic broadening in ZnO by linear and nonlinear spectroscopies // Phys. Rev. B. — 2013. — Apr. — Vol. 87, no. 16. — P. 161202.

153. *Davis J. A.* [et al.]. Observation of coherent biexcitons in ZnO/ZnMgO multiple quantum wells at room temperature // Appl. Phys. Lett. — 2006. — Oct. — Vol. 89, no. 18. — P. 182109.

154. *Solovev I. A.* [et al.]. Coherent dynamics of localized excitons and trions in ZnO/(Zn,Mg)O quantum wells studied by photon echoes // Phys. Rev. B. — 2018. — June. — Vol. 97, no. 24. — P. 245406.

155. *Liu H. Y.* [et al.]. Donor behavior of Sb in ZnO // J. Appl. Phys. — 2012. — Aug. — Vol. 112, no. 3. — P. 033706.

156. *Takagahara T.* Excitonic relaxation processes in quantum well structures // J. Lumin. — 1989. — Vol. 44, no. 4–6. — P. 347–366.

157. *Cundiff S. T., Wang H., Steel D. G.* Polarization-dependent picosecond excitonic nonlinearities and the complexities of disorder // Phys. Rev. B. — 1992. — Vol. 46, no. 11. — P. 7248–7251.

158. *Hellmann R.* [et al.]. Dephasing of localized and delocalized excitons in disordered CdTe/(Cd,Mg)Te multiple quantum wells // Mater. Sci. Forum. — 1995. — Vol. 182–184. — P. 199–202.

159. *Moody G.* [et al.]. Intrinsic homogeneous linewidth and broadening mechanisms of excitons in monolayer transition metal dichalcogenides // Nat. Commun. — 2015. — Vol. 6, May. — P. 1–6.

160. *Esser A.*, *Yayon Y.*, *Bar-Joseph I.* Localization Properties of Trions // Phys. status solidi. — 2002. — Nov. — Vol. 234, no. 1. — P. 266–272.

161. *Zimmermann R.*, *Große F.*, *Runge E.* Excitons in semiconductor nanostructures with disorder // Pure Appl. Chem. — 1997. — Jan. — Vol. 69, no. 6. — P. 1179–1186.

162. *Noll G.* [et al.]. Picosecond stimulated photon echo due to intrinsic excitations in semiconductor mixed crystals // Phys. Rev. Lett. — 1990. — Feb. — Vol. 64, no. 7. — P. 792–795.

163. *Poltavtsev S. V.* [et al.]. Long coherent dynamics of localized excitons in (In,Ga)N/GaN quantum wells // Phys. Rev. B. — 2018. — Vol. 98, no. 19. — P. 195315.

164. *Narukawa Y.* [et al.]. Role of self-formed InGaN quantum dots for exciton localization in the purple laser diode emitting at 420 nm // Appl. Phys. Lett. — 1997. — Vol. 70, no. 8. — P. 981.

165. *Chichibu S.* [et al.]. Spontaneous emission of localized excitons in InGaN single and multiquantum well structures // Appl. Phys. Lett. — 1996. — Vol. 69, no. 27. — P. 4188.

166. *Chichibu S.*, *Wada K.*, *Nakamura S.* Spatially resolved cathodoluminescence spectra of InGaN quantum wells // Appl. Phys. Lett. — 1997. — Vol. 71, no. 16. — P. 2346.

167. *Singh R.* [et al.]. Phase separation in InGaN thick films and formation of InGaN/GaN double heterostructures in the entire alloy composition // Appl. Phys. Lett. — 1997. — Vol. 70, no. 9. — P. 1089.

168. *Musikhin Y. G.* [et al.]. Influence of metalorganic chemical vapor deposition growth conditions on In-rich nanoislands formation in InGaN/GaN structures // Appl. Phys. Lett. — 2002. — Vol. 80, no. 12. — P. 2099.

169. *Bolshakov A. S.* [et al.]. Resonant Bragg structures based on III-nitrides // J. Mater. Res. — 2015. — Vol. 30, no. 5. — P. 603.

170. *Tsatsulnikov A. F.* [et al.]. Influence of hydrogen on local phase separation in InGaN thin layers and properties of light-emitting structures based on them // Semiconductors. — 2011. — Feb. — Vol. 45, no. 2. — P. 271–276.

171. *Oliver R. A.* [et al.]. InGaN quantum dots grown by metalorganic vapor phase epitaxy employing a post-growth nitrogen anneal // Appl. Phys. Lett. — 2003. — July. — Vol. 83, no. 4. — P. 755–757.

172. *Choi S.-K.* [et al.]. Fabrication and characterization of self-assembled InGaN quantum dots by periodic interrupted growth // / ed. by M. Razeghi, G. J. Brown. — 02/2007. — 64791F.

173. *Zimmermann R.* [et al.]. Transient four-wave-mixing spectroscopy on gallium nitride: Energy splittings of intrinsic excitonic resonances // Phys. Rev. B. — 1997. — Vol. 56, no. 20. — R12722–R12724.

174. *Ishiguro T.* [et al.]. Coherent manipulation of A and B excitons in GaN // Phys. Status Solidi C. — 2007. — Vol. 4, no. 7. — P. 2776–2779.

175. *Schneck J. R.* [et al.]. Temperature dependent photon echoes of a GaN thin film // Appl. Phys. Lett. — 2012. — Vol. 101, no. 14. — P. 142102.

176. *Haag H.* [et al.]. Optical nonlinearities of gallium nitride // J. Mater. Sci. Eng. B. — 1997. — Vol. 50, no. 1–3. — P. 197–200.

177. *Kundys D. O.* [et al.]. Resolution of discrete excited states in $In_xGa_{1-x}N$ multiple quantum wells using degenerate four-wave mixing // Phys. Rev. B. — 2006. — Apr. — Vol. 73, no. 16. — P. 165309.

178. *Bolshakov A. S.* [et al.]. Room temperature exciton-polariton resonant reflection and suppressed absorption in periodic systems of InGaN quantum wells // J. Appl. Phys. — 2017. — Vol. 121, no. 13. — P. 133101.

179. *Azuhata T.* [et al.]. Optical phonons in GaN // Phys. B Condens. Matter. — 1996. — Vol. 219/220. — P. 493.

180. *Borri P.* [et al.]. Exciton dephasing via phonon interactions in InAs quantum dots: Dependence on quantum confinement // Phys. Rev. B. — 2005. — Vol. 71, no. 11. — P. 115328.

181. *Kim M.* [et al.]. Investigating carrier localization and transfer in InGaN/GaN quantum wells with V-pits using near-field scanning optical microscopy and correlation analysis // Sci. Rep. — 2017. — Vol. 7. — P. 42221.

182. *Hahn W.* [et al.]. Evidence of nanoscale Anderson localization induced by intrinsic compositional disorder in InGaN/GaN quantum wells by scanning tunneling luminescence spectroscopy // Phys. Rev. B. — 2018. — July. — Vol. 98, no. 4. — P. 45305.

183. *Chichibu S. F.* [et al.]. Optical properties of InGaN quantum wells // Mater. Sci. Eng., B. — 1999. — Vol. 59, no. 1–3. — P. 298–306.

184. *Ivchenko E. L.*, *Nesvizhskii A. I.*, *Jorda S.* Resonant Bragg reflection from quantum-well structures // Superlattices Microstruct. — 1994. — Vol. 16, no. 1. — P. 17–20.

185. *Hübner M.* [et al.]. Collective Effects of Excitons in Multiple-Quantum-Well Bragg and Anti-Bragg Structures // Phys. Rev. Lett. — 1996. — May. — Vol. 76, no. 22. — P. 4199–4202.

186. *Bayer M.*, *Forchel A.* Temperature dependence of the exciton homogeneous linewidth in $In_{0.60}Ga_{0.40}As$/GaAs self-assembled quantum dots // Phys. Rev. B. — 2002. — Vol. 65, no. 4. — P. 41308.

187. *Schömig H.* [et al.]. Probing Individual Localization Centers in an InGaN/GaN Quantum Well // Phys. Rev. Lett. — 2004. — Vol. 92, no. 10. — P. 106802.

188. *Gotoh H.* [et al.]. Effects of nonradiative centers on localized excitons in InGaN quantum well structures // Appl. Phys. Lett. — 2006. — Vol. 89, no. 22. — P. 222110.

189. *Poltavtsev S.* [et al.]. Extremely low inhomogeneous broadening of exciton lines in shallow (In,Ga)As/GaAs quantum wells // Solid State Commun. — 2014. — Vol. 199. — P. 47–51.

190. *Solovev I. A.* [et al.]. Long-lived dark coherence brought to light by magnetic-field controlled photon echo // Phys. Rev. B. — 2021. — June. — Vol. 103, no. 23. — P. 235312.

191. *Solovev I. A.* [et al.]. Manipulation of optical coherence of quantum-well excitons by transverse magnetic field // Phys. Rev. B. — 2022. — Sept. — Vol. 106, no. 11. — P. 115401.

192. *Lu Z.* [et al.]. Magnetic field mixing and splitting of bright and dark excitons in monolayer MoSe$_2$ // 2D Mater. — 2020. — Vol. 7, no. 1.

193. *Zhang X. X.* [et al.]. Magnetic brightening and control of dark excitons in monolayer WSe$_2$ // Nat. Nanotechnol. — 2017. — Vol. 12, no. 9. — P. 883–888.

194. *Zhou Y.* [et al.]. Probing dark excitons in atomically thin semiconductors via near-field coupling to surface plasmon polaritons // Nat. Nanotechnol. — 2017. — Vol. 12, no. 9. — P. 856–860.

195. *Glasberg S.* [et al.]. Exciton exchange splitting in wide GaAs quantum wells // Phys. Rev. B. — 1999. — Dec. — Vol. 60, no. 24. — R16295–R16298.

196. *Bayer M.* [et al.]. Spectroscopic study of dark excitons in In$_x$Ga$_{1-x}$As self-assembled quantum dots by a magnetic-field-induced symmetry breaking // Phys. Rev. B. — 2000. — Mar. — Vol. 61, no. 11. — P. 7273–7276.

197. *Zaric S.* Optical Signatures of the Aharonov-Bohm Phase in Single-Walled Carbon Nanotubes // Science (80-.). — 2004. — May. — Vol. 304, no. 5674. — P. 1129–1131.

198. *Poem E.* [et al.]. Accessing the dark exciton with light // Nat. Phys. — 2010. — Dec. — Vol. 6, no. 12. — P. 993–997.

199. *Schwartz I.* [et al.]. Deterministic Writing and Control of the Dark Exciton Spin Using Single Short Optical Pulses // Phys. Rev. X. — 2015. — Jan. — Vol. 5, no. 1. — P. 011009.

200. *Ikeuchi O.* [et al.]. Observation of population transfer to dark exciton states by using spin-diffracted four-wave mixing // J. Appl. Phys. — 2003. — June. — Vol. 93, no. 12. — P. 9634–9638.

201. *Accanto N.* [et al.]. Engineering the spin-flip limited exciton dephasing in colloidal CdSe/CdS quantum dots // ACS Nano. — 2012. — Vol. 6, no. 6. — P. 5227–5233.

202. *Siegner U.* [et al.]. Quantum interference in the system of Lorentzian and Fano magnetoexciton resonances in GaAs // Phys. Rev. B. — 1995. — Feb. — Vol. 51, no. 8. — P. 4953–4961.

203. *Cundiff S. T.* [et al.]. Excitonic dephasing in semimagnetic semiconductors // J. Opt. Soc. Am. B. — 1996. — Vol. 13, no. 6. — P. 1263.

204. *Ivchenko E.* [et al.]. Exciton longitudinal-transverse splitting in GaAs/AlGaAs superlattices and multiple quantum wells // Solid State Commun. — 1989. — May. — Vol. 70, no. 5. — P. 529–534.

205. *Miller R. C.* [et al.]. Biexcitons in GaAs quantum wells // Phys. Rev. B. — 1982. — Vol. 25, no. 10. — P. 6545–6547.

206. *Sobiesierski Z.* [et al.]. Photoluminescence and photoluminescence excitation spectroscopy of H-related defects in strained $In_xGa_{1-x}As$/GaAs (100) quantum wells // J. Vac. Sci. Technol. B Microelectron. Nanom. Struct. — 1992. — Vol. 10, no. 4. — P. 1975.

207. *Borri P.* [et al.]. Binding energy and dephasing of biexcitons in $In_{0.18}Ga_{0.82}As$/GaAs single quantum wells // Phys. Rev. B - Condens. Matter Mater. Phys. — 1999. — Vol. 60, no. 7. — P. 4505–4508.

208. *Feldmann J.* [et al.]. Coherent dynamics of excitonic wave packets // Phys. Rev. Lett. — 1993. — Vol. 70, no. 20. — P. 3027–3030.

209. *Ikezawa M.* [et al.]. Photon echo study of excitons and excitonic complexes in self-assembled quantum dots // J. Lumin. — 2007. — Vol. 122/123, no. 1/2. — P. 730–734.

210. *Glazov M. M.* Electron & Nuclear Spin Dynamics in Semiconductor Nanostructures. Vol. 1. — Oxford : Oxford University Press, 2018.

211. *Bir G. L.*, *Pikus G. E.* Symmetry and strain-induced effects in semiconductors. — New York : Wiley, 1974.

212. *Kesteren H. W. van* [et al.]. Optically Detected Magnetic Resonance Study of a Type-II GaAs-AlAs Multiple Quantum Well // Phys. Rev. Lett. — 1988. — July. — Vol. 61, no. 1. — P. 129–132.

213. *Madelung O.*, *Osten W. von der*, *Rössler U.* Intrinsic Properties of Group IV Elements and III-V, II-VI and I-VII Compounds / ed. by O. Madelung. — Berlin, Heidelberg : Springer-Verlag Berlin Heidelberg, 1987.

214. *Heberle A. P.*, *Rühle W. W.*, *Ploog K.* Quantum beats of electron Larmor precession in GaAs wells // Phys. Rev. Lett. — 1994. — June. — Vol. 72, no. 24. — P. 3887–3890.

215. *Malinowski A.* [et al.]. Larmor beats and conduction electron g factors in $In_xGa_{1-x}As$/GaAs quantum wells // Phys. Rev. B. — 1999. — Sept. — Vol. 60, no. 11. — P. 7728–7731.

216. *Malinowski A., Harley R.* Anisotropy of the electron g factor in lattice-matched and strained-layer III-V quantum wells // Phys. Rev. B - Condens. Matter Mater. Phys. — 2000. — Vol. 62, no. 3. — P. 2051–2056.

217. *Kusrayev Y. G.* [et al.]. Homogeneous optical anisotropy in an ensemble of InGaAs quantum dots induced by strong enhancement of the heavy-hole band Landé parameter q // Phys. Rev. Lett. — 1999. — Apr. — Vol. 82, no. 15. — P. 3176–3179.

218. *Semenov Y. G., Ryabchenko S. M.* Effects of photoluminescence polarization in semiconductor quantum wells subjected to an in-plane magnetic field // Phys. Rev. B. — 2003. — July. — Vol. 68, no. 4. — P. 045322.

219. *Marie X.* [et al.]. Hole spin quantum beats in quantum-well structures // Phys. Rev. B. — 1999. — Aug. — Vol. 60, no. 8. — P. 5811–5817.

220. *Tholen H. M.* [et al.]. Active tuning of the g-tensor in InGaAs/GaAs quantum dots via strain // Phys. Rev. B. — 2019. — Vol. 99, no. 19. — P. 1–8.

221. *Wu S.* [et al.]. Electron and Hole g Tensors of Neutral and Charged Excitons in Single Quantum Dots by High-Resolution Photocurrent Spectroscopy // Phys. Rev. Appl. — 2020. — July. — Vol. 14, no. 1. — P. 014049.

222. *Zhukov E. A.* [et al.]. Magnetic field dependence of the in-plane hole g factor in ZnSe- and CdTe-based quantum wells // Phys. Rev. B. — 2021. — Mar. — Vol. 103, no. 12. — P. 125305.

223. *Yugova I. A.* [et al.]. Exciton fine structure in InGaAs/GaAs quantum dots revisited by pump-probe Faraday rotation // Phys. Rev. B. — 2007. — May. — Vol. 75, no. 19. — P. 195325.

224. *Blum K.* Density matrix theory and applications / ed. by Zubarev, D. N. — Moscow : Mir, 1983.

225. *Landau L. D., Lifshitz E. M.* Quantum Mechanics. — 3rd. — Pergamon, 1977.